TÉCNICO LISBOA

Numerical flue gas flow analysis in wet limestone Flue Gas Desulfurization installation using Computational Fluid Dynamics

Kamil Bogdan Chłosta

Thesis to obtain the Master of Science Degree in

Energy Engineering and Management

Supervisors: Prof. Luís Rego da Cunha de Eça
Dr. Karol Sztekler

Examination Committee

Chairperson: Prof. Edgar Caetano Fernandes
Supervisor: Prof. Luís Rego da Cunha de Eça
Member of the Committee: Dr. Duarte Manuel Salvador Freire Silva de Albuquerque

November 2018

Abstract

This Thesis focuses on the simulation of flue gas flow in wet limestone FGD installation in a combined heat and power plant using Computational Fluid Dynamics. Geometry description, mesh generation, flow solution and post-processing were performed using the following tools: ANSYS Fluent, ANSYS Meshing, ANSYS SpaceClaim and Engineering Equation Software.

The numerical simulations provide static pressure and velocity distributions throughout the installation, illustrating the locations subject to increased pressure levels. The analysis pointed out the locations of the ducts configuration design that may be improved. The simulations also enable to adjust the secondary Induced Draft fans setup to produce sufficiently low pressure for the flue gas ducts and the collector in order to keep the complete installation under negative pressure. The various steam boiler capacities configurations are simulated to provide important information to the installation owner.

Keywords: *Wet limestone FGD, CFD, desulphurization*

Resumo

Esta Tese apresenta a simulação do escoamento de gases de combustão do processo de dessulfuração de centrais termoelétricas a carvão utilizando técnicas Mecânica dos Fluidos Computacional (habitualmente designadas por CFD). A modelação da geometria, geração de malhas, solução numérica do escoamento e o pós-processamento utilizaram as seguintes ferramentas de cálculo: ANSYS Fluent, ANSYS Meshing, ANSYS SpaceClaim e Engineering Equation Software.

As simulações numéricas determinaram a pressão estática e a distribuição de velocidade ao longo das condutas da instalação, identificando as regiões em que a pressão atinge valores superiores ao desejado. A análise dos resultados identificou as condutas cujo desenho pode ser melhorado. As simulações também permitiram ajustar o funcionamento dos ventiladores secundários de forma a garantir que a pressão é inferior à atmosférica no interior de todas as condutas da instalação. Várias capacidades das caldeiras de vapor foram simuladas para obter curvas de funcionamento essenciais para a operação da instalação.

Keywords: *FGD de calcário húmido, CFD, dessulfurização*

Table of content

List of tables

List of figures

1. Introduction

With the exponential growth of the computing power of our computers throughout recent decades, the numerical analysis has become yet another established way to obtain a solution to variety of researched problems. Analytical solving can allow to get exact solution to study the behavior of the system with changing properties. However, since the analytical methods are of limited use we can solve very few practical engineering problems. To elaborate more deeply, when fluid motion is governed by Navier-Stokes equations - a set of coupled nonlinear partial differential equations derived from fundamental laws of conservation of mass, momentum and energy - the fluid flow velocity, pressure, density and temperature are often unknown. As a result it is often not possible to obtain an analytical solution. In these situations – leaving the numerical analysis aside - the scientists usually try to find an experimental solution in the laboratories. However, it often is impossible and difficult to get satisfactory and free from error solution. The answers could not reflect the real problem due to difficulties in enforcing dynamic and geometric similitude between laboratory experiments and designed prototypes. To add-up, not only is it troublesome but also expensive often due to complex design and construction. Numerical analysis is an attractive alternative, when there is no possibility to solve the problem analytically or an empirical solution is not economically and physically feasible. Not only can it be useful when designing a new system, but also finds it usage in investigating the working performance of an existing installations without necessity to shut them down and to install additional (otherwise redundant) measurement devices. The latter is the topic of this master thesis, as it aims to obtain a numerical solution to a Navier-Stokes equations based on conservation of mass and momentum in the existing and operating wet limestone Flue Gas Desulphurization installation.

The objective is to solve the problem numerically and obtain fluid static pressure and velocity distributions throughout the ducts system which directs the flue gases to the absorber, where the wet limestone FGD process takes place, it is necessary to maintain a sub-pressure in the ducts, however the induced draft fans warranty measurements indicated elevated (positive) pressure levels. Hence, it was necessary to find pressure distribution and velocity of the flue gases flowing through the ducts to evaluate the existing designed ducts configuration and nominal operating parameters of the secondary Induced Draft fans, that are responsible for maintaining appropriate pressure level in examined part of the wet limestone FGD installation.

The cogeneration plant, in which wet Flue Gas Desulphurization installation has been investigated, has the capacity of generating around 260 MW_e (electrical) and 810 MW_t (thermal) power. The CHP power plant has tree steam and two water boilers. The latter two work only few days a year, hence their influence on overall flue gas ducts system is negligible in regard to a whole year. Hence the flue gas ducts of the water boilers has been omitted in the numerical model consideration. The collector is the place where the flue gas streams of each of the steam boilers (namely K1, K2, K3) flow through. Flue gas leaves each of the steam boilers through two separate ducts per each unit. The ducts then connect and the stream flows further to

the collector. Subsequently, the collector directs the streams from all three units to the absorber. The whole process and the installation is depicted in detail on Figure 2.1 and 2.2. It is worth to mention that in this case there two different types of Induced Draft fans distinguished. The primary Induced draft fans are responsible to force the flue gas stream from the boilers to the ducts and collector configuration. However, secondary Induced Draft fans suck the flue gas from the collector and force the stream to flow to the absorber. The usage of Induced Draft fans results in creating negative pressure upstream and positive pressure downstream the fans. Hence, the location of the most elevated pressure was expected to occur at the inlets of the primary Induced Draft fans. The type of analyzed FGD system in the cogeneration power plant is wet scrubbing with limestone as a sorbent. The wet limestone Flue Gas Desulphurization system is described more widely in the “Wet FGD systems” chapter in this paper.

The geometry of the given problem was not available in CAD. Hence it was necessary to create the model from detailed design documentation, including technical drawings. It was severely important to create the model very close to the real design to cover influence of all geometry details on the flue gas flow. After development of the model geometry in SpaceClaim, the numerical mesh has been created in ASNYS Meshing software to allow further progress in the numerical modeling. The mesh optimization process has been conducted, including mesh sensitivity analysis. The emphasis was on mesh size, orthogonal quality and skewness. It has allowed to create model that would provide results with satisfactory accuracy with simultaneous minimization of the computing time. Subsequently, in order to input appropriate boundary conditions, turbulence model and set up proper flue gas parameters, as well as to choose other computing functions in ANSYS Fluent, the data from Induced Draft fans warranty measurements and other existing company-internal records of operational conditions has been analyzed. The simulations has been carried out for 36 different operation conditions (steam boiler capacities), with additional 12 with repeated working conditions, but assumed averaged mass flow rates (sum of the mass flow rates of the streams leaving given unit divided by the amount of fluid inlets of respective units) to examine the influence of the regular flow in each of the channels of particular K1, K2 and K3 units. The results of the numerical analysis has allowed to indicate faulty ducts configuration design of the K2 unit (in place, where two respective flue gas ducts joints). It has allowed to recognize the places with elevated static pressure levels. Moreover, the regulation curves has been developed to help set up proper nominal work parameters of the secondary Induced Draft fans. Furthermore, the possibility to program secondary ID fans to work in compliance with steam boiler capacities has been observed.

Sulphur compounds produced during combustion processes have severely negative impact on environment. Hence emission limitations have essential importance in improvement of the atmosphere condition. The content of Sulphur in used fuels also creates technical problems concerning maintenance and utilization of combustion systems. Sulphur oxides released in combustion processes impact also boiler heating surfaces. Considering Sulphur oxides, flames contain mainly Sulphur dioxides and - to a lesser extend - Sulphur trioxides. The sulfur content in fuels depends mainly on the type of fuel and the conditions

of its origins, including geological age and deposit forming conditions for fossil fuels. Sulphur mass-based content in solid and liquid fuels stays usually within following limits: peat (0.8-1%), bituminous coal (0.32-10%), lignite (1-4%), coke (0.8 -1.3%), petroleum (0.1-3%), heating oil (0.5-5%) and diesel oil (0.2-1.2%). Taking under consideration gaseous fuels, sulfur is present mostly as hydrogen sulfide. Volume-based content of H2S in cleaned natural gas in pipelines network does not extend 400ppm. Hydrogen sulfide concentration in coke oven gas is within 0.02-0.5 g/ mn3

Flue gas desulphurization (FGD) is a group of technologies applied for the purpose of sulfur dioxide SO_2 removal and its mostly used in flue gas exhaust systems of fossil fuel power plants. Not only is it found to be applied in conventional power plants but also to abate SO_2 emissions of other emitting processes, e.g. waste incineration plants. To most commonly used FGD systems belong: wet scrubbing (applying a slurry of alkaline sorbent – generally limestone or lime), spray-dry scrubbing, wet sulfuric acid process (with simultaneous production of commercially viable sulfuric acid), dry or semi-dry sorbent injection technologies (for instance powdered hydrated lime introduced into exhaust ducts).The Flue Gas Desulphurization system has been traditionally considered as wet scrubbers that abate SO_2 emissions from large electric utility boilers. The FGD technology in coal-based energy industry emerged in power plants and some other industrial processes in early 1970s in US and Japan. Ever since, it has been growing rapidly in the 1980s in Europe [1, 2]. In the FGD process, the flue gas stream reacts with an absorbent in an absorber or a scrubber vessel. As a result, the high solid S slurry is produced. As stated by to US EPA (US Environmental Protection Agency) FGD technologies could be classified as non-regenerable or regenerable processes based on whether the Sulphur-based compounds are separated from the absorbent as a by-product or discharged as a waste product [3, 4]. Another classification proposed by Clarke and Sloss [5] divides FGD systems into the regenerable and non-regenerable, but the latter is furthermore put into wet scrubber and spray dry systems subcategories. Still, other authors [2, 6] classifies FGD systems into four categories: wet scrubbers, spray dry scrubbers, sorbent injection and regenerable processes. Subsequently, each given category is subdivided into a few subcategories based on the respective chemical reactions and flow conditions. Without emphasis on classifications, most of the specialized literature [2-7, 8] acknowledge the wet limestone Flue Gas Desulphurization systems as most commonly used (87%) often due to its high Sulphur removal efficiency (ranging between 90-95%) and lower operating costs [9].

2. Flue Gas Desulfurization Technologies for Coal-Fired Power Plants

The term Flue Gas Desulphurization system has been traditionally thought of as wet scrubbers that are responsible for limiting SO_2 emissions from sizable electric utility boilers. The Flue Gas Desulphurization installations occurrence in coal-based energy industry in power plants and some other industrial processes dates on early 1970s in US and Japan. Since then, it has been expanding rapidly in the 1980s in Europe [1, 2]. In the Flue Gas Desulphurization process, the flue gas reacts with an absorbent in an absorber or a scrubber vessel. As a result of this interaction, the high solid S slurry is produced. According to US EPA

(US Environmental Protection Agency) FGD installations are classified as non-regenerable or regenerable processes depending on whether the Sulphur-based compounds are separated from the absorbent as a by-product or disposed of as a waste product [A2]. Another classification given by Clarke and Sloss [5] divides FGD systems into the regenerable and non-regenerable, but the latter is put into wet scrubber and spray dry systems subcategories. Yet, other authors [2, 6] suggest different approach classifying FGD systems into 4 categories: wet scrubbers, spray dry scrubbers, sorbent injection and regenerable processes. Moreover, each category is subdivided into a few subcategories based on the particular chemical reactions and flow conditions.

Without regard to classifications, the majority of specialized literature [2-7, 8] acknowledge the wet limestone Flue Gas Desulphurization systems as the most widely used (87%) mostly due to its high Sulphur removal efficiency (ranging between 90-95%) and relatively low operating costs [9]. In addition, since the thesis concerns a CHP plant that uses wet limestone Flue Gas Desulphurization, this chapter will focus mainly on those systems description and the current state of knowledge in the field. Thus, the attention will be turned to general review of the FGD systems, that mitigate Sulphur emissions in coal-fired power plants, its physic-chemical processes connected with the design, operation and maintenance of wet limestone FGDs, referring to removal efficiency for major, minor and trace elements by wet limestone FGD as well as the fate of some pollutants during the process and the characteristics of desulphurization process by-products.

2.1 Wet FGD systems

The wet scrubbers produce regenerable or non-regenerable products. Taking under consideration regenerable processes, the sorbent undergoes a regeneration, that rises SO_2, H_2SO_4 or S^0, producing a sludge by-product, which can be afterwards sold to offset the operating costs of the FGD to some degree. In case of non-regenerable processes the Sulphur is bound with the sorbent producing a waste that has to be disposed of properly or used in very particular applications. In general, coal-fired power plants with wet FGD systems use limestone, slaked lime or a mixture of slaked lime and alkaline Fly Ash sorbents, that react with SO_2 forming Ca-S compounds [9].

2.1.1 Wet limestone FGD systems

The non-regenerable wet limestone Flue Gas Desulphurization refer to complex acid-base reactions occurring under natural or forced oxidation conditions. Following the reactions of desulphurization two main regions can be distinguished in majority of the scrubbers, that are gas-to-liquid contact zone and the reaction tank. In case of forced oxidation following reactions [1, 10] take place in the gas-to-liquid contact zone with a pH ranging between 5 and 6:

$$SO_{2(g)} \leftrightarrow SO_{2(aq)}$$ Gas SO_2 dissolution (2.1)

$$SO_{2(g)} + H_2O \leftrightarrow H_2SO_{3(aq)}$$ Hydrolysis of SO_3 (2.2)

$H_2SO_{3(aq)} \leftrightarrow H^+_{(aq)} + HSO^-_3 \leftrightarrow H^+_{(aq)} + SO^{2-}_3$ Sulfurous acid dissociation (2.3)

$CaCO_{3(s)} + H^+_{(aq)} \leftrightarrow Ca^{2+}_{(aq)} + HCO^-_{3(aq)}$ Limestone dissolution (2.4)

$HCO^-_{3(aq)} + H^+_{aq} \leftrightarrow CO_{2(aq)} + H_2O_{(aq)}$ Acid-base neutralization (2.5)

$CO_{2(aq)} \leftrightarrow CO_{2(g)}$ Equilibrium desorption (2.6)

Thus, by combining equations above the overall reaction in the gas-to-liquid zone can be obtained:

$$CaCO_{3(s)} + SO_{2(g)} + 2H_2O_{(aq)} \rightarrow CaSO_3 \cdot 2H_2O_{(aq)} + CO_{2(aq)} \quad (2.7)$$

Reactions that has started in the gas-to-liquid contact zone are then completed in the reaction tank, that delivers a sufficient reaction time for the complete oxidation of SO^{2-}_3 to SO^{2-}_4 as stated below:

$$CaSO_3 \cdot 2H_2O_{(aq)} + 1/2O_{2(g)} \rightarrow CaSO_4 \cdot 2H_2O_{(s)} \quad (2.8)$$

When the pH ranges between 4.5 and 5.5, the reaction varies [10]. Following SO_2 absorption, the neutralization by limestone produces $\mathrm{Ca(HSO_3)_2}$, as presented below:

$$CaCO_{3(s)} + SO_{2(g)} + H_2O \leftrightarrow Ca(HSO_3)_{2(aq)} + CO_{2(aq)} + H_2O \quad (2.9)$$

$$Ca(HSO_3)_{2(aq)} + O_{2(g)} + 2H_2O \rightarrow CaSO_4 \cdot 2H_2O_{(s)} + H_2SO_{4(aq)} \quad (2.10)$$

In addition, in the reaction tank partially spent slurry is mixed with fresh limestone slurry to replenish used $CaCO_3$. The acidic slurry is being neutralized in the reaction tank. Furthermore, produced CO_2 is afterwards desorbed [10]:

$$CaCO_{3(s)} + H_2SO_{4(aq)} + H_2O \rightarrow CaSO_4 \cdot 2H_2O_{(s)} + CO_{2(g)} \quad (2.11)$$

Some wet limestone FGD systems may operate in natural oxidation mode provided appropriate pH level of limestone slurry, SO_2 concentrations and proper amount of excess air in the flue gas. In the majority of applications it is better to control oxidation thought [10]. In case of natural oxidation, the primary product is a mixture 50-60% of $CaSO_3 \cdot 1/2H_2O$ and $CaSO_4 \cdot 2H_2O$ in troublesome sludge form, that is difficult to dewater in contrast to forced oxidation, that allows to obtain the main product as around 90% $CaSO_4 \cdot 2H_2O$ [10].In forced oxidation mode (Figure 2.1), limestone slurry is processed in a locked ball mill (1) and then pumped into the scrubber in controlled amounts to maintain the pH of the scrubber on the proper level [1]. In the gas to liquid contact zone, sprayed limestone contained in suspended slurry droplets (2) undergo reaction, based on pH level, with HSO^-_3 or SO^{2-}_3, that are the products of aqueous dissolution and hydrolysis of SO_2 (3). In the process, after reacting with the flue gas, the slurry droplets drop down into reaction tank. The oxygen that inlets the reaction tank form the bottom sprinklers undergoes the reaction with a $Ca(HSO_3)_2$ or $CaSO_3 \cdot 2H_2O$, depending on whichever holds an entirely oxidized $CaSO_4 \cdot 2H_2O$ product (4). The slurry

agitators are placed around the reaction tank to help with mixing the solid particles with the gypsum slurry. The produced gypsum slurry can consist of about 15 wt.% (percentage by weight, mass fraction) of suspended solids. Thus, during filtration process hydro-cyclones forward the gypsum slurry into a vacuum filter, where fresh water and concentrate wash the solids forming the FGD gypsum by-product (6), that generally contains about 10 wt.% of moisture. Afterwards, the FGD gypsum end-product is transported and disposed of in the landfills [11], is used in the cement industry or finds other various applications. In case of limited water resources, the water is filtered and re-circulated into the scrubber (7). Power plants with access to water are generally equipped with effluent treatment plants that cause high pollutant load of the sludge. After water drops are removed by water eliminator from the gas stream outgoing the FGD system (OUT-FGD), the PM and gaseous stream from FGD installation are emitted through the stack. The efficiency of abating SO_2 emissions using wet limestone Flue Gas Desulphurization system ranges between 92% and 98% [10].

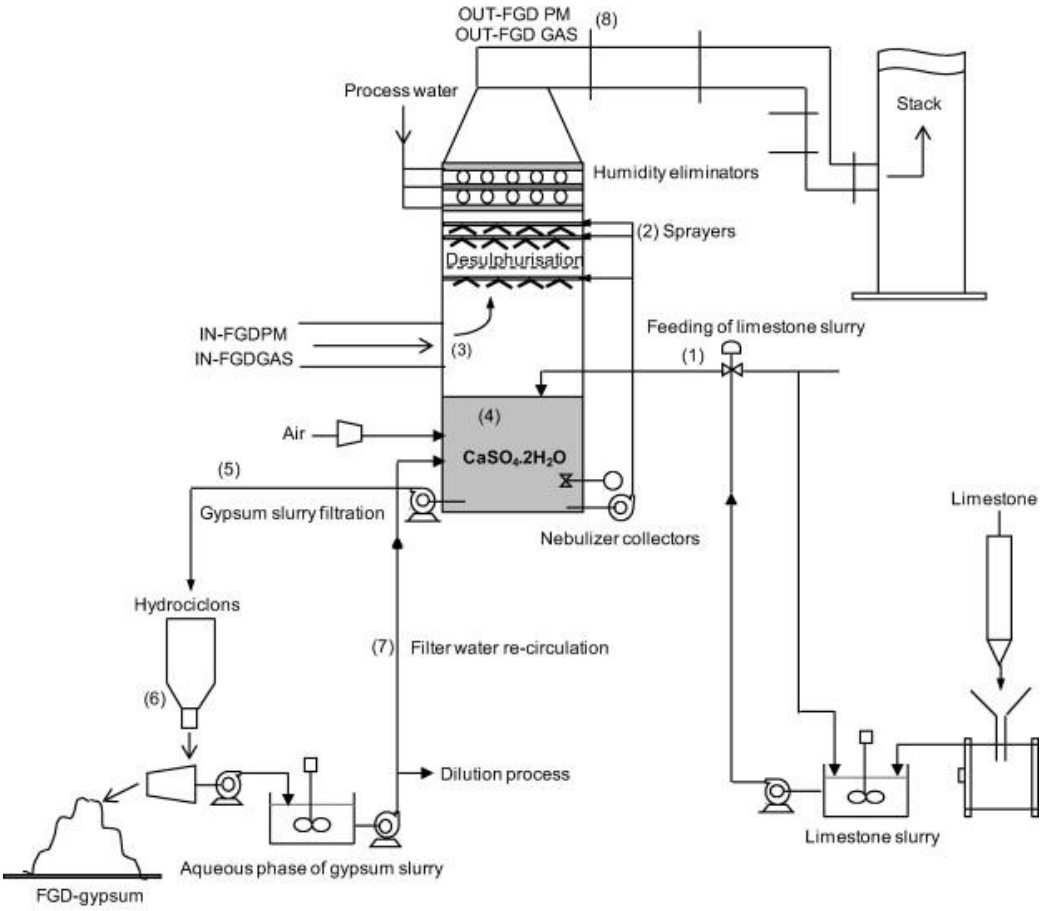

(1) Feeding of limestone slurry to the scrubber

(2) Limestone slurry is pumped through the nebulizer collectors and sprayed into the scrubber to react with SO_2.

(3) Gas and PM input flow into the scrubber after combustion process.

(4) Formation of gypsum slurry as result of the desulphurisation process.

(5) Extraction of gypsum slurry for the filtration process by hydro-cyclones

(6) Production of gypsum slurry and FGD-gypsum.

(7) Re-circulation of filtered water after dilution process.

(8) Cleaned gas and PM flow OUT-FGD

Figure 2.1 Conventional design and operation idea of a wet limestone FGD system (forced oxidation). [1]

2.1.2 Wet lime and magnesium-lime Flue Gas Desulphurization systems

To abate SO_2 content in flue gases, lime scrubbing uses CaO (normally 90%). Although lime is more expensive, its far more reactive than limestone slurry [12]. One of the types of the lime processes is the Magnesium Enhanced Lime (MEL) [12]. It uses a particular type of lime: dolomitic lime (around 20% of MgO) or magnesium-enhanced lime (in range between 5-8% of MgO). Due to better solubility of magnesium salts than calcium sorbents the absorber slurry is much more alkaline. Thus, the Magnesium Enhanced Lime process is able to have high efficiencies of SO_2 removal in far smaller scrubber comparing to limestone

scrubbers. However, the end-products of Flue Gas Desulfurization systems based on the Magnesium Enhanced Lime process have worse dewatering characteristics, when compared to FGD-gypsum derived from wet limestone FGD systems [14].

2.1.3 Seawater FGD systems

The main idea behind seawater FGD system lies is taking advantage of natural alkalinity of seawater to neutralize SO_2 [1]. The seawater contains HCO_3^- and CO_3^{2-}, that helps to absorb SO_2 from the flue gas. The process can be described simply by following reactions:

$$SO_{2(g)} \leftrightarrow SO_{2(aq)} \tag{2.12}$$

$$SO_{2(aq)} + 2HCO_{3(aq)}^- + 1/2O_2 \leftrightarrow SO_{4(aq)}^{2-} + 2CO_{2(aq)} + H_2O_{(aq)} \tag{2.13}$$

To maintain appropriate pH level for oxidation process, the acidified absorber effluent is being mixed with extra seawater. The air is introduced to oxidize HSO_3^- and to remove dissolved CO_2. Before the seawater is disposed of to the sea, the water is saturated with oxygen and the pH level is neutralized [10]. In this process SO_4^{2-} is entirely dissolved in the seawater, thus there is no waste product, that is necessary to dispose of. This type of systems are capable of removing SO_2 with efficiencies ranging from 92% to 98% [10].

2.1.4 Dual-alkali Flue Gas Desulphurization systems

Double-alkali (or dual) scrubbing is yet another non-regenerable Flue Gas Desulphurization technique, that utilizes alkali solution based on sodium to abate SO_2 content in the flue gas stream [A2]. During the process, the Sulphur dioxide reacts with alkaline solution ($NaOH,\ Na_2SO_3\ and\ Na_2CO_3$) to mainly form $NaHSO_3\ and\ Na_2SO_3$. Sulphur dioxide is absorbed by the sodium alkali and the spent absorbing slurry is being regenerated with $CaCO_3$ or CaO – hence the name of this type of FGD system. In the process, $CaSO_4$ or calcium sulphite is being precipitated and discarded as a sludge, while the sodium solution is regenerated and reintroduced to the absorber. The double-alkali FGD systems may achieve up to 98% of SO_2 removal efficiency [A2].

2.1.5 Ammonia Flue gas Desulphurization systems

In this process, the Sulphur dioxide is absorbed owing to aqueous NH_3. As a result $(NH_4)_2SO_4$ is produced [, having quite high potential to find an application as a fertilizer by-product. On the other hand, this technique is expensive and taking under consideration developed industrialized countries there are plenty of other sources of this fertilizer though.

2.2 Dry or/and semi-dry Flue Gas Desulphurization systems

In those kind of systems, the gaseous stream containing Sulphur dioxide reacts with alkaline sorbent, generally CaO or $Ca(OH)_2$ [10], producing dry waste, that is usually easier to dispose of in comparison to waste resulting from wet FGD techniques.

2.2.1 Spray dry Flue Gas Desulphurization systems

The second most common Flue Gas Desulphurization system worldwide (11%) is spray dry adsorption, which generally is applied in smaller or medium capacity boilers fired with coal with low to medium Sulphur content (1.5 wt.%) [16]. In spray dry FGD systems Sulphur dioxide reacts with calcium oxide or $Ca(OH)_2$ sorbent, which is mixed with a surplus of water or used to produce lime slurry by slaking.

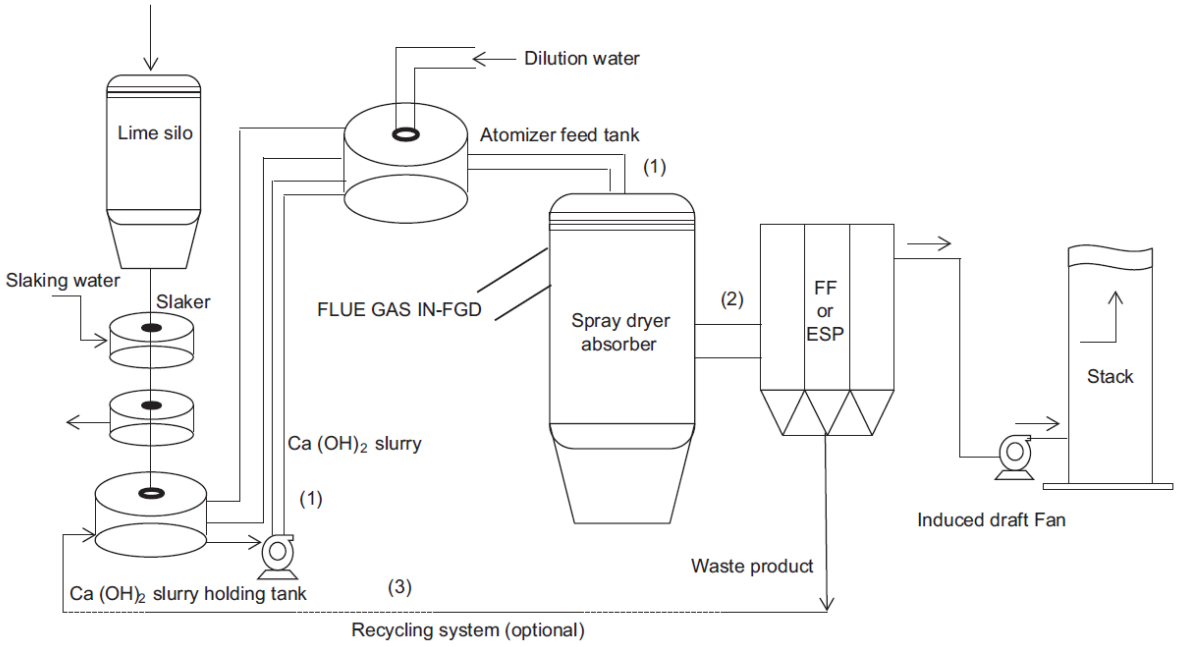

(1) Feeding of lime to the atomizer feed tank

(1) Lime slurry is sprayed into the scrubber to react with SO_2.

(2) Desulphurisation by-product is entrained in the flue gas and carried downstream toward a particulate collection device.

(3) Residue is recycled and mixed with fresh CaO slurry to enhance CaO utilisation

Figure 2.2 Conventional design and operation idea of a Spry dry-lime FGD system [1]

In the spray dry absorber, the lime slurry is fed in form of a cloud of fine droplets (1) and reacts with Sulphur dioxide. Provided that the water evaporates due to the high temperature of flue gas, there is no requirement to treat the waste water in the process. The main reactions during the process are as follow:

$$Ca(OH)_2 + SO_2 \leftrightarrow CaSO_3 + H_2O \quad (2.14)$$

$$Ca(OH)_2 + SO_3 \leftrightarrow CaSO_4 + H_2O \quad (2.15)$$

The Sulphur dioxide is absorbed into liquid and reacts as it was in a lime slurry process. Moreover, the secondary reaction takes place:

$$CaSO_3 + 1/2O_2 \leftrightarrow CaSO_4 \quad (2.16)$$

The obtained by-product, a dry mixture of $CaSO_4 \cdot 2H_2O$, $CaSO_3 \cdot 1/2H_2O$, fly ash and remaining lime is carried downstream with flue gas to a particulate collection device (2), usually fabric filter or ESP - electrostatic precipitator, though the latter achieves higher fly ash collection efficiencies when Sulphur-to-ash content is higher (due to lower electrical resistivity of the fly ash) [17, 18, 19]. The residue is then recycled (3) altogether with new CaO slurry to boost CaO utilization. The dry spray absorber systems are characterized by relative low costs and energy consumption (approx. 30-50% lower in comparison to wet limestone systems). On the other hand, the dry spray technique has high operational costs due to use of more expensive sorbent [20]. The Spray dry Flue Gas Desulphurization installations can achieve Sulphur dioxide removal efficiencies from 85% to 95% [10].

2.2.2 Furnace sorbent injection

Furnace sorbent injection desulphurization method is based on injecting a dry sorbent directly into the flue gas stream leaving the boiler [20]. Among other sorbents applied in this method are $CaCO_3$ and $CaCO_3 \cdot MgCO_3$. In the boiler, the process of sorbent calcinations produces reactive CaO particles. Sulphur dioxide reacts with the surface of produced CaO particles forming $CaSO_3$ and $CaSO_4$. Then, the products are removed altogether with fly ash by the particulate control device, often ESP (electrostatic precipitator) or fabric filter. The captured dry solid residue requires no further treatment before being disposed of to a landfill or applied as a construction material.

The Sulphur dioxide removal efficiency can achieve 50% when sorbent molar ratio (Ca/S) at 4-5 and the limestone is injected into the furnace at about optimum operation conditions. Though 70-80% removal efficiency can be obtained when recycling the reaction product [10]

2.2.3 Duct sorbent injection

Another dry FGD system, the duct sorbent injection involves injection of $Ca(OH)_2$ or $NaHSO_3$ into the flue gas downstream the air pre-heater and upstream the ESP (or other particulate control device, e.g. fabric filter). Though to further improve SO_2-sorbent reaction, water can be introduced into the gaseous stream before the sorbent injection [20]. Part of the produced residues, fly ash, reaction products, and any remaining sorbent collected by ESP (or fabric filter) are recirculated into the stream to enhance sorbent utilization, while the other part is discharged. The Suphur dioxide removal efficiencies varies depending on the sorbent applied in the process. The system that utilizes $Ca(OH)_2$ sorbent can achieve 50-60% of capture efficiency. The SO_2 removal efficiency using $NaHSO_3$ as a sorbent is expected to be approximately 80%.

2.2.4 Circulating fluidized bed (CFB) dry scrubber

The Circulating fluidized bed dry scrubber is characterized by the fact that in addition to coal, CaO, $Ca(OH)_2$, or $CaCO_3$ are inserted into circulating fluidized bed reactor. In circulating fluidized bed reactor the air is introduced from the bottom of the reactor, resulting in rise to the bed. This results in long contact time between flue gas and sorbent due to the fact that the sorbent flows through the bed a few times. Additionally, the higher speed stream enables entrainment of reaction products to flow to the particulate control device [10].

The CDB systems significantly impact the potential reaction time and the degree to which the gas can be mixed, that result in efficient combustion and fixation of Sulphur. The SO_2 removal efficiency can reach 98% [10]

2.3 The impact of the operational conditions of wet limestone flue gas desulphurization systems

In terms of economic viability, the two most essential indicators in wet limestone FGD systems are Sulphur dioxide removal efficiency and the residual limestone level of the FGD-gypsum [21]. However, the most significant physical factors impacting the design and operation of a wet limestone FGD installations can be listed as liquid-to-gas ratio, the absorber gas velocity, and the oxidation fraction [22]. The chemistry factors that influences the operational conditions of wet limestone FGD systems are the limestone reactivity, SO_2 concentration in flue gas, the reaction tank pH level, the temperature of the scrubber, HCI, HF and the application of additives. Other operation parameters that affect the wet limestone FGD installations are residence time, recycling or water treatment, particulate control device efficiency and proper oxidation process.

3. Numerical flue gas flow modelling

Generally, fluid flow is described by Navier-Stokes equations, that are a set of coupled nonlinear partial differential equations that originate form fundamental laws of conservation of mass, momentum and energy. The flow velocity, pressure, density and temperature are most commonly unknown, hence it is often impossible to find an analytical solution. In such case, the scientists often try to find an empirical solution in the laboratory by conducting appropriate experiments. Though not always is it possible and easy to get correct solution in such situations. The answers can vary due to difficulties in enforcing dynamic and geometric similitude between laboratory experiments and designed prototypes. Not only is it problematic but also costly in terms of design and construction. However, the scientists nowadays have an additional tool that brings an attractive alternative to these methods. Computational Fluid Dynamics is connected with numerical solution of differential equations that govern transport of mass, momentum and energy in fluid in motion [23]. CFD emerged and became an appealing alternative to existing solving methods altogether with the rising availability of computers in the beginning of 1960s [23]. Due to exponential development of

computational power of our computers, currently, Computational Fluid Dynamics is in a firm position alongside empirical and theoretical methods of finding a solution to Navier-Stokes equations – even if large and complex problems are involved. CFD finds its application in basic and applied research, in a process of designing of an engineering equipment, as well as computation of environmental and geophysical phenomena [23]. At the beginning of 1970s, commercial software packages and computer codes emerged and became available. As a result CFD became an severely important approach in engineering practice in various sectors, such as industry, defense, as well as in environmental organizations. For quite some time, the design process (including sizing, economic operation and safety) of engineering equipment depended on difficult to obtain empirical information. Similarly, various industrial processes relied on experimental data in terms of design. The experimental information is generally presented as correlations, tables and/or monograms between essential variables. Such records is highly appreciated by designers and consultants [24]. However, the empirical records are only available in limited range of values of fluid velocity, temperature, time and/or length for which it is needed. Therefore, to scale up, for instance higher capacity power plant or just to design turbines with higher dimensions, the new experimental data was necessary. The process of acquiring these information is very troublesome and demanding. It involved generating the data through laboratory-scale models. Hence the new scaling laws were needed to reflect geometric, kinematic and dynamic similarities between the model and the real-size equipment. The process not only required significant experience but also ingenuity. Thus, the process had to be supplemented with flow-visualization research and by simplified (generally one-dimensional) analytical solutions to equations that govern the examined phenomena. In addition, due to the activity being expensive, such information is usually widely unavailable and of proprietary kind. Recently, the challenge of scaling was set into opposite direction. As electronic equipment is getting smaller, the process of scaling down is gaining its relevance. For instance, in materials processing, where the most relevant phenomena takes place at microscales – even further – at molecular or atomic scales, where at this point the continuum assumption no longer abides. Other than that, smaller scale phenomena occur in biocells [23].

To conclude, the scientists and designers would highly appreciate a design tool, which would be scale neutral. Not only the tool has to be scientific but also economically affordable and viable. Obtaining scale neutrality can be hardly possible for an individual designers and scientists. Fortunately, information scale neutrality is acquirable by the fundamental laws of conservation of mass, momentum and energy. The answer is to find a solution to differential equations governing these laws and subsequently interpret it for practical design. Since the fundamental laws has been invented about 200 years ago, its (not omitting other connected with it empirical laws) potential in terms of obtaining data with scale neutrality has been known for so long too. However, only recently the potential to solve the essential differential equations has been recognized due to higher computers availability. The recent six decades have showed tremendous improvement in computational speed that can be carried out on a computer [23].

3.1 Fluid dynamics equations

To start with, there are three laws governing transport, namely the law of conservation of mass, Newton's second law of motion (conservation of momentum) and the first law of thermodynamics (transport of energy). These laws are applied to an infinitesimally small control volume situated in a fluid in motion (elemental fluid). The aforementioned application leads to partial differential equations of transport of mass, momentum and energy. There is two possible approaches, namely, a particle approach and a continuum approach [23].

In the first one, there is assumption that the fluid is structured by particles (molecules, atoms, etc.). The laws are utilized to examine fluid motion. Furthermore, the motion of the fluid, is expressed via statistically averaged motion of a group of particles [23]. The most common is application of Avogadro's number, which says that at normal conditions (normal temperature and pressure) a gas will have $6.022 \cdot 10^{26}$ molecules per kmol. Thus, according to this, for instance the air will contain 10^{16} molecules per mm^3. However, in majority of practical situations in engineering and environment, a particle approach is very inconvenient, since the essential dimensions of the flow are significantly larger than the length of the mean-free-path between molecules.

In the latter, in a continuum approach has been assumed that the statistical averaged motion has been already done and the fundamental laws has been introduced into portions of fluid (alternatively called control volumes) that consist of a higher number of molecules. However, the information about length of the mean-free-path has to be somehow recovered. The other auxiliary laws and experimentally obtained specifications of transport properties (viscosity, thermal conductivity and mass diffusivity) have to include the lost information. The properties of the fluid transport are usually obtained empirically. Therefore, the continuum approach can appear attractive, because when relating to temperature, pressure, velocity at given point, one can correlate it to the values measured by majority of the practical instruments. To decide to whether use the continuum or particle approach can be answered by Knudsen number:

$$K_n = \frac{l}{L} \tag{3.1}$$

where l is the length of mean-free-path between particles and L is a flow characteristic dimension [23]. If the Knudsen number is smaller than 10^{-5} the continuum approach is regarded as correct. Thus, as far as engineering and environmental flows are considered, the continuum approach is applied.

3.2 Transport equations

The chapter covers a mathematical representation of fluid flow derived from laws of conservation of mass and momentum. Not only does it cover the fluid motion governing equations but also discussion about necessary initial boundary conditions. It includes the derivation of the system of partial differential equations (PDEs) governing the fluid flow in Cartesian (x, y, z) coordinates , the Newton model of viscous stresses that concludes in Navier-Stokes equations, the connection between the PDEs and the transport

equation definition, integrated forms of the transport equation over a finite control volume and finite time interval, proper boundary conditions for a few categories…

Generally, the fluid flow governing equations reflect mathematical statements of conservation of laws of physics. Namely, the mass of a fluid is conserved, the rate of change of momentum have to be equal to the sum of the forces on a fluid particle (Newton's second law), the rate of energy change have to be equal to the sum of the rate of heat input and of work that is done by the fluid particles (first law of thermodynamics) [25, 26]. Since we analyze the industrial engineering problem the fluid will be considered as a continuum (see Knudsen number in previous chapter). Thus, we will be regarding the fluid properties (velocity, pressure, density and temperature) at macroscopic scale, basically as an average of space and time over large number of molecules. Therefore, a fluid is considered the smallest element, and its properties in further calculations are not influenced by individual molecules.

The Figure 3.1 presents the considered small element of fluid, with sides marked as $\delta x, \delta y \; and \; \delta z$:

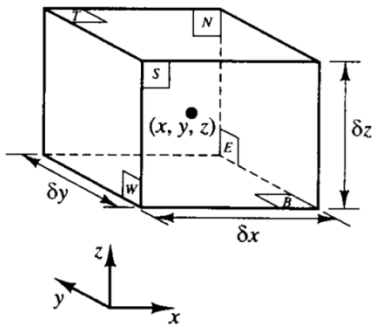

Figure 3.1 Fluid element representation for conservation laws [25]

The respective faces are labeled as N (North), S (South), E (East), W (West), T (top), B (bottom).The Cartesian coordinate axes directions are also presented. The centre of the element is positioned in point (x, y, z). Basically, fluid flow equations are just a systematized record of changes in the mass, momentum and energy of the fluid element, caused by fluid flow across its boundaries and (in some cases) the action of sources inside the fluid element.

Even though, every fluid property is a function of space and time, thus should be described appropriately $\rho(x, y, z, t)$, $p(x, y, z, t)$, $T(x, y, z, t)$,$\boldsymbol{u}(x, y, z, t)$(respectively density, pressure, temperature and velocity vector),such convention would be severely inconvenient and somehow cumbersome. In order to simplify the notation, the dependences on space coordinates and time will not be explicitly stated in future in this thesis (unless specified otherwise). For example, the density at point (x, y, z) of a fluid element at time t will be written as ρ and the x-derivative of, e.g. pressure at centre (x, y, z) and time t as $\partial p/\partial x$. This convention of notation is applied to the rest of the fluid properties.

The considered fluid element is so small that the aforementioned properties at the faces can be mathematically represented with sufficient accuracy by first two terms of a Taylor series expansion. Notably, the pressure at faces E and W, that are displaced by 0.5 δx from the point (x, y, z), can be written as:

$$p - \frac{\partial p}{\partial x}\frac{1}{2}\partial x \qquad \text{and} \qquad p + \frac{\partial p}{\partial x}\frac{1}{2}\delta x. \tag{3.2}$$

3.2.1 Three dimensional mass conservation equation

To determine the mass conservation PDE, mass balance has to be prepared for considered fluid element. The rate of increase of mass in fluid element has to be equal to the net rate of flow of mass into fluid element. The rate of increase of mass in the fluid element can be expressed as

$$\frac{\partial}{\partial t}(\rho \delta x \delta y \delta z) = \frac{\partial \rho}{\partial t}\delta x \delta y \delta z \tag{3.3}$$

Subsequently, it is necessary to determine mass flow rate across a face of the fluid element, that is equal to the product of density, area, and the velocity component normal to the face. The Figure 3.2 shows that the net rate of flow of mass into the fluid element across its boundaries (positive sign – mass flows in; negative sign - mass flows out) is determined as

$$\left(\rho u - \frac{\partial(\rho u)}{\partial x}\frac{1}{2}\,\delta x\right)\delta y\delta z - \left(\rho u - \frac{\partial(\rho u)}{\partial x}\frac{1}{2}\,\delta x\right)\delta y\delta z + \left(\rho v - \frac{\partial(\rho v)}{\partial y}\frac{1}{2}\,\delta y\right)\delta x\delta z - \left(\rho v - \frac{\partial(\rho v)}{\partial y}\frac{1}{2}\,\delta y\right)\delta x\delta z + \left(\rho w - \frac{\partial(\rho w)}{\partial z}\frac{1}{2}\,\delta z\right)\delta x\delta y - \left(\rho w - \frac{\partial(\rho w)}{\partial z}\frac{1}{2}\,\delta z\right)\delta x\delta y. \tag{3.4}$$

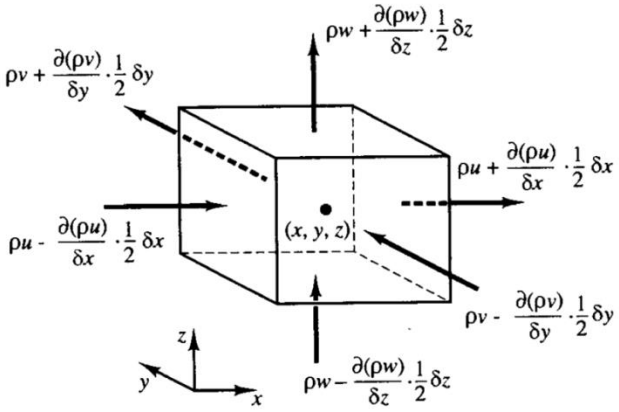

Figure 3.2 Mass flows into and out of fluid element [25]

After comparing equations 3.3 and 3.4, arranging all the terms on the left hand side, as well as dividing both sides by element volume $\delta x \delta y \delta z$ one can arrive at following equation:

$$\frac{\partial \rho}{\partial t} + \frac{\partial(\rho u)}{\partial x} + \frac{\partial(\rho v)}{\partial y} + \frac{\partial(\rho w)}{\partial z} = 0 \tag{3.5}$$

The equation 3.5 can be also expressed in vector notation

$$\frac{\partial \rho}{\partial t} + \mathrm{div}(\rho \boldsymbol{u}) = 0 \tag{3.6}$$

The equation 3.6 presents the generalized compact version of the mass conservation equation. The equation describes unsteady, three-dimensional continuity equation at a centre point in fluid element in a compressible fluid. To put it more simple, the left hand side of the equation reflects the rate of change in time of the density (first term) and the net flow of mass out of the fluid element across its boundaries (second, convective term). To model the flow of incompressible fluid (where the density is constant), the equation 3.6 can be simplified to a following form

$$div(\boldsymbol{u}) = 0. \tag{3.7}$$

Alternatively, the equation 3.7 can also be written in elongated notation

$$\frac{\partial u}{\partial x} + \frac{\partial v}{\partial y} + \frac{\partial w}{\partial z} = 0 \tag{3.8}$$

The symbol $\boldsymbol{u} = [u, v, w]^T$ in equations 3.6, 3.7 is a particle velocity column matrix. Furthermore, after simplification of the equation and application of divergence theorem the equation 3.5 takes following form:

$$\frac{\partial}{\partial t}\int_V \rho dV + \int_S \rho \boldsymbol{u} \cdot \boldsymbol{n} dS = 0, \tag{3.9}$$

where:

$$\boldsymbol{n} = \left[n_x, n_y, n_z\right]^T \tag{3.10}$$

is considered an external normal unit vector and S is a area closing external surface of an element with volume V. It is worth noting, that symbol "·" is equivalent with scalar product of two vectors, where the first one is (left hand side of the sign) is regarded as row vector and the second (right hand side of the sign) is considered a column vector.

3.2.2 Rates of change of fluid properties

The subchapter will consider rates of change of properties following a fluid particle and a fluid element, that conclude from the mass and energy conservation statements. To start with, the fluid particle will be considered. Every property of fluid particle is a function of the time t and particle position (x, y, z). To shorten the notation, a given property with respect to unit mass will be denoted as ϕ. The total (substantive) derivative of fluid property per unit mass with respect to time for a particle has form

$$\frac{D\phi}{Dt} = \frac{\partial \phi}{\partial t} + \frac{\partial \phi}{\partial x}\frac{dx}{dt} + \frac{\partial \phi}{\partial y}\frac{dy}{dt} + \frac{\partial \phi}{\partial z}\frac{dz}{dt} \tag{3.11}$$

The respective derivatives of a position change over time is just particle velocities, thus $dx/dt = u$, $dy/dt = v$, $dx/dt = w$ and the total derivative of fluid property per unit mass with regard to time $D\phi/Dt$ is

$$\frac{D\phi}{Dt} = \frac{\partial \phi}{\partial t} + u\frac{\partial \phi}{\partial x} + v\frac{\partial \phi}{\partial y} + w\frac{\partial \phi}{\partial z} = \frac{\partial \phi}{\partial t} + \boldsymbol{u}.grad\phi \quad (3.12)$$

However, in this case, the equation above would be more convenient if regarded in respect to unit volume rather than unit mass. Therefore, the rate of change of given fluid property ϕ per unit volume for a particle is a product of density and the aforementioned substantive derivative of ϕ with respect to time

$$\rho\frac{D\phi}{Dt} = \rho\left(\frac{\partial \phi}{\partial t} + \boldsymbol{u}.grad\phi\right) \quad (3.13)$$

Secondly, the fluid element, which is fixed in space will be considered. This form is the most used and convenient representation of conservation laws of a fluid flow properties. The dependence between the total derivative of ϕ, that follows a fluid particle and the rate of change of fluid element properties per unit mass will be investigated. Since the conservation of mass equation includes the mass with respect to unit volume (density) as a representation of conserved quantity, then the sum of the rate of change of density and the convective term in equation 3.6 have following form

$$\frac{\partial \rho}{\partial t} + div(\rho\boldsymbol{u}) \quad (3.14)$$

Therefore, the general representation of these terms for an conserved fluid property per unit mass is

$$\frac{\partial(\rho\phi)}{\partial t} + div(\rho\phi\boldsymbol{u}) \quad (3.15)$$

This form represents the rate of change of ϕ per unit volume summed with the net flow of ϕ out of the fluid element in regard to time t. Alternatively, it can be expressed as

$$\frac{\partial(\rho\phi)}{\partial t} + div(\rho\phi\boldsymbol{u}) = \rho\left[\frac{\partial \phi}{\partial t} + \boldsymbol{u}\cdot grad\ \phi\right] + \phi\left[\frac{\partial \rho}{\partial t} + div(\rho\boldsymbol{u})\right] = \rho\frac{D\phi}{Dt} \quad (3.16)$$

The mass conservation law implies that the term $\phi[\partial\rho/\partial t + div(\rho\boldsymbol{u})]$ is equal to zero.The equation 3.16 can be described as: sum of the rate of increase of ϕ of fluid element and the net rate of flow of ϕ out of fluid element equals to the rate of increase of $\phi$for a fluid particle.

To arrive at law of conservation of momentum and energy, it is necessary to introduce essential entries for $\phi$and define their rates of change per unit volume. The information in contained in the Table 3.1

Table 3.1 The components of the momentum and energy equation constructed for relevant entries for ϕ and their rate of change per unit volume [25]

Equation component		The rate of change per unit volume	
x-momentum	u	$\rho\frac{Du}{Dt}$	$\frac{\partial(\rho u)}{\partial t} + div(\rho u\boldsymbol{u})$
y-momentum	v	$\rho\frac{Dv}{Dt}$	$\frac{\partial(\rho v)}{\partial t} + div(\rho v\boldsymbol{u})$
z-momentum	w	$\rho\frac{Dw}{Dt}$	$\frac{\partial(\rho w)}{\partial t} + div(\rho w\boldsymbol{u})$

Energy	E	$\rho\frac{DE}{Dt}$	$\frac{\partial(\rho E)}{\partial t} + div(\rho E\boldsymbol{u})$

Alternatively, the conservative (divergence) and non-conservative approach can be used to express the rate of change in regard to an arbitrary property change per unit volume in fluid element/particle.

3.2.3 Three dimensional momentum conservation equation

The law of conservation of momentum is derived from Newton's second law, which states that the rate of change of momentum of a fluid particle is equal to the sum of forces applied on the particle. The mentioned rates of change of x, y, z- momentum referred to an unit of volume of a fluid particle are accordingly: $\frac{\rho Du}{Dt}$, $\frac{\rho Dv}{Dt}$, $\frac{\rho Dw}{Dt}$. There are two main types of the forces that act on a fluid particles: surface forces (pressure, viscous forces) and body forces (gravity, centrifugal, Coriolis, electromagnetic forces). It has become a standard to include the surface forces as separate termsin the momentum equation and the body forces as source terms. The stresses in a fluid element are highlighted by the pressure and viscous stress components as shown in the Figure 3.3. The notation adopted for those quantities are as follows: the pressure p (being a normal stress), viscous stresses τ_{ij} with suffixes indicating the direction (stress component act on the j-direction, that is normal to the i-direction)[25, 27].

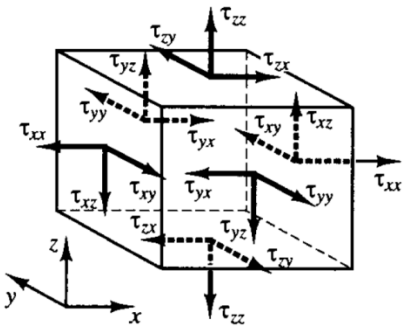

Figure 3.3 Fluid element and the stress component that act on its three faces [25]

To start with, let's consider the x-components of the force related to pressure and stresses τ_{xx}, τ_{yx} and τ_{zx}. The value (magnitude) of a force that results from a surface stress is the product of stress and area. Forces in direction marked in accordance with the co-ordinate axis have a positive sign and the opposite direction forces have a negative sign. The overall net force in the direction x is equal to the sum of the force components that act on the fluid element in x-direction. The above statements are represented by the Figure 3.4.

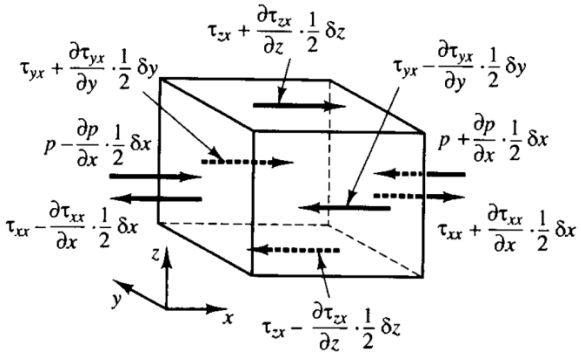

Figure 3.4 The force (stress) components presented for the x-direction [25]

For the pair of face E and face W as marked on the Figure 3.4 we obtain:

$$\left[\left(p - \frac{\partial p}{\partial x}\frac{1}{2}\delta x\right) - \left(\tau_{xx} - \frac{\partial \tau_{xx}}{\partial x}\frac{1}{2}\delta x\right)\right]\delta y\delta z + \left[-\left(p + \frac{\partial p}{\partial x}\frac{1}{2}\delta x\right) + \left(\tau_{xx} + \frac{\partial \tau_{xx}}{\partial x}\frac{1}{2}\delta x\right)\right] =$$

$$= \left(-\frac{\partial p}{\partial x} + \frac{\partial \tau_{xx}}{\partial x}\right)\delta x\delta y\delta z \tag{3.17}$$

The net force in the direction x on faces N and S:

$$-\left(\tau_{yx} - \frac{\partial \tau_{yx}}{\partial y}\frac{1}{2}\delta y\right)\delta x\delta z + \left(\tau_{yx} + \frac{\partial \tau_{yx}}{\partial y}\frac{1}{2}\delta y\right)\delta x\delta z = \frac{\partial \tau_{yx}}{\partial y}\delta x\delta y\delta z \tag{3.18}$$

Consequently, the net force in direction x on faces T and B:

$$-\left(\tau_{zx} - \frac{\partial \tau_{zx}}{\partial z}\frac{1}{2}\delta z\right)\delta x\delta y + \left(\tau_{zx} + \frac{\partial \tau_{zx}}{\partial z}\frac{1}{2}\delta z\right)\delta x\delta y = \frac{\partial \tau_{zx}}{\partial z}\delta x\delta y\delta z \tag{3.19}$$

When summing equations 3.17, 3.18, 3.19 and dividing by the volume of a fluid particle $\delta x\delta y\delta z$ we obtain the total force per unit volume that acts on the fluid particles (resulting from the surface stresses):

$$\frac{\partial(-p+\tau_{xx})}{\partial x} + \frac{\partial \tau_{yx}}{\partial y} + \frac{\partial \tau_{zx}}{\partial z} \tag{3.20}$$

In order to simplify further considerations and to somehow include the body forces, a source can be defined as S_{Mx} of x-momentum per unit volume per unit time. Taking this under consideration we arrive at the x-component of the momentum equation:

$$\rho\frac{Du}{Dt} = \frac{\partial(-p+\tau_{xx})}{\partial x} + \frac{\partial \tau_{yx}}{\partial y} + \frac{\partial \tau_{zx}}{\partial z} + S_{Mx} \tag{3.21}$$

Analogically, the y-component and z-component of the momentum equation have accordingly following forms:

$$\rho\frac{Dv}{Dt} = \frac{\partial(-p+\tau_{xy})}{\partial x} + \frac{\partial \tau_{yy}}{\partial y} + \frac{\partial \tau_{zy}}{\partial z} + S_{My} \tag{3.22}$$

$$\rho \frac{Dw}{Dt} = \frac{\partial(-p+\tau_{xz})}{\partial x} + \frac{\partial \tau_{yz}}{\partial y} + \frac{\partial \tau_{zz}}{\partial z} + S_{Mz} \quad (3.21)$$

To give an example of inclusion of body forces, let's assume the gravity force g in z-direction. Then the proper body forces sources would be equal to: $S_{Mx} = 0, S_{My} = 0$ and $S_{Mz} = -\rho g$.

3.2.4 Three dimensional energy conservation equation

Applying the first law of thermodynamics to our fluid particle we can make following statement: the rate of increase of energy of a fluid particle in equal to the sum of the net rate of heat added to a fluid particle and the net rate of work done on a fluid particle. Let's assume the rate of increase of energy of a fluid particle in regard to unit volume as$\rho \frac{DE}{Dt}$.

Secondly, the rate of work done on the fluid particle in the element by a surface forces has to be defined. Namely, it is a product of the force and velocity component in the direction being in accordance of the direction of the force:

$$\left[\left(pu - \frac{\partial(pu)}{\partial x}\frac{1}{2}\delta x\right) - \left(\tau_{xx}u - \frac{\partial(\tau_{xx}u)}{\partial x}\frac{1}{2}\delta x\right) - \left(pu + \frac{\partial(pu)}{\partial x}\frac{1}{2}\delta x\right) + \left(\tau_{xx}u + \frac{\partial(\tau_{xx}u)}{\partial x}\frac{1}{2}\delta x\right)\right]\delta y\delta z + \left[-\left(\tau_{yx}u - \frac{\partial(\tau_{yx}u)}{\partial y}\frac{1}{2}\delta y\right) + \left(\tau_{yx}u - \frac{\partial(\tau_{yx}u)}{\partial y}\frac{1}{2}\delta y\right)\right]\delta x\delta z + \left[-\left(\tau_{zx}u - \frac{\partial(\tau_{zx}u)}{\partial z}\frac{1}{2}\delta z\right) + \left(\tau_{zx}u - \frac{\partial(\tau_{zx}u)}{\partial z}\frac{1}{2}\delta z\right)\right]\delta x\delta y. \quad (3.22)$$

Considering only x-direction surface forces, the net rate of work done by them is

$$\left[\frac{\partial[u(-p+\tau_{xx})]}{\partial x} + \frac{\partial(u\tau_{yx})}{\partial y} + \frac{\partial(u\tau_{zx})}{\partial z}\right]\delta x\delta y\delta z \quad (3.23)$$

One has to take under consideration the y- and z-direction surface forces since they affect the fluid particle (they do work on the particle). Thus, rates of work done on the fluid particle caused by surface forces of accordingly y- and z-direction:

$$\left[\frac{\partial(v\tau_{xy})}{\partial x} + \frac{\partial[v(-p+\tau_{yy})]}{\partial y} + \frac{\partial(v\tau_{zy})}{\partial z}\right]\delta x\delta y\delta z \quad (3.24)$$

$$\left[\frac{\partial(v\tau_{xy})}{\partial x} + \frac{\partial[v(-p+\tau_{yy})]}{\partial y} + \frac{\partial(v\tau_{zy})}{\partial z}\right]\delta x\delta y\delta z \quad (3.25)$$

Subsequently, by summing and dividing the equations 3.23, 3.24 and 3.25 by the volume $\delta x\delta y\delta z$, we obtain:

$$-\frac{\partial(up)}{\partial x} - \frac{\partial(vp)}{\partial y} - \frac{\partial(wp)}{\partial z} = -div(p\boldsymbol{u}) \quad (3.26)$$

The resulting equation 3.26 is the total rate of work done per unit volume on the fluid particle by the surface forces. Lastly, the total rate of work done on the fluid particle by all the surface stresses has a following form

$$[-div(p\boldsymbol{u})] + \left[\frac{\partial(u\tau_{xx})}{\partial x} + \frac{\partial(u\tau_{yx})}{\partial y} + \frac{\partial(u\tau_{zx})}{\partial z} + \frac{\partial(v\tau_{xy})}{\partial x} + \frac{\partial(v\tau_{yy})}{\partial y} + \frac{\partial(v\tau_{zy})}{\partial z} + \frac{\partial(w\tau_{xz})}{\partial x} + \frac{\partial(w\tau_{yz})}{\partial y} + \frac{\partial(w\tau_{zz})}{\partial z}\right] \quad (3.27)$$

To continue further consideration of three dimensional conservation of energy equation, energy flux connected to the conduction has to be defined. The heat flux vector will be denoted **q**. The vector's three components are q_x, q_y and q_z.

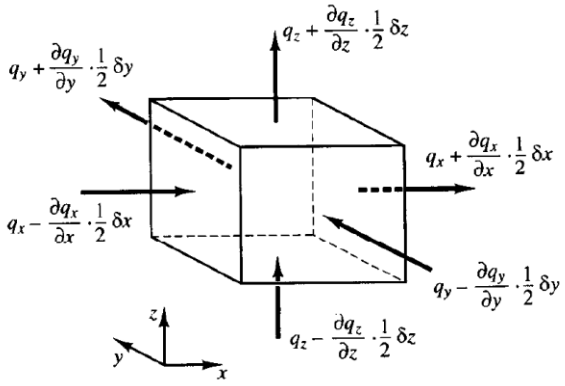

Figure 3.5 The heat flux vector components [25]

Taking under consideration x-directional heat flow, the net rate of heat transfer to the fluid particle is the difference of the rate of heat inputted through face W and the rate of heat lost through face E. It can be described as

$$\left[\left(q_x - \frac{\partial q_x}{\partial x}\frac{1}{2}\delta x\right) - \left(q_x + \frac{\partial q_x}{\partial x}\frac{1}{2}\delta x\right)\right]\delta y\delta z = -\frac{\partial q_x}{\partial x}\delta x\delta y\delta z \tag{3.28}$$

Analogically, the net rate of heat transfer to the fluid particle in directions y- and z- are accordingly

$$-\frac{\partial q_y}{\partial y}\delta x\delta y\delta z \tag{3.29}$$

$$-\frac{\partial q_z}{\partial z}\delta x\delta y\delta z \tag{3.30}$$

Therefore, after summation of equations 3.28, 3.29 and 3.30 and division by the volume $\delta x\delta y\delta z$

$$-\frac{\partial q_x}{\partial x} - \frac{\partial q_y}{\partial y} - \frac{\partial q_z}{\partial z} = -div\,\boldsymbol{q} \tag{3.31}$$

Which is the total rate of the heat inputted to the fluid particle in relation to unit of volume caused by the heat flow through its faces. Referring to Fourier's law, we can correlate the heat flux with the local temperature gradient. Thus, we can write the heat flux vector's three components as

$$q_x = -k\frac{\partial T}{\partial x} \tag{3.27}$$

$$q_y = -k\frac{\partial T}{\partial y} \tag{3.28}$$

$$q_z = -k\frac{\partial T}{\partial z} \tag{3.29}$$

or alternatively in vector form

$$\boldsymbol{q} = -k\ grad\ T \tag{3.30}$$

Therefore, taking under consideration equations 3.30 and 2.26

$$-div\ \boldsymbol{q} = div(k\ grad\ T) \tag{3.31}$$

The above equation (3.31) is the rate of heat addition to the fluid particle related to heat conduction through the element surfaces.

Yet, the specific energy of a fluid has to be defined. Usually, the energy of the fluid is written as a sum of internal, kinetic energy and potential energy. Let's denote the specific energy of the fluid as E, the internal energy as i, kinetic energy $\frac{1}{2}\ (u^2 + v^2 + w^2)$. The definition of the specific energy of the fluid can be modeled in two ways. One is that we regard the fluid element that stores the gravitational potential energy. Another one is to consider the gravitational force as a body force, acting (doing work) on the fluid element, which goes through the gravitational field. Here the latter approach will be considered. The impact of the potential energy changes will be included as a source term. The source of energy per unit volume per unit time will be denoted as S_E. Law of conservation of energy is reflected here as the rate of change of energy of the fluid particle equated to the sum of the net rate of work done on the fluid particle and the summation of the net rate of heat added to the fluid element and the rate of increase of energy connected to source terms. Therefore, the energy equation will take following form

$$\rho \frac{DE}{Dt} = -div\ (p\boldsymbol{u}) + \left[\frac{\partial(u\tau_{xx})}{\partial x} + \frac{\partial(u\tau_{yx})}{\partial y} + \frac{\partial(u\tau_{zx})}{\partial z} + \frac{\partial(v\tau_{xy})}{\partial x} + \frac{\partial(v\tau_{yy})}{\partial y} + \frac{\partial(v\tau_{zy})}{\partial z} + \frac{\partial(w\tau_{xz})}{\partial x} + \frac{\partial(w\tau_{yz})}{\partial y} + \frac{\partial(w\tau_{zz})}{\partial z}\right] + div(k\ grad\ T) \tag{3.32}$$

In the approach taken here, the specific energy of a fluid is

$$E = i + \frac{1}{2}(u^2 + v^2 + w^2) \tag{3.33}$$

The equation 3.33 is correct and used widely, however, it is sometimes more practical to reflect the changes of the kinetic energy by the dependence on internal energy and temperature [25]. To arrive at conservation of kinetic energy equation one can simply multiply the appropriate x-, y-, z-momentum equations by respectively u, v, w velocity components and sum it up together. It results in

$$\rho \frac{D\left[\frac{1}{2}(u^2+v^2+w^2)\right]}{Dt} = -\boldsymbol{u} \cdot grad\ p + u\left(\frac{\partial(\tau_{xx})}{\partial x} + \frac{\partial(\tau_{yx})}{\partial y} + \frac{\partial(\tau_{zx})}{\partial z}\right) + v\left(\frac{\partial(\tau_{xy})}{\partial x} + \frac{\partial(\tau_{yy})}{\partial y} + \frac{\partial(\tau_{zy})}{\partial z}\right) + w\left(\frac{\partial(\tau_{xz})}{\partial x} + \frac{\partial(\tau_{yz})}{\partial y} + \frac{\partial(\tau_{zz})}{\partial z}\right) + \boldsymbol{u} \cdot \boldsymbol{S_M} \tag{3.34}$$

In order to get the internal energy equation, let's subtract the equations 3.34 and 3.33

$$\rho \frac{Di}{Dt} = div(k\ grad\ T) + \tau_{xx} \frac{\partial u}{\partial x} + \tau_{yx} \frac{\partial u}{\partial y} + \tau_{zx} \frac{\partial u}{\partial z} + \tau_{xy} \frac{\partial v}{\partial x} + \tau_{yy} \frac{\partial v}{\partial y} + \tau_{zy} \frac{\partial v}{\partial z} +$$

$$+\tau_{xz} \frac{\partial w}{\partial x} + \tau_{yz} \frac{\partial w}{\partial y} + \tau_{zz} \frac{\partial w}{\partial z} + S_i \quad (3.35)$$

When considering an incompressible fluid the internal energy $i = cT$, (c being specific heat), and $div\ \boldsymbol{u} = 0$. In such special case the equation above can be rewritten to obtain a temperature equation

$$\rho c \frac{DT}{Dt} = div(k\ grad\ T) + \tau_{xx} \frac{\partial u}{\partial x} + \tau_{yx} \frac{\partial u}{\partial y} + \tau_{zx} \frac{\partial u}{\partial z} + \tau_{xy} \frac{\partial v}{\partial x} + \tau_{yy} \frac{\partial v}{\partial y} + \tau_{zy} \frac{\partial v}{\partial z} +$$

$$+\tau_{xz} \frac{\partial w}{\partial x} + \tau_{yz} \frac{\partial w}{\partial y} + \tau_{zz} \frac{\partial w}{\partial z} + S_i \quad (3.36)$$

In case of compressible fluid in many instances the equation 3.33 is rewritten to obtain an enthalpy equation. In order to do that let's introduce the notation for specific enthalpy h and the specific total enthalpy h_0 of the fluid such that

$$h = i + p/\rho \qquad \text{and} \quad (3.37)$$

$$h_0 = h + \frac{1}{2}(u^2 + v^2 + w^2) \quad (3.38)$$

Thus, including two above equations and the specific energy equation:

$$h_0 = i + \frac{p}{\rho} + \frac{1}{2}(u^2 + v^2 + w^2) = E + \frac{p}{\rho} \quad (3.39)$$

Taking under consideration the equation 3.33 and 3.39 we can obtain another alternative form of the energy equation

$$\frac{\partial(\rho h_0)}{\partial t} + div(\rho h_0 \boldsymbol{u}) = div(k\ grad\ T) + \frac{\partial p}{\partial t} + \left[\frac{\partial(u\tau_{xx})}{\partial x} + \frac{\partial(u\tau_{yx})}{\partial y} + \frac{\partial(u\tau_{zx})}{\partial z} + \frac{\partial(v\tau_{xy})}{\partial x} + \frac{\partial(v\tau_{yy})}{\partial y} + \frac{\partial(v\tau_{zy})}{\partial z} + \frac{\partial(w\tau_{xz})}{\partial x} + \right.$$

$$\left. + \frac{\partial(w\tau_{yz})}{\partial y} + \frac{\partial(w\tau_{zz})}{\partial z}\right] + S_h. \quad (3.40)$$

3.2.5 Equations of state

The three dimensional fluid motion is governed by transport equations, that in practice are a system of five PDEs, namely the mass conservation equation, the three (x-, y-, z-) momentum equations and the energy equation. There are following thermodynamics unknowns ρ, p, i and T.In this chapter the connection between these variables is being discussed. To obtain linkage between thermodynamic variables, the assumption of thermodynamic equilibrium can be used. When the fluid velocity is low enough, often the fluid can adapt its properties so quickly that sometimes the assumption that the fluid is in thermodynamics equilibrium can be sufficient to obtain accurate approximation. However, there are some exceptions, for instance flows with strong shockwaves, but in some cases even here the assumption of thermodynamic equilibrium can be accurate enough [27].

When the fluid is in thermodynamic equilibrium, its state can be characterized by only two state variables. Equations of state correlate two state variables to the remaining ones. Notably, if density and temperature is used, the state equation for specific internal energy and pressure look like

$$i = i(\rho, T) \tag{3.41}$$

$$p = p(\rho, T) \tag{3.42}$$

In case when the fluid can be modeled as a perfect gas, following equations of state can be used

$$p = \rho R T \tag{3.43}$$

$$i = C_v T \tag{3.44}$$

If the assumption of thermodynamic equilibrium is applied, two thermodynamic state variables are eliminated from the PDEs. Furthermore, when modeling a flow of a compressible fluid the equations of state allow to correlate the energy, mass, as well as momentum equations due to resulting density variations concerned with the pressure and temperature changes in the flow field[25, 28].

Often, when the low speed flow of liquids and gases is concerned, there is a possibility to assume the fluid is incompressible. The assumption eliminates the mentioned density variations and dispose of the correlation between energy equation, as well as mass and momentum conservation equations. Thus, the flow field can be calculated by regarding only mass and momentum equations. However, if the analyzed case includes heat transfer phenomenon, there is necessity to solve the energy equation as well [25, 29].

3.2.6 Transport equations roundup

To summarize, the conservative (or divergence) form of system of equations describing dependent on time compressible fluid flow and heat transfer in three dimensions of a Newtonian fluid has been shown below in Table 3.2

Table 3.2 Governing equations of the time-dependent three-dimensional flow of a compressible Newtonian fluid [25]

Mass	$\frac{\partial \rho}{\partial t} + \mathrm{div}(\rho \boldsymbol{u}) = 0$	(3.6)
x-momentum	$\frac{\partial(\rho u)}{\partial t} + div\,(\rho u \boldsymbol{u}) = -\frac{\partial p}{\partial x} + div\,(\mu\ grad\ u) + S_{Mx}$	(3.50)
y-momentum	$\frac{\partial(\rho v)}{\partial t} + div\,(\rho v \boldsymbol{u}) = -\frac{\partial p}{\partial y} + div\,(\mu\ grad\ v) + S_{My}$	(3.51)
z-momentum	$\frac{\partial(\rho w)}{\partial t} + div\,(\rho w \boldsymbol{u}) = -\frac{\partial p}{\partial z} + div\,(\mu\ grad\ w) + S_{Mz}$	(3.52)
Internal energy	$\frac{\partial(\rho i)}{\partial t} + div\,(\rho i \boldsymbol{u}) = -p\ div\ \boldsymbol{u} + div\,(k\ grad\ T) + \Phi + S_i$	(3.53)

Equations of state	$i = i(\rho, T)$	(3.41)
	$p = p(\rho, T)$	(3.42)
	$p = \rho RT$	(3.43)
	$i = C_v T$	(3.44)

Beside five flow PDEs, there are two supplementary algebraic equations obtained owing to equilibrium assumption. Furthermore, the Newtonian model provide the way to describe viscous stresses in terms of velocity gradients. It is worth noting, that at this point the system is mathematically closed since we got seven equations and seven unknowns. In other words, the system of equations can be solved if the proper auxiliary, initial and boundary conditions are specified [25, 31]

3.2.7 Integral and differential forms of the transport equations and introduction to Finite Volume Methods

When studying the table 3.2, it is not hard to realize there are many similarities between respective equations, that allow to rewrite the conservative forms of all fluid flow equations substituting the proper variables with a general variable ϕ. It also applies to equations including scalar quantities (temperature, pollutant concentration and so on). It is visible that the sum of the rate of increase of ϕ of fluid element and the net rate of flow of ϕ out of fluid element is equal to the sum of the rate of increase of ϕ due to diffusion and the rate of increase of ϕconcerned with sources [25, 27]. It can be written as

$$\frac{\partial(\rho\phi)}{\partial t} + div\,(\rho\phi\boldsymbol{u}) = div\,(\Gamma\, grad\,\phi) + S_\phi \tag{3.54}$$

The above equation is usually related to as transport equation for property ϕ. In the diffusive term of the equation, Γ is diffusion coefficient. The terms, that did not fit the equation 3.54 scheme had to be included (hidden) in source terms. It is worth noting that this equation can take another form, when applying the equation of state to replace internal energy with temperature. The equation 3.54 is a base for Computational Fluid Dynamics in Finite Volume Methods. Having ϕ set to be 1, u, v, w and i(alternatively T or h_0) and choosing suitable values for Γ and S_ϕ we get special form of the table 3.2 of five PDEs of interests (mass, momentum and energy conservation). Here is the integral form of equation 3.54:

$$\int_{CV} \frac{\partial(\rho\phi)}{\partial t} dV + \int_{CV} div\,(\rho\phi\boldsymbol{u}) dV = \int_{CV} div\,(\Gamma\, grad\,\phi) dV + \int_{CV} S_\phi dV \tag{3.55}$$

The control volume integrals: on the left hand side of the equation, the second (convective) term and on the right hand side, the first (diffusive) term have another form as integrals over the whole bounding surface of the CV by applying Gauss' (or Ostrogradsky's) divergence theorem [25, 30, 31]. The theorem states that for a given vector **a** the following

$$\int_{int} div\,\boldsymbol{a} dV = \int_A \boldsymbol{n}\cdot\boldsymbol{a} dA \tag{3.56}$$

In other words, $\boldsymbol{n} \cdot \boldsymbol{a}$ is the component of vector $\boldsymbol{a}$normal to surface dA and in the direction of the vector **n**. Therefore, the integral of the divergence of a given vector $\boldsymbol{a}$over given volume is equalized to the component of $\boldsymbol{a}$ in the direction normal to the surface that bounds the volume integrated over that bounding surface A. By using Ostrogradsky's divergence theorem the equation 3.55 can take following form

$$\frac{\partial}{\partial t}\left(\int_{CV} \rho\phi dV\right) + \int_A \boldsymbol{n} \cdot (\rho\phi\boldsymbol{u}) dA = \int_A \boldsymbol{n} \cdot (\Gamma\, grad\, \phi) dA + \int_{CV} S_\phi dV \tag{3.57}$$

The first (change) term reflects the rate of change of the total amount of fluid property ϕ in the CV (control volume), the second (convective) term the net rate of decrease of the fluid property ϕ of the fluid element connected to convection. Subsequently, on the right hand side, the first (diffusive) term is the net rate of increase of fluid property ϕ of the fluid element due to diffusion and the second (source) term is the rate of increase of property ϕ resulting from sources inside the fluid element. The integration of the PDEs has produced a statement concerning conservation of fluid property for a finite size (macro) volume [25].

In case of modelling steady state problems, the change term is zero. Thus, the steady transport equation in integral form is written as

$$\int_A \boldsymbol{n} \cdot (\rho\phi\boldsymbol{u}) dA = \int_A \boldsymbol{n} \cdot (\Gamma\, grad\, \phi) dA + \int_{CV} S_\phi dV \tag{3.58}$$

When problem is time-dependent, additionally there is necessity to integrate in regard to time over a small time interval Δt, for instance from t until $t + \Delta t$. At last, the general transport equation in integrated form is presented as

$$\int_\Delta \frac{\partial}{\partial t}\left(\int_{CV} (\rho\phi dV)\right) dt + \int_{\Delta t}\int_A \boldsymbol{n} \cdot (\rho\phi\boldsymbol{u}) dA\, dt = \int_{\Delta t}\int_A \boldsymbol{n} \cdot (\Gamma\, grad\, \phi) dA\, dt + \int_{\Delta t}\int_{CV} S_\phi dV\, dt \tag{3.59}$$

3.3 Turbulence modeling

All fluid flows in industrial and engineering practice, can become unstable provided high enough Reynolds number$Re = UL/\nu$, where U is a characteristic velocity and L is characteristic length scales of the mean flow, as well as the kinematic viscosity is denoted as ν. When the Reynolds number is low, the flows are laminar. When the Reynolds number is getting higher the flows are becoming turbulent, resulting in chaotic, irregular flow and velocity and pressure fluctuations in time in significantly substantial regions of the fluid flow [25, 32].

If the flow is laminar, it suffices to base the model on the equations in previous chapter (Table 3.2). If the problem is simple enough it can be solved by analytical approach [30]. However, if it is more complex, it is common practice to develop the numerical model applying finite volume method, even without extra approximations [25, 32].It is safe to say that most of the flows in engineering and industrial field are turbulent. Thus, the problem of turbulence modeling is not just a theoretical challenge but also an essential to everyday engineering practice.

The Reynolds number of a flow describes the correlation between inertia forces (in regards to convective effects) and viscous forces. It was empirically proved that below certain critical Reynolds number Re_{crit} the fluid flows smoothly and its adjacent layers past each other in an orderly way. If the boundary conditions (bc) are constant (i.e. there are no changes in time) the flow is steady. This kind of a fluid flow is named laminar. On the other side, if the values of the Reynolds number surpass the Re_{crit} value, multiple complex events are observed influencing the flow character, eventually resulting in a significant change of flow regime. As the flow is becoming more and more developed, the flow state becomes chaotic and random. Even though constant boundary conditions were imposed, the motion of fluid particles becomes unsteady. The fluid particle's velocity and flow properties change randomly and chaotically. This type of regime is named turbulent flow. The randomness of the turbulent flow prevent the calculations from thorough description of all the fluid particles motion. Thus, often the velocity fluctuations can be averaged to a steady mean value U, as marked on Figure 3.6 [33].

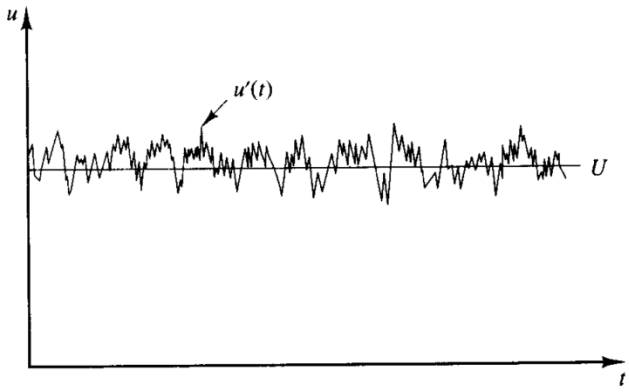

Figure 3.6 Usual point velocity measurement in turbulent flow [25]

Instead, the fluctuating component $u'(t)$ is superimposed on U, such that $u(t) = U + u'(t)$. Usually, the turbulent flow properties are described by the mean values (for instance U, V, W, P)and statistical fluctuations (respectively u', v', w', p'). It is worth noting that even in flows where the pressures and the mean velocities differ in one or two dimensions, the turbulence affects the flow properties in three-dimensions. Moreover, the observations of turbulence showed rotational flow structures, called eddies, that vary significantly in length scales [25, 31].

The particles of fluid, that are separated by a certain distance from one another at the beginning, can be brought together by means of turbulence and generation of eddies. It is so-called effective mixing, that increase the diffusion coefficients and significantly improve transport of mass, momentum and heat throughout the turbulent fluid flow regions. Accordingly with the law of conservation of energy, the eddies extract energy from the mean flow. This process is called vortex stretching. The mean velocity gradients in sheared flows decrease the rotational character of turbulent eddies [25, 32]. Respectively, the likewise aligned eddies are being stretched due to given angular velocity of the fluid particles – the further the fluid particle is located from the center of the eddy the faster it is forced to move [25].

The larger eddies have the characteristic velocity ϑ and characteristic length ℓ at the order of level near the velocity scale U and length scale L (respectively) of the mean flow [25]. Therefore, Reynolds number of the large eddy will be at similar large level. Furthermore, in the larger eddies the inertial forces are prevailing rather than viscous effects. On the other hand, smaller eddies are stretched by larger ones and to a lower degree by the mean flow. Thus, the kinetic energy is transferred from larger eddies to more and more smaller ones. This phenomena is called energy cascade. All the varying in time properties of the turbulent flow contain energy across series of wavenumbers and frequencies. The correlation between the two is that wavenumber is equal to $2\pi f/U$, where f is mentioned frequency [25, 34].

Furthermore, the lowest scale of fluid motion, that takes place in turbulent regime is dependent on viscosity. The Reynolds number of the smallest eddies is equal to 1. Usually, in typical turbulent flows in engineering practice, at this mentioned scale, where the length ranges from 0.1 to 0.01 mm and the frequency is near 10 kHz, viscous effects gain more importance. Namely, the work is done on the overcoming of the viscous stresses and the energy concerning motions of eddies is being dissipated and transformed to a form of thermal internal energy. As a result, such small scale turbulent flows are often associated with increased energy losses [25, 35].

The largest eddies have strongly anisotropic structure and are highly depend on the flow because they strongly interact with the mean flow. In this case, the diffusive character of the viscosity action have a tendency to smear out anisotropy (directionality) at these significantly smaller scales [35, 36]. If the mean flow Reynolds number is high, the eddies that are the smallest are isotropic or in other words non-directional.

3.3.1 The turbulent to laminar flow transition

The transition to the turbulence regime in an early stage can be approached by looking at the stability of the laminar flows reacting to small flow disturbances. Many theoretical research works are being conducted to analyze the transition inception, so-called hydrodynamic instability. In a lot of essential cases, the transition to turbulent regime is connected to sheared flows. Linear hydrodynamic stability theory looks for the sources of conditions that amplify the flow disturbances. In an engineering fields, the one of the priorities is to pre-identify the values of Reynolds numbers $Re_{x_{,crit}} = Ux_{crit}/\nu$ at which the amplification of disturbances occur, as well as $R_{x,tr} = -Ux_{tr}/\nu$, at which the transition ends and the turbulent flow is fully developed [25, 37].

There are two different instability mechanisms concerned with the shape of the two-dimensional laminar velocity profile of the base flow. The flows with a velocity distribution that have a so-called point of inflexion, as marked on Figure 3.7 (on the left - case a)) are generally unstable in regard to infinitely small disturbances when the value of Re is sufficiently high. This type of hydrodynamic instability was initially discovered by applying inviscid assumption in the equations concerning the disturbances evolution [37, 38]. Further investigation of the theory owing to addition of the effect of viscosity did not influence the results in any significant way, thus the described type of instability is recognized as inviscid instability. The influence

of viscous effects is concerned with smearing out fluctuations and stabilizing the flow if the Reynolds numbers are low enough [39].

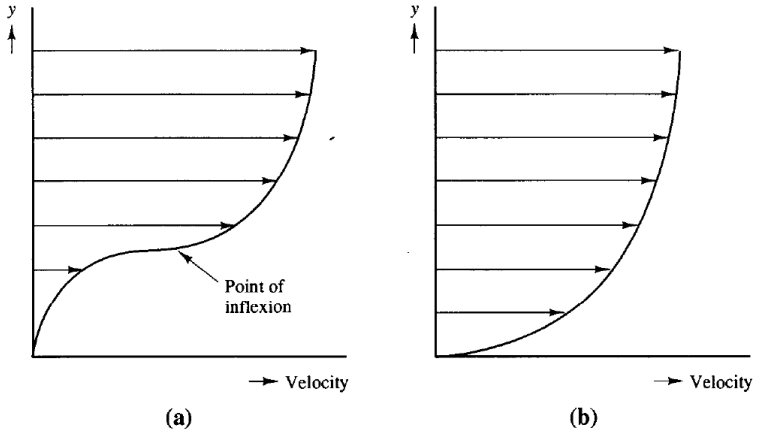

Figure 3.7 The shape of velocity profiles associated with: (a) inviscid instability; (b) viscous instability [25]

The laminar flows have velocity profiles, that do not have a point of inflexion (case (b) on a Figure 3.7) and thus, are susceptible to viscous instability [25, 40]. The approximate inviscid theory foresee non-conditional stability for mentioned velocity profiles, that are always connected with flows close to solid walls (boundary layers characterized without any negative pressure gradients). Nevertheless, the viscous effects have a more complicated aspects introducing damping in case of low and high Re values and impacting the flow in a way that cause destabilization at middle Reynolds number values [41].

In regard to transition to turbulent regime, initially the instability always emerges in the point upstream the point of transition to entirely turbulent flow [25, 41, 42]. The intensity of amplification of the unstable disturbances is dependent on the distance between the points where the Reynolds number is equal to $Re_{x,crit}$ and where the Reynolds number is equal to $Re_{x,tr}$ (the latter is so-called the point of transition) [43]. Linear theory of hydrodynamic instability tackles the problem of prediction of the point of instability and the initial point of transition. Although, there is no exhaustive theory considering these transition states. The advanced contemporary computing power of computers has enabled the simulations of the events that lead to turbulent transition [25, 44].

The transitions to a turbulent flow have some common characteristics, such as the amplification of starting small disturbances, the development of areas with concentrated rotational structures, the intense small scale motions formation, the development and interference of these areas [25]. It is worth noting that the transition process is significantly influenced by pressure gradients, disturbance levels, wall roughness and heat transfer [25, 45]. The discussion only concerns subsonic incompressible flows.

3.3.2 Time-averaged Navier-Stokes equations and the turbulence modeling

To start with, the effects of the occurrence of turbulent fluctuations on the mean flow properties will be investigated. The initial approach is to look into Reynolds equations. Firstly, the mean Φ of the flow property φ will be defined

$$\Phi = \frac{1}{\Delta t}\int_0^{\Delta t} \varphi(t)dt \tag{3.60}$$

Theoretically, the limit of time interval Δt should be approaching infinity. Nevertheless, Δt is sufficiently large, when it surpasses the time scale of the variations of property φ, that are the slowest. This mean flow property definition is appropriate in steady mean flows. If the flow is time-dependent, the mean of a given property in certain time t is an averaged value over numerous alike experiments of instant property, so-called ensemble average. The time-dependent flow property is regarded as a sum of a steady mean component Φ and time-dependent fluctuating component φ' of zero mean value (namely, $\varphi(t) = \Phi + \varphi'(t)$). Since now, the time dependence of φ nad φ' will not be written explicitly, thus $\varphi = \Phi + \varphi'$. According to the definition, the time average of the φ' fluctuations is equal to 0

$$\overline{\varphi'} = \frac{1}{\Delta t}\int_0^{\Delta t} \varphi'(t)dt = 0 \tag{3.61}$$

Furthermore, the root-mean-square (so-called rms) of the fluctuations provides information the fluctuating part

$$\varphi_{rms} = \sqrt{\overline{(\varphi')^2}} = \left[\frac{1}{\Delta t}\int_0^{\Delta t}(\varphi')^2(t)dt\right]^{\frac{1}{2}} \tag{3.62}$$

High importance of those rms values is recognized due to the possibility to measure them with a probe(for instance a hot-wire anemometer), which is sensitive to the fluctuations in turbulent regime. The kinetic energy per unit mass, denoted as k, connected with the turbulence is described as

$$k = \frac{1}{2}\left(\overline{u'^2} + \overline{v'^2} + \overline{w'^2}\right) \tag{3.63}$$

There is following dependence between the turbulence intensity T_i and a reference mean flow velocity U_{ref}

$$T_i = \frac{\left(\frac{2}{3}k\right)^{\frac{1}{2}}}{U_{ref}} \tag{3.64}$$

The rules governing the time averages of fluctuating properties $\varphi = \Phi + \varphi'$ and $\psi = \Psi + \psi'$, as well as their combinations, derivatives and integrals has to be summed before the derivation of the mean flow equations will follow.

$$\overline{\varphi'} = \overline{\psi'} = 0;\ \ \overline{\Phi} = \Phi;\ \ \overline{\frac{\partial \backslash \varphi}{\partial s}} = \frac{\overline{\partial \Phi}}{\partial s};\ \overline{\int \varphi ds} = \int \varphi ds;\ \ \overline{\varphi + \psi} = \Phi + \Psi;\ \ \overline{\varphi\psi} = \Phi\Psi + \overline{\varphi'\psi'};$$

$$\overline{\varphi\Psi} = \Phi\Psi;\ \ \overline{\varphi'\Psi} = 0 \tag{3.65}$$

The correlations above can be easily checked by taking under consideration equations 3.60 and 3.61. Subsequently, the rules listed above can be written as fluctuating vector quantities $\boldsymbol{a} = \boldsymbol{A} + \boldsymbol{a}'$ and the combinations of the above, using fluctuating scalar $\varphi = \Phi + \varphi'$

$$\overline{div\ \boldsymbol{a}} = div\ \boldsymbol{A}; \overline{div(\varphi\boldsymbol{a})} = div\ \overline{(\varphi\boldsymbol{a})} = div\ (\Phi\boldsymbol{A}) + div\ (\overline{\varphi'\boldsymbol{a}'});\ \ \overline{div\ grad\ \varphi} = div\ grad\ \Phi \tag{3.66}$$

To demonstrate the impact of turbulent fluctuations on the mean flow, the instant continuity and Navier-Stokes equations for an incompressible flow of fluid with constant viscosity will be regarded. Therefore:

$$div\ \boldsymbol{u} = 0 \tag{3.67}$$

$$\frac{\partial u}{\partial t} + div\ (u\boldsymbol{u}) = -\frac{1}{\rho}\frac{\partial p}{\partial x} + \nu\ div\ grad\ u \tag{3.68}$$

$$\frac{\partial v}{\partial t} + div\ (v\boldsymbol{u}) = -\frac{1}{\rho}\frac{\partial p}{\partial y} + \nu\ div\ grad\ v \tag{3.69}$$

$$\frac{\partial w}{\partial t} + div\ (w\boldsymbol{u}) = -\frac{1}{\rho}\frac{\partial p}{\partial z} + \nu\ div\ grad\ w \tag{3.70}$$

To be able to examine the impact of fluctuations, the flow variables $\boldsymbol{u}$ (as well as u, v, w) and p are in equations above are substituted by the sum of mean and fluctuating term as stated below.

$$\boldsymbol{u} = \boldsymbol{U} + \boldsymbol{u}';\ \ u = U + u';\ \ v = V + v', w = W + w';\ \ p = P + p'$$

Subsequently, the rules in equations 3.66 are applied, the time averages of the individual terms rewritten and the process repeated on x-, y- and z-momentum equations, resulting in

$(\boldsymbol{I})\quad (\boldsymbol{II})\qquad (\boldsymbol{III})\qquad (\boldsymbol{IV})\qquad (\boldsymbol{V})$

$$\frac{\partial U}{\partial t} + div\ (U\boldsymbol{U}) + div(\overline{u'\boldsymbol{u}'}) = -\frac{1}{\rho}\frac{\partial P}{\partial y} + \ \nu\ div\ grad\ U \tag{3.71}$$

$$\frac{\partial V}{\partial t} + div\ (V\boldsymbol{U}) + div(\overline{v'\boldsymbol{u}'}) = -\frac{1}{\rho}\frac{\partial P}{\partial y} + \ \nu\ div\ grad\ V \tag{3.72}$$

$$\frac{\partial W}{\partial t} + div\ (W\boldsymbol{U}) + div(\overline{w'\boldsymbol{u}'}) = -\frac{1}{\rho}\frac{\partial P}{\partial z} + \ \nu\ div\ grad\ W \tag{3.73}$$

Thus, the additional term (III) has appeared (there other four have already existed in equations 3.68, 3.69 and 3.79)and it is somewhat convective momentum transfer resulting from velocity fluctuations. The equations above can be rewritten placing the terms (III) on the far right hand sides in more developed forms, resulting in a set of equations, called Reynolds equations

$$\frac{\partial U}{\partial t} + div\ (U\boldsymbol{U}) = -\frac{1}{\rho}\frac{\partial P}{\partial y} + \ \nu\ div\ grad\ U + \left[-\frac{\partial\overline{u'^2}}{\partial x} - \frac{\partial\overline{u'v'}}{\partial y} - \frac{\partial\overline{u'w'}}{\partial z}\right] \tag{3.74}$$

$$\frac{\partial V}{\partial t} + div\,(V\boldsymbol{U}) = -\frac{1}{\rho}\frac{\partial P}{\partial y} + \nu\, div\, grad\, V + \left[-\frac{\partial \overline{u'v'}}{\partial x} - \frac{\partial \overline{v'^2}}{\partial y} - \frac{\partial \overline{v'w'}}{\partial z}\right] \tag{3.75}$$

$$\frac{\partial W}{\partial t} + div\,(W\boldsymbol{U}) = -\frac{1}{\rho}\frac{\partial P}{\partial z} + \nu\, div\, grad\, W + \left[-\frac{\partial \overline{u'v'}}{\partial x} - \frac{\partial \overline{v'w'}}{\partial y} - \frac{\partial \overline{w'^2}}{\partial z}\right] \tag{3.76}$$

It is necessary to write out stress terms resulting from six additional stresses and three normal stresses, as well as another three shear stresses

$$\tau_{xx} = -\rho\overline{u'^2};\ \ \tau_{yy} = -\rho\overline{v'^2};\ \ \tau_{zz} = -\rho\overline{w'^2};\tau_{xy} = \tau_{yx} = -\rho\overline{u'v'};\ \ \tau_{xz} = \tau_{zx} = -\rho\overline{u'w'};\ \ \tau_{yz} = \tau_{zy} = -\rho\overline{v'w'}$$

These turbulent stresses are so-called Reynolds stresses. The first three are normal stresses, the next six stresses are the shear stresses (representing the action between different velocity components). It is worth knowing, that if one of two velocity components were independent fluctuations, their time average would be equal to zero. On the other hand, these turbulent shear stresses are non-zero and generally much larger in comparison to the viscous stresses in turbulent regime.

Similarly, when considering an arbitrary scalar quantity and derive its transport equation we obtain some additional turbulent transport terms, namely the time average transport equation for scalar φ.

$$\frac{\partial \Phi}{\partial \mathrm{t}} + div\,(\Phi U) = div\,(\Gamma_\Phi^*\, grad\,\Phi) + \left[-\frac{\partial \overline{u'\varphi'}}{\partial x} - \frac{\partial \overline{v'\varphi'}}{\partial y} - \frac{\partial \overline{w'\varphi'}}{\partial z}\right] + S_\Phi \tag{3.77}$$

In the numerical flue gas flow analysis of the FGD installation, that is the main subject of the Thesis, the density has been assumed to be constant, but in real cases of the fluid flow the mean density could differ and the instantaneous density always shows turbulent fluctuations. Such case would have to involve modeling a compressible fluid flow. However, smaller scale density fluctuations seem not to influence the flow in a significant way [36-40]. Hence, to simplify, the flue gas in the analyzed case has been assumed incompressible.

3.3.3 Standard and realizable k-ε turbulence models overview

A turbulence model is a computational method to solve the system of mean flow equations (listed in table 3.3) by closing it in order to resolve different kind of flow problems. Generally, the majority of engineering problems only require information about the impact of the turbulence on the mean flow and prevailingly the details concerning turbulent fluctuations are redundant. To put things more precisely, the expressions regarding Reynolds stresses and turbulent scalar transport terms are often sought. In order for turbulence model to be commonly applicable it has to be accurate, simple, optimized (economical to compute) and properly characterized so it can be applied in variety of analyzed problems [41]. The turbulence model, that has been applied in the numerical flue gas flow analysis in wet limestone FGD installation is realizable k-ε, which has more developed form of one of the classical models (i.e. standard k-ε model). Therefore, in this paper only mentioned model will be described, as well as two-equation k-ε model.

The classical models are based on the Reynolds equations and constitute basis of turbulence computations in commercial CFD codes. The base of k-ε model is an assumption about presence of an analogy between the action of viscous stresses and Reynolds stresses on the mean flow. In both cases, the viscous stresses and Reynold stresses are placed on the right side of the momentum equation and in Newton's law of viscosity the viscous stresses are regarded as proportional to the rate of deformation of fluid elements [25, 41-43]. In case of incompressible fluids

$$\tau_{ij} = \mu e_{ij} = \mu \left(\frac{\partial u_i}{\partial x_j} + \frac{\partial u_j}{\partial x_i} \right) \tag{3.78}$$

Where i and $j = 1$ correspond to x-direction, $i, j = 2$ to the y-direction, and analogically $i, j = 3$ to the z-direction. The notation change is for the simplicity sake. It has been empirically recognized that the turbulence decay occurs provided that there is no shear in incompressible isothermal flows [44, 45]. Moreover, it has been observed that if the mean rate of deformation increases, the turbulent stresses also increase [44-47]. According to Boussinesq (1877), the Reynolds stresses can be correlated with the mean rate of deformation [25]

$$\tau_{ij} = -\rho \overline{u_i' u_j'} = u_t \left(\frac{\partial U_i}{\partial x_j} + \frac{\partial U_j}{\partial x_i} \right) \tag{3.79}$$

Where u_t $[Pa\ s]$ is turbulent viscosity. The kinematic turbulent viscosity is denoted as $v_t = \mu_t / \rho$ $[m^2/s]$. Analogically, transport of heat, mass and various scalar properties concerned with turbulence are modelled. The equation above shows the turbulent momentum transport to be proportional to mean gradients of velocity. Similarly, transport of scalar property due to turbulence is assumed to be proportional to the gradient of the mean value of the transported quantity, as showed below

$$-\rho \overline{u_i' \varphi'} = \Gamma_t \frac{\partial \Phi}{\partial x_i} \tag{3.80}$$

In the equation above symbol Γ_t denotes the turbulent diffusivity. Due to the fact that the transport of the momentum and heat or mass is concerned with the same phenomena (i.e. eddy mixing), the value of Γ_t can be predicted as being relatively close to the value of turbulent viscosity μ_t. A turbulent Prandtl number is being introduced, describing turbulent viscosity to turbulent diffusivity ratio

$$\sigma_t = \frac{\mu_t}{\Gamma_t} \tag{3.81}$$

Empirical data obtained from observations of many flows have shown that above ratio is usually near constant. A lot of CFD methods presume the above statement and applies the Prandtl number equal to about one. Standard k-epsilon turbulence model allows the description of turbulence, that enables the impacts of turbulence properties transport on the mean flow, diffusion and turbulence generation and decay. In k-epsilon model two partial differential transport equations are solved, notably for the turbulent kinetic energy k, as well as for the rate of dissipation of turbulent kinetic energy ε. It is worth noting that for both

models the assumption that turbulent viscosity μ_t is isotropic (i.e. the ratio between Reynolds stresses and mean rate of deformation is identical in every direction) has been made. The mentioned assumption cannot be regarded as true in every case though. Such approach could lead to inadequate flow predictions in many cases [48].

3.3.4 The standard k-epsilon model

In case of 2D thin shear layers, the slow character of the flow direction change allows the turbulence to readjust itself depending on the local parameters and conditions. If the diffusion and convection of the turbulence properties are negligible, the impact of turbulence on the mean flow can be modeled by means of the mixing length. However, in circumstances, where the diffusion and convection of turbulence properties are impactful (for example, recirculating flows) the mentioned model no longer can be applied. To face the problem, the k-epsilon model tackles it by delving into mechanisms connected with the dynamics of turbulence, namely the turbulent kinetic energy k. To start with, the definition of instantaneous kinetic energy (denoted$k(t)$) has to be defined as a sum the mean kinetic energy K, and the turbulent kinetic energy.

$$k(t) = K + k \tag{3.82}$$

$$K = \frac{1}{2}(U^2 + V^2 + W^2) \tag{3.83}$$

$$k = \frac{1}{2}\left(\overline{u'^2} + \overline{v'^2} + \overline{w'^2}\right) \tag{3.84}$$

Subsequently, the rate of deformation is being introduced is matrix form

$$e_{ij} = \begin{pmatrix} e_{xx} & e_{xy} & e_{xz} \\ e_{yx} & e_{yy} & e_{yz} \\ e_{zx} & e_{zy} & e_{zz} \end{pmatrix} \tag{3.85}$$

Furthermore, the turbulent stresses in tensor form are defined as

$$\tau_{ij} = \begin{pmatrix} \tau_{xx} & \tau_{xy} & \tau_{xz} \\ \tau_{yx} & \tau_{yy} & \tau_{yz} \\ \tau_{zx} & \tau_{zy} & \tau_{zz} \end{pmatrix} \tag{3.86}$$

The rate of deformation of a fluid element in a turbulent flow is written as a sum of the mean and a fluctuating component, as described below

$$e_{ij}(t) = E_{ij} + e'_{ij} \tag{3.87}$$

The equation describing the mean kinetic energy is a product of multiplication of appropriately x-, y- z-momentum Reynolds equations by U, V and W respectively. This step allows to obtain the time-averaged equation governing kinetic energy of the flow [49]

(I) (II) (III) (IV) (V) (VI) (VII)

$$\frac{\partial(\rho K)}{\partial t} + div(\rho KU) = div\left(-PU + 2\mu UE_{ij} - \rho U\overline{u_i' u_j'}\right) - 2\mu E_{ij} \cdot E_{ij} + \rho\overline{u_i' u_j'} \cdot E_{ij} \quad (3.88)$$

Subsequently, the equation governing the turbulent kinetic energy k is obtained by multiplication of instantaneous Navier-Stokes equations by u', v' and w' respectively (analogically to above equation), and the multiplication of proper Reynolds equations by the same fluctuating velocity components (analogy), as well as finally subtraction of obtained two equations [25, 49]. This process should give out following equation

(I) (II) (III) (IV) (V) (VI) (VII)

$$\frac{\partial(\rho k)}{\partial t} + div(\rho kU) = div\left(\overline{-p'\boldsymbol{u}'} + 2\mu\overline{\boldsymbol{u}\boldsymbol{e}_{ij}} - \rho\frac{1}{2}\overline{u_i' \cdot u_i' u_j'}\right) - 2\mu\overline{e'_{ij} \cdot e'_{ij}} + \rho\overline{u_i' u_j'} \cdot E_{ij} \quad (3.89)$$

Moreover, the essential term in turbulence dynamics is the dissipation of turbulent kinetic energy, defined as

$$\varepsilon = 2\nu\overline{e'_{ij} \cdot e'_{ij}} \quad (3.90)$$

The dissipation of turbulent kinetic energy ε (whose dimension is $[m^2/s^3]$) is concerned with the action (word) done by the smallest eddies on viscous stresses. It is always the basic mean flow kinetic energy destruction term (it is negative in K-equation), and its values are often close to production term (VII) in k-equation, thus it can never be negligible. In circumstances, where the Re number is high, the viscous transport term (IV) in k-equation is significantly smaller is regard to the turbulent transport term (VI) in the same equation.

In standard k-ε model there are two model equations, namely for k and ε. Those two turbulence quantities are used in order to define length scale ℓ and velocity scale ϑ, that concerns large scale turbulences.

$$\vartheta = k^{1/2} \quad (3.91)$$

$$\ell = \frac{k^{\frac{3}{2}}}{\varepsilon} \quad (3.92)$$

The usage of the variable ε, that normally describes small eddies to define large eddies is justified at high Re values [25, 46]. Analogically to mixing length model, the eddy viscosity is written as

$$\mu_t = C\rho\vartheta\ell = \rho C_\mu \frac{k^2}{\varepsilon} \quad (3.93)$$

In the equation 3.104, C_μ is a dimensionless constant. The transport equations of k and ε for standard k-epsilon model are as follows:

$$\frac{\partial(\rho k)}{\partial t} + div(\rho k\boldsymbol{U}) = div\left[\frac{\mu_t}{\sigma_k} grad\ k\right] + 2\mu_t E_{ij} \cdot E_{ij} - \rho\varepsilon \quad (3.94)$$

$$\frac{\partial(\rho\varepsilon)}{\partial t} + div(\rho\varepsilon \boldsymbol{U}) = div\left[\frac{\mu_t}{\sigma_\varepsilon} grad\ \varepsilon\right] + C_{1\varepsilon}\frac{\varepsilon}{k}\ 2\mu_t E_{ij}\cdot E_{ij} - C_{2\varepsilon}\rho\frac{\varepsilon^2}{k} \tag{3.95}$$

In the two above equations there are five different constants, whose values in the standard k-epsilon model are

$$C_\mu = 0.09;\ \ \sigma_k = 1;\ \ \sigma_\varepsilon = 1.3;\ \ C_{1\varepsilon} = 1.44;\ \ C_{2\varepsilon} = 1.92$$

In order to calculate the Reynolds stresses the following relationship is used

$$-\rho\overline{u_i' u_j'} = \mu_t\left(\frac{\partial U_i}{\partial x_j} + \frac{\partial U_j}{\partial x_i}\right) - \frac{2}{3}\ \rho k\delta_{ij} = 2\mu_t E_{ij} - \frac{2}{3}\rho k\delta_{ij} \tag{3.96}$$

The above equation is so-called extended Boussinesq relationship. The Kronecker delta δ_{ij} is equal to one if $i = j$ and equal to zero if $i \neq j$. Since the k and ε equations are elliptic, there is necessity to specify following boundary conditions:

Table 3.3 The boundary conditions required for k and ε equations in standard k-epsilon model [25]

Inlet	Distributions of k and ε has to be determined
Outlet or symmetry axis	$\partial k/\partial n = 0$ and $\partial\varepsilon/\partial n = 0$
Free stream	$k = 0$ and $\varepsilon = 0$
Solid walls	Highly dependent on Re

If there is no information concerning measured values of k and ε, the approximations can be introduced for inlet distributions of internal fluid flows based on turbulence intensity T_i and a characteristic length L (for instance hydraulic diameter) as follows

$$k = \frac{3}{2}\left(U_{ref}T_i\right)^2;\quad \varepsilon = C_\mu^{\frac{3}{4}}\frac{k^{\frac{3}{2}}}{\ell};\quad \ell = 0.07L$$

The flows at high Re this model does not integrate the equations up to the wall, but instead uses the universal behavior of near wall flows. Assuming y (distance from the wall) as co-ordinate direction, that is normal to a solid wall, the mean velocity at a point y_p fulfils the log-law and is contained in range $30 < y_p^+ < 500$, as well as the predictions (most preferred would me measurements) of turbulent kinetic energy values implies that the rate of turbulence production is equal to the rate of dissipation, and finally adding the eddy viscosity correlations, the following wall function is developed

$$u^+ = \frac{U}{u_t} = \frac{1}{\kappa}\ln\left(Ey_p^+\right);\ \ \varepsilon = \frac{u^3}{\kappa y};\ \ k = \frac{u_t^2}{\sqrt{C_\mu}} \tag{3.97}$$

Where E is wall roughness parameter equal to 9.8 in case of smooth walls.

If the flows is at low Re the log-law is no longer valid, thus other boundary conditions has to be applied. The equations for ε and k will also change. Since the thesis concerns a flow at high Reynolds number, the equations are omitted in this paper, but can be found in literature [25, 50].

The k-epsilon model is a well-established and one of the most commonly applied turbulence model. It is particularly useful in computations of different kinds of thin layer flows and those with recirculation, without the necessity to readjust the constant in every other problem. It is specially accurate in confined fluid flows, where there is significant share of transport effects due to Reynolds shear stresses. Thus, inevitably the popularity is owed to industrial applications, where the Reynolds shear stresses often prevailing in transport equations. However, it is not the best model to choose from in case of unconfined flows, since it only provides moderately accurate results. The model does not perform optimally in weak shear layers and the spreading rate of axisymmetric jets in fixed surroundings is strongly overpredicted [25]. The model constants can be adjusted to influence the rates of production of turbulent kinetic energy and the rate of dissipation though. These changes can provide satisfactory results provided that the constants are properly adjusted. Furthermore, the model struggles in case of swirling flows, as well as large, rapid and extra strains. It is due to the model not having described correlations between streamline curvatures and turbulence. Flows driven by anisotropic normal Reynolds stresses (i.e. in long and other than circular ducts) has to have adjusted the constants to requite for inadequate proportion of normal stresses in this model. The k-epsilon model also omits the body forces, since the frame of reference has a rotational character.

To summarize, the model has numerous advantages, namely: being widely validated and well established, simple, requires supply of only initial and/or boundary conditions, performs excellently in case of many industrial engineering flows. On the other hand, it uses significantly more computational resources (has two more PDEs to calculate in comparison to mixing length model), it performs poorly in some unconfined flows, flows with large extra strains, rotating flows and fully developed flows in non-circular channels [25].

3.3.5 Realizable k-ε turbulence model

The realizable k-ε is upgraded form of standard k-ε model, where the new model dissipation rate equation and a new realizable eddy viscosity formulation are applied. The equation of dissipation rate is concerned with the dynamic equation for fluctuating vorticity [51]. Moreover, the new eddy viscosity formulae provides realizability and includes the effect of mean rotation on turbulence stresses. The dynamic equation for fluctuating vorticity was modelled as

$$\frac{\partial}{\partial t}\left(\frac{\overline{\omega_\iota\omega_\iota}}{2}\right) + W\frac{\partial}{\partial y}\left(\frac{\overline{\omega_\iota\omega_\iota}}{2}\right) = -\frac{1}{2}\frac{\partial}{\partial y}\left(\overline{u_j\omega_\iota\omega_\iota}\right) + C_1\overline{\omega_k\omega_k}S - \frac{C_2\left(\overline{\omega_k\omega_k\omega_\iota\omega_\iota}\right)}{\frac{k}{\nu}+\sqrt{\overline{\omega_\iota\omega_\iota}}} \tag{3.98}$$

Where $\overline{\omega_\iota\omega_\iota}$ is mean-square vorticity function [51], the correlation between this function and $\overline{\omega_k\omega_k}$ is given by definition of a fluctuating anisotropic tensor b_{ij}^{ω}

$b_{ij}^{\omega} = \frac{\omega_i\omega_i}{\omega_k\omega_k} - \frac{1}{3}\delta_{ij}$, and (3.99)

$$\overline{\omega_\iota \omega_j u_{\iota j}} = \overline{b_{ij}^{\omega} \omega_k \omega_k u_{\iota j}} \tag{3.100}$$

The assumption was made that the vortex stretching aligns vortex lines with the strain rate. Additionally, it was presumed that the anisotropy b_{ij}^{ω} is caused by the anisotropy of the fluctuating strain rate. Therefore, b_{ij}^{ω} is could be assumed as being proportional to the strain rate s_{ij} (i.e. $b_{ij}^{\omega} \propto s_{ij}/s$), where $s = \left(2s_{ij}s_{ij}\right)^{\frac{1}{2}}$ and $s_{ij} = (u_{ij} + u_{ji})/2$. Although there were a few other assumptions made to arrive at the dynamic equation for fluctuating vorticity, all of them will not be presented in the thesis, since there is not enough space foresaw to delve more deeply into the origins of this particular turbulence model. The more precise and detailed description of the model is available in literature [51, 52, 53, 54].The dissipation rate equation at high Re values is obtained from following correlation:

$\varepsilon = v\,\overline{\omega_\iota \omega_\iota}$, therefore: (3.101)

$$\frac{\partial \varepsilon}{\partial t} + U_j \frac{\partial \varepsilon}{\partial j} = -\frac{\partial}{\partial j}\left(\overline{u_j \varepsilon'}\right) + C_1 S\varepsilon - C_2 \frac{\varepsilon^2}{k+\sqrt{v\varepsilon}} \tag{3.102}$$

The following suffix notation has been used: the letter i or j relate to respective coordinates and/or a fluid property/parameter in regards to these coordinates. The model coefficients are presented in the Table 3.4. The mean strain is denoted as η.

Table 3.4 The coefficients of the realizable k-ε turbulence model [51- 53]

σ_k	σ_ε	C_1	C_2	C_μ	A_0
1.0	1.2	$\max\left\{0.43, \frac{\eta}{5+\eta}\right\}$	1.9	$\frac{1}{A_0 + A_s U^* \frac{k}{\varepsilon}}$	4.0

Furthermore, the non-realizability of standard model in case of large mean strain rates (e.g. $Sk/\varepsilon > 3.7$ and $S = \sqrt{2S_{ij}S_{ij}}$), when the normal stresses would become negative and violate the Schwarz' inequity for shear stresses, in realizable k-ε model was solved by relating the C_μ coefficient to the mean strain rate (instead of being constant) [51, 52, 53].

$$U^* = \sqrt{S_{ij}S_{ij} + \overline{\Omega_{\text{ıj}}\Omega_{\text{ıj}}}}, \text{ where } \overline{\Omega_{\text{ıj}}} = \Omega_{ij} - 2\epsilon_{ijk}\omega_k \text{and } \Omega_{ij} = \overline{\Omega_{\text{ıj}}} - \epsilon_{ijk}\omega_k \tag{3.103}$$

$\overline{\Omega_{\text{ıj}}}$ is mean rotation rate viewed in a rotating reference frame having angular velocity ω_k [51]. Subsequently, the parameter A_s is calculated as

$$A_s = \sqrt{6}\cos\left(\frac{1}{3} arccos\left(\sqrt{6}\frac{S_{ij}S_{jk}S_{ki}}{(S_{ij}S_{ij})^{\frac{3}{2}}}\right)\right) \tag{3.104}$$

To summarize, in practically every measure of comparison the realizable k-ε model has demonstrated its superiority and ability to reflect the mean flows of the complex structures when placed in juxtaposition with standard k-ε model. The realizable k-ε turbulence model provides better predictions for flows concerned with spreading rate of planar and round jets. It performs excellently with flows including rotation, accurately solves boundary layers subject to adverse pressure gradients, flows with separation, as well as recirculation. Additionally, the dissipation rate equation of realizable k-ε model, has demonstrated enhanced numerical stability in computations involving advanced closure schemes (for instance second order) [51-54].

4. Research problem description

In a Combined heat and power plant after implementation of Wet Flue Gas Desulphurization Installation (wet limestone FGD) flue gases ducts configuration has changed. Before the changes boilers K1, K2 and K3 has been connected to the same chimney. Currently, the flue gases are directed through wet FGD collector. Downstream the collector, secondary Induced Draft fans (ID fans), that are responsible for maintaining appropriate sub-pressure in the ducts and collector. Presently, irregular flue gas flow has been observed in individual flue gas ducts downstream the primary induced draft fans of units K1 and K2. Additionally, the data analysis obtained from warranty measurement readings for units K1, K2 and K3 has indicated overpressure occurrence on the outlets of primary induced draft fans for every working conditions configurations, for which the measurements were conducted. Resulting pressure drop influences proper operational conditions of the installation, decreasing overall performance. The vibration measurements of the ducts has further indicated increased values of vibrations levels that could lead to damaging the flue gas ducts and the installation. The high vibration level readings could be related to elevated static pressure of flue gas stream throughout the system.

Thus, the thesis tackles the problem by developing a numerical model, which allows to investigate the issue source by imitating the real conditions of the wet FGD collector and in wide spectrum of operational configurations for the units K1, K2, K3. The flue gas flow analysis provides static pressure and stream velocity distribution throughout the wet FGD installation to evaluate existing design and operational parameters of the installation. The flue gas flow analysis is developed by applying Computational Fluid Dynamics using ANSYS Fluent software. The model geometry has been made based on post-completion documentation of the wet limestone FGD installation. To determine pressure levels and mass flow rates on the outlets from primary induced draft fans of units K1, K2 and K3, data from different owner-internal sources has been analyzed, such as reports, warranty measurements of induced draft fans of units K1, K2 and K3, as well as other historical records gathered throughout the installation lifespan up to August 2017. These documents are classified and thus cannot be listed in the literature.

4.1 Facility characterization – flue gas treatment system description in CHP plant

The CHP plant has capacity of generating approximately 260$MW_e$of electrical power and 810$MW_t$of thermal power. The combined heat and power plant has three steam boilers and two hot water boilers. The latter two work only a few days per year therefore flue gas ducts of the hot water boilers are omitted in the numerical flue gas analysis. The flue gas desulphurization method applied in investigated CHP plant is wet limestone FGD. The power plant generates nominally 1 115 000 m_n/h of flue gases. The Sulphur content in the fuel (bituminous coal) ranges from approximately 0.45% to 1.2%. The wet limestone FGD installation has about 94% SO_2 removal efficiency. The end-product of the desulphurization is gypsum. Figure 4.1 shows present configuration of the ducts (including ducts of hot water boilers) and collector, as well the previous flue gas ducts configuration featuring chimney, to where the flue gases were directed before the wet FGD system has been built. Presently, the flue gases from steam boilers (units K1, K2 and K3) are directed through the collector to the absorber. To ensure balanced draft in the boiler and avoid pressurization primary ID fans forces the flue gases to flow towards the collector. Each of the unit has two primary ID fans. Unit K1 has 0WS1 and 0WS2 primary ID fans, K2 has 1WS1 and 2WS2, consequently unit K3 has 2WS1 and 2WS2 primary ID fans.

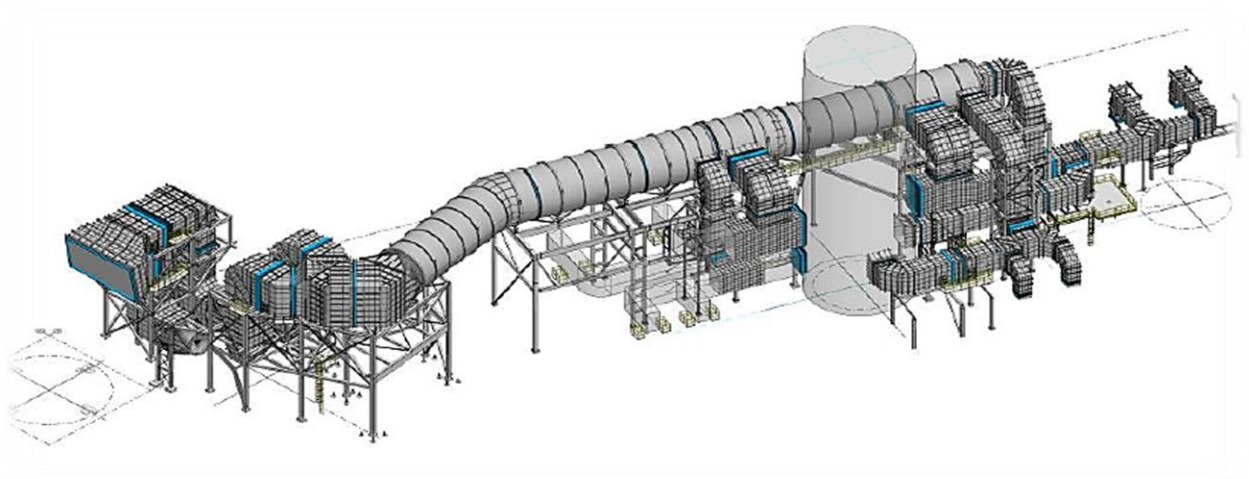

Figure 4.1 Ducts and collector configuration of examined Wet FGD installation

Downstream the collector, main (or secondary) ID fans, that are responsible for maintaining appropriate negative pressure in the ducts and collector. Slight negative pressure in the ducts is necessary for safe operation to prevent pressurization of the boiler, flue gas collector and corresponding ducts. There are two main ID fans, labeled WWS1 and WWS2. Downstream the secondary ID fans flue gas stream inlets the absorber. Figure 4.2 reflects operational idea of wet limestone FGD system, indicating the locations of primary and secondary ID fans and showing simplified flue gas flow diagram, as well as control system responsible for managing main ID fans, that regulate the static pressure level in the collector. The control system is designed to maintain constant fixed sub-pressure level (-350 Pa) in the measurement point. The pressure control/measurement point is installed on the collector, downstream the flue gas stream inlet from

unit K1 and upstream the inlet of flue gases coming from unit K2. The information about static pressure level is sent from the measurement point to the controller. If the static pressure level in not equal to the designed static pressure level, the controller sends the control signal to main ID fans adjusting their rotational speed. Subsequently, main ID fans generate appropriate static pressure in particular flue gas ducts and the collector such that negative pressure in measurement point is equal to nominal designed value. One of the goals of conducting the numerical flue gas flow analysis of examined wet limestone FGD installation is to determine the value of static pressure in the control point such that the flue gas ducts and the collector operates under negative pressure.

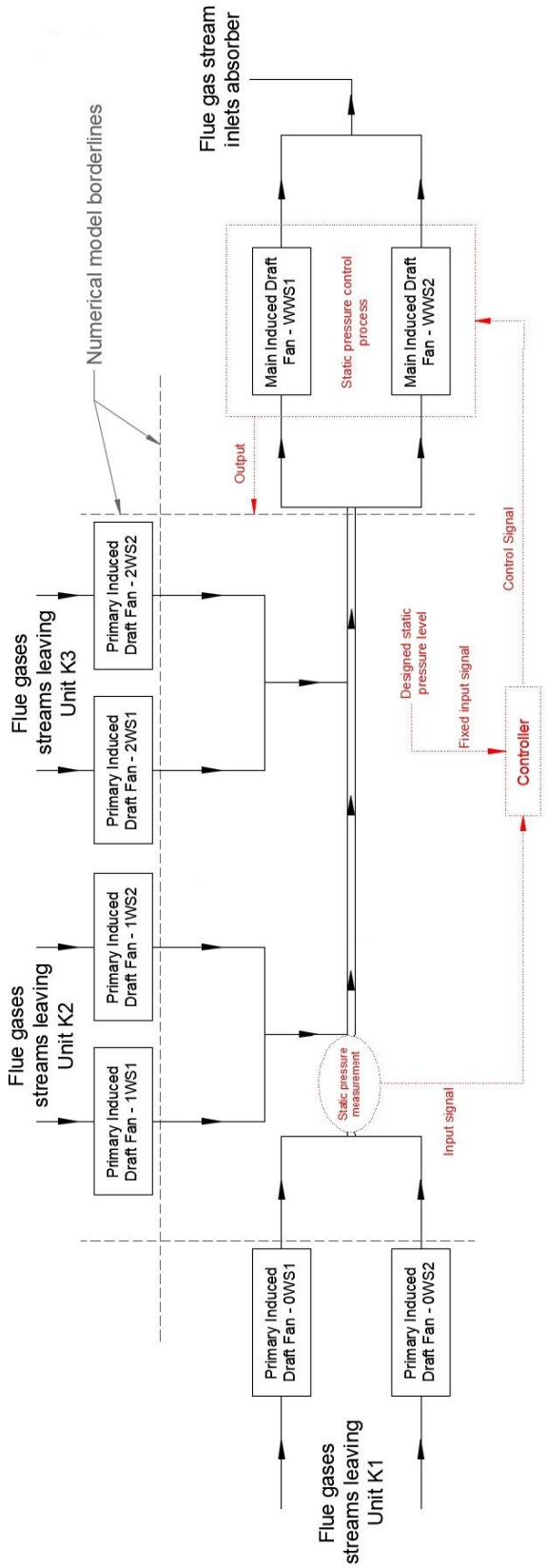

Figure 4.2 Wet FGD installation operational scheme

5. Numerical model description

The exponential growth in the computing power of computers throughout recent decades has caused prompt development of Computational Fluid Dynamics. As a result, the numerical analysis has become yet another generally recognized and accepted method to get a solution to wide range of examined industrial, engineering and scientific problems. Analytical solving could lead to obtaining an exact solution for studying the behavior of the system with various properties. The implementation of an analytical method of solving can be of limited use thought. We can solve analytically very few practical engineering and industrial problems. Since fluid motion is governed by Navier-Stokes equations, a set of coupled nonlinear partial differential equations derived from fundamental laws of conservation of mass, momentum and energy, the fluid flow velocity, pressure, density and temperature are often unknown. Thus, it is often impossible to acquire an analytical solution. In these cases, the scientists often strive to find an a solution empirically. Despite that, most commonly it is troublesome to acquire a sufficient solution. The results could not mirror the investigated problem effectively due to emerged dilemmas in enforcing dynamic and geometric similitude between laboratory experiments and designed models. In addition, it is often expensive and/or difficult due to complicated design and structure. Therefore, numerical solving is an interesting alternative to analytical and empirical approach, especially if one cannot solve problem analytically (too many unknowns) and/or empirical method is not economically and/or physically viable. The usefulness of an numerical analysis also present itself when examining operating installation since it eliminates the necessity to shut it down and/or installation of a supplementary measurement devices, that would otherwise be redundant.

The thesis tackles the problem of simulating the operation of working installation. Generally, the work intends to acquire a numerical solution (i.e. numerically obtained satisfactory approximation – not exact solution as in analytical approach) to a Navier-Stokes equations based on laws of conservation of mass and momentum. The objective is to solve the equations numerically to get static pressure and velocity distributions of flue gas throughout the ducts system which directs the stream to the absorber.

It is necessary to keep a negative pressure in the ducts and the collector of the Flue Gas Desulphurization installation as it influences proper operational conditions of the installation, and overall performance of the duct system. However the induced draft fans warranty measurements pinpointed increased (positive) pressure levels. Consequently, it was urgent to find pressure distribution and velocity of the flue gas stream flowing through the ducts to examine the existing designed ducts system and nominal work parameters of the secondary Induced Draft fans, that are maintaining adequate pressure level in investigated part of the wet limestone FGD installation ducts.

5.1 Numerical model development description

The chapter is divided into three main subchapters, notably, the 3D model geometry development, mesh development and optimization (including mesh sensitivity analysis), the subchapter about boundary conditions, as well as turbulence model choice and closure scheme applied in numerical computations. Moreover, the context and/or justification for the respective approaches in modeling process is shortly described.

5.1.1 Model's geometry

The model's geometry has been developed based on post-completion documentation of wet Flue Gas Desulphurization installation. The documentation included the two-dimensional drawings of respective parts of the duct and collector system. Thus, it was necessary to develop three-dimensional model based on the drawings provided by the company responsible for the design of the built installation. The software used in the process was ANSYS SpaceClaim. The current duct and collector system geometry model is showed on the Figure 5.1.

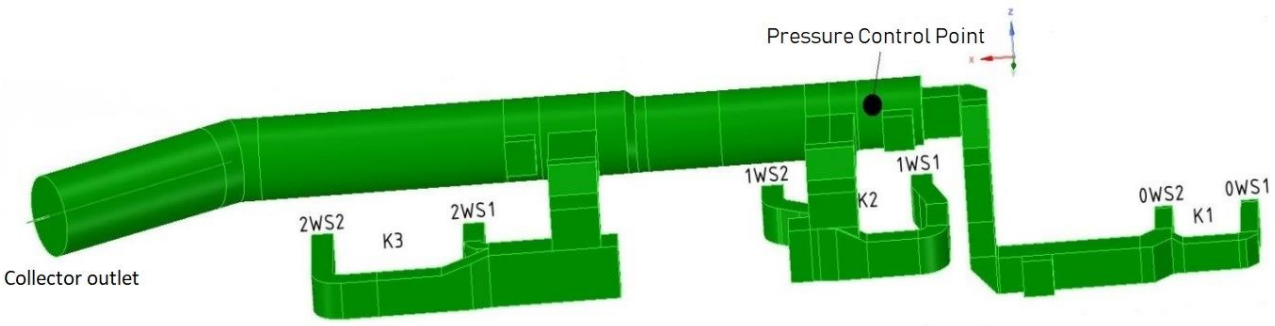

Figure 5.1 Model's geometry developed in ANSYS SpaceClaim

5.1.2 Numerical mesh development and optimization

Before simulations for each of the operational configurations had been carried out, the numerical mesh optimization has been conducted in order to minimize computation time and simultaneously maintain satisfactory results accuracy. In order to realize the optimization process, the mesh sensitivity analysis has been conducted, as well as optimization of local mesh structures and densities in places with inferior quality. The main quality criteria were skewness and orthogonal quality indicative parameters available in ANSYS Mesh software.

5.1.2.1 Mesh sensitivity analysis

The mesh sensitivity is a basic iterative process of optimization of model mesh density in order to obtain results with sufficient accuracy with simultaneous minimum number of cells (the less cells there are, the lower computation time is). The numerical model had to be solved for relatively different number of cells (various mesh densities), starting with mesh with low number of cells – in this case approximately 67k - and for subsequently increased mesh densities – here 354k, 731k and 916k consequently. The values used to

indicate the subsequent accuracy improvement accompanying consequent increased mesh densities, (so-called quantities of interests) were area averaged static pressure levels at evaluation faces placed normal to the flow direction. The locations of those faces are presented on the Figure 5.2 below.

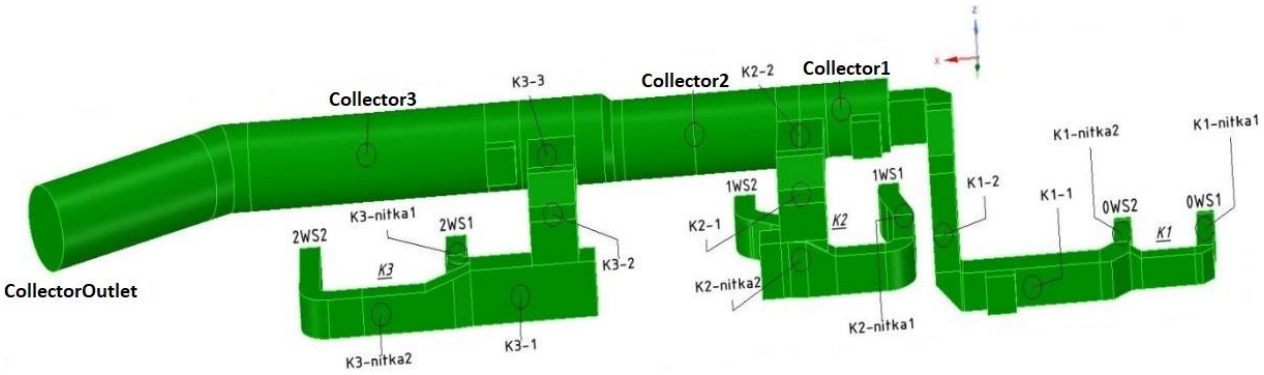

Figure 5.2 Evaluation planes used to calculate area averaged static pressure levels at marked faces normal to the flow direction

Besides mentioned mesh sensitivity analysis, the mesh quality optimization has been carried out to optimize locations with lower mesh quality indicated by ANSYS Mesh software (skewness and orthogonal quality criteria) by changing the meshing method, increasing mesh densities in impactful model areas and decreasing number of cells values in less impactful areas. The fourth iteration of mesh sensitivity study with about 713 thousands of number of cells has demonstrated overall error compared to iteration fifth with 916 thousands of number of cells at level 4.94%. The relative accuracy has been considered as sufficient, but the further optimization of mesh quality from forth iteration has been conducted anyway. This resulted in an additional numerical mesh with improved quality that counts approximately 639 thousands of number of cells and have overall relative error compared to fifth iteration mesh at level 3.72%. The calculations and indicative results juxtaposition for each mesh is presented in the Table 5.1. The mesh sensitivity analysis is depicted on Figure 5.3. The Figure 5.4 shows the final mesh structure (the third iteration in Table 5.1 and on the Figure 5.3).

The overall relative error has been calculated as a sum of the respective absolute errors concerned with area averaged static pressure levels differences between a particular iteration and fifth iteration (final one) in respect to the final iteration. To realize comparison of final numerical mesh to other analyzed meshes the following parameter is being introduced

$$h_i = \frac{1}{\sqrt[3]{N_{i,c}}} \tag{5.1}$$

Where $N_{i,c}$ is number of cells in mesh sensitivity iteration i.

Another important parameter to consider when developing a numerical mesh is expected boundary layer shape and its influence on the results. It is connected with the choice of particular turbulent model and an

appropriate wall function, as well as the proper type and sufficient mesh density of near wall regions of the model. The essential parameter is often a dimensionless wall distance y^+, which is equal several thousand for the analyzed problem. According to ASNYS Fluent Theory Guide from 2015, for very high Reynolds number values (the analyzed case has $1{,}15 \cdot 10^6 < Re < 1{,}7 \cdot 10^6$), it can reach values as high as several thousand [54]. The Reynolds number is calculated based on measured values for respective inlets and listed in the Table 5.3.

Table 5.1 Results for consecutive iterations of mesh sensitivity analysis and overall relative errors of the meshes

	Iteration i		**1**	**2**	**3***	**4**	**5**
	Number of cells		**67k**	**354k**	**639k**	**713k**	**916k**
	h_i/h_3		0,472	0,821	1,000	1,037	1,128
Surfaces – evaluation planes	0WS1	**Area Averaged Static Pressure [Pa]**	218,3	203,7	161,5	166	159,7
	0WS2		133,6	122,5	122,6	127,7	121,5
	K1-nitka1		97,7	58,14	43,54	48,02	41,82
	K1-nitka2		65,31	63,15	37,98	40,48	34,35
	K1-1		91,64	90,36	80,19	80,2	75,2
	K1-2		-34,83	-29,92	-18,63	-18,12	-22,02
	1WS1		298	348,9	261,6	285,6	272,6
	1WS2		238,6	264,3	227,4	238,2	238,6
	K2-nitka1		278,4	326,5	234,7	258,7	245,6
	K2-nitka2		169,7	206,9	185,3	196,3	195,7
	K2-1		-52,7	-60,86	-135,3	-143,5	-138
	K2-2		-297,3	-296	-295,1	-296,6	-296,4
	2WS1		68,68	53,59	67,24	67,39	64,99
	2WS2		69,59	60,57	76,84	76,98	74,65
	K3-nitka1		43,94	24,87	23,87	24,76	22,37
	K3-nitka2		66,35	57,33	73,55	73,68	71,37
	K3-1		42,05	37,06	58,81	59,42	56,92
	K3-2		-166,5	-162,3	-202	-205,8	-195,2
	K3-3		-160,1	-159,8	-163,9	-167,8	-164,6
	Collector1		-142,2	-143,2	-141,5	-143	-142,7
	Collector2		-215,2	-214,2	-213,8	-216,2	-215,8
	Collector3		-291,4	-293,3	-292,9	-295,2	-295,1
	CollectorOutlet		-299,8	-299,9	-299,9	-300	-300
	Overall relative error		26,52%	20,19%	3,72%	4,94%	0%

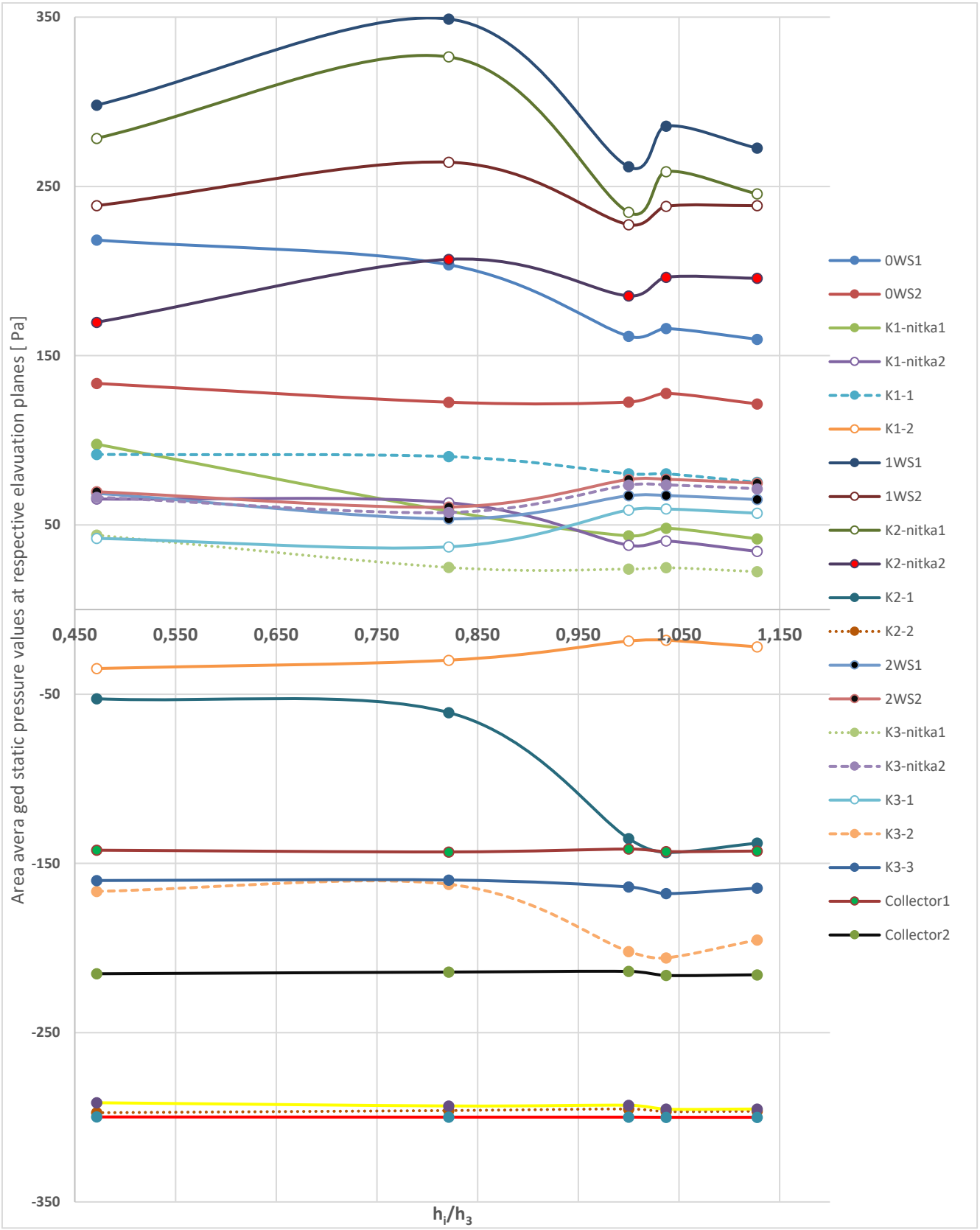

Figure 5.3 Mesh sensitivity analysis and mesh quality optimization influence on results accuracy

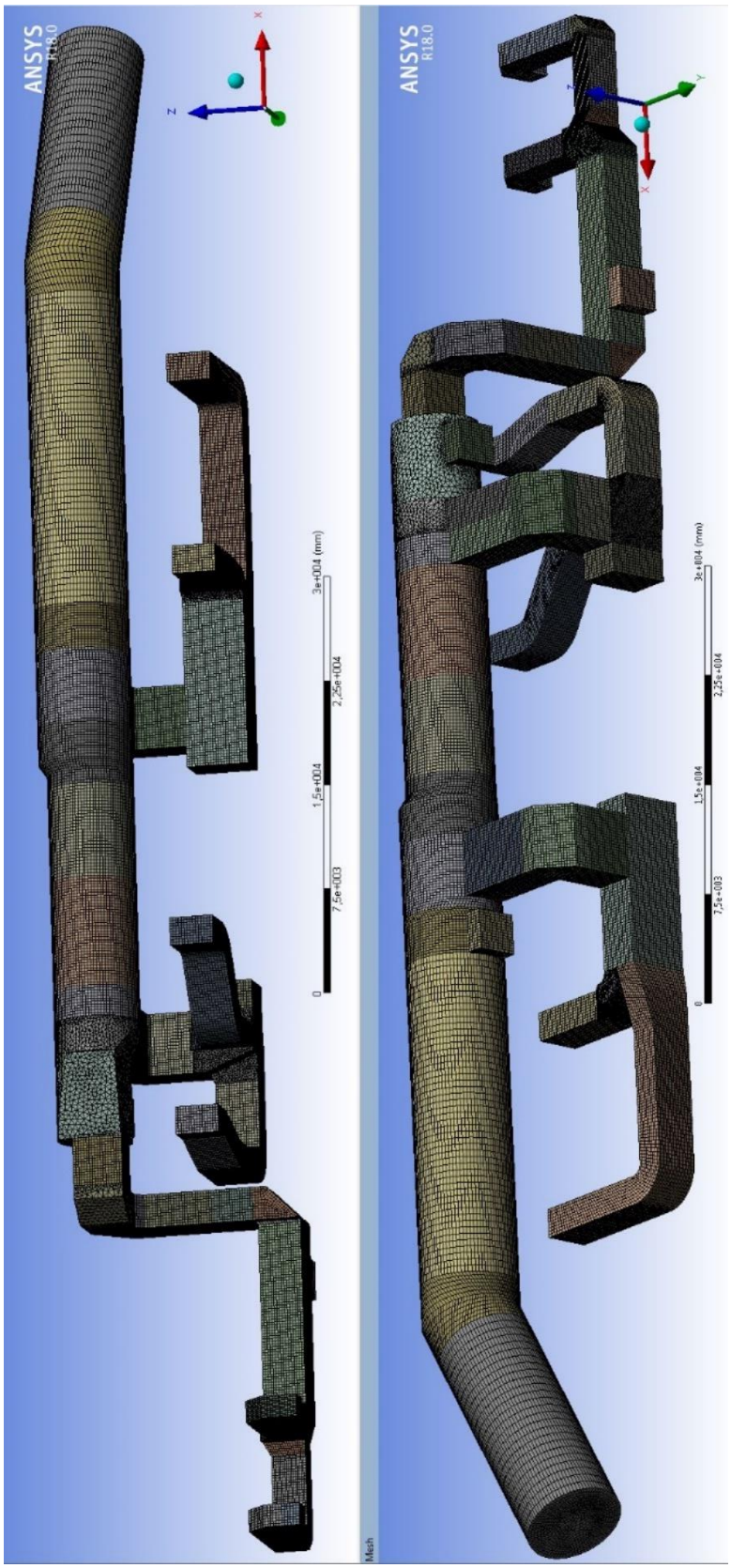

Figure 5.4 Final mesh state

5.1.3 Basic flue gas parameters

In order to determine the operational parameters of the wet FGD collector the installation owner's internal report featuring primary induced draft fan measurements installed next to the steam boiler units has been analyzed. The recorded data has allowed to determine approximate flue gas composition, density, as well as mass flow rates on the outlets from the primary ID fans of each unit for most of the steam boiler capacities configurations. In initial phase of the model development process the data regarding measured static pressure allowed to verify the correctness of the numerical model. Knowing approximate flue gas composition and the temperature, the density and dynamic viscosity has been calculated using Engineering Equation Solver software.

Table 5.2 Assumed flue gas parameters and composition (volume percentage concertation of each gas component)

Assumed flue gas composition, %					**Flue gas parameters**		
O_2	CO_2	N_2	H_2O	SO_2	Temperature, °C	Dynamic viscosity, kg//m/s	Density, kg/m^3
6.5	12.8	74.36	6,3	0,04	135	2.19E-05	0.8758

5.1.4 Boundary conditions and turbulence model

To start with, it is necessary to indicate the dimensions of ducts in places of respective inlets from primary ID fans. It is concerned with particular boundary conditions applied to improve the necessary inputs for computations and the initial inputs of the realizable k-ε turbulence model applied. It is concerned with turbulence intensity (assumed as 10% due to primary ID fans work impact on the fluid flow) and characteristic dimension (hydraulic diameter) of the respective inlet/outlet ducts. The Table 5.3 contains mentioned information and calculated hydraulic diameter, as well as other essential information to provide sufficient boundary conditions and initial values. The methodology taken is in accordance with the information concerning transport equations and turbulence modeling discussed in Chapter 3. The hydraulic diameter has been calculated as:

$$L_D = 4\frac{L_1 L_2}{2L_1+2L_2} \tag{5.2}$$

where L_1 and L_2 are respective dimensions of rectangular inlet surfaces. The Reynolds number has been computed as:

$$Re = \frac{\rho \dot{V} L_D}{L_1 L_2 \mu} \tag{5.3}$$

where $\dot{V}$ is a volumetric flow rate [m^3/s] in the respective rectangular duct with L_1 and L_2 as appropriate dimensions of the duct cross-section. This is in regard to stream of fluid with density ρ and dynamic viscosity μ.

Table 5.3 Boundary conditions applied for consecutive inlet faces and calculated Re number for appropriate inlet conditions

Unit	K1		K2		K3	
Inlet from primary ID fan	**0WS1**	**0WS2**	**1WS1**	**1WS2**	**2WS1**	**2WS2**
Inlet dimensions, m	1,6	1,72	2	3,15	2	3,15
Turbulent intensity	10%		10%		10%	
Hydraulic diameter, m	1,66		2,45		2,45	
Mass flow rate, kg/s	61,47	47,69	111,67	107,82	97,78	97,16
Reynolds number	1480867	1148774	1734284	1674491	1518566	1508937

The applied turbulence model is realizable k-ε model, discussed in more detail in Chapter 3. The standard wall function was applied. The gravitational acceleration was assumed to be equal to 9.81 m/s^2.

6. Numerical flue gas flow analysis

The Figure 6.1 represents the locations of faces normal to flow direction, where area averaged static pressure values have been calculated by means of numerical simulations.

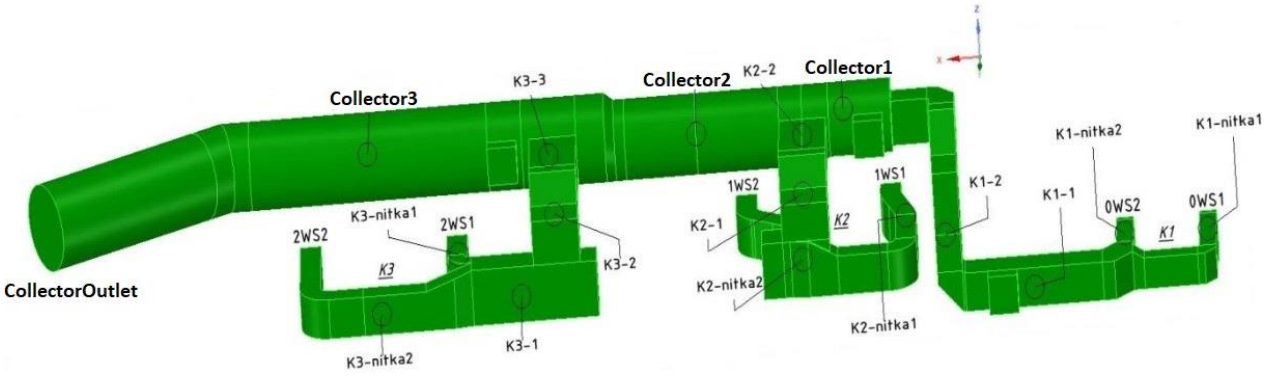

Figure 6.1 Evaluation planes for used to calculate and compare area averaged static pressure values

6.1 Operational system conditions

The Table 6.1 is a juxtaposition of different configurations of steam boiler capacities of each of unit K1, K2 and K2, for which the flue gas flow analysis has been conducted. The configurations has been labeled with subsequent alphabet letters A, B, C, D, E, F, G, H and I. The number one next to the letter informs that the configuration was conducted for the measured conditions. However, number 2 is a configuration, where the mass flow rate boundary conditions on the inlets from respective unit has been assumed as an arithmetic average from measured values, so that the impact of regular flow distribution for each of the two inlet ducts could be examined.

Table 6.1 The list of analyzed configurations and the steam boiler capacities

No.	A1	A2	B1	B2	C	D	E	F	G1	G2	H	I
Unit	**Steam boiler capacity, t/h**											
K1	230	230	230	230	230	185	185	230	140	140	140	0
K2	430	430	430	430	0	430	350	350	430	430	350	430
K3	430	430	0	0	0	430	380	380	430	430	380	0

6.2 List of analyzed operational configurations

Table 6.2 The steam boiler capacities of each unit per a configuration and applied mass flow rates as boundary conditions

Lp.	Unit	K1		K2		K3	
	Primary Induced Draft Fan	0WS1	0WS2	1WS1	1WS2	2WS1	2WS2
A	Steam Boiler Capacity t/h	230		430		430	
1	ID fan outlet temperature, °C	143,8	137,6	128,5	121,3	132,8	131,2
	Flue gas mass flow rate, kg/s	53,8	41,8	97,8	94,4	85,6	85,1
2	ID fan outlet temperature, °C	143,8	137,6	128,5	121,3	132,8	131,2
	Flue gas mass flow rate, kg/s	47,8	47,8	96,1	96,1	85,4	85,4
B	Steam Boiler Capacity t/h	230		430		0	
1	ID fan outlet temperature, °C	143,8	137,6	128,5	121,3	0,0	0,0
	Flue gas mass flow rate, kg/s	53,8	41,8	97,8	94,4	0,0	0,0
2	ID fan outlet temperature, °C	143,8	137,6	128,5	121,3	0,0	0,0
	Flue gas mass flow rate, kg/s	47,8	47,8	96,1	96,1	0,0	0,0
C	Steam Boiler Capacity t/h	230		0		0	
	ID fan outlet temperature, °C	143,8	137,6	0,0	0,0	0,0	0,0
	Flue gas mass flow rate, kg/s	47,8	47,8	0,0	0,0	0,0	0,0
D	Steam Boiler Capacity t/h	185		430		430	
	ID fan outlet temperature, °C	133,9	129,3	128,5	121,3	132,8	131,2
	Flue gas mass flow rate, kg/s	37,3	37,3	96,1	96,1	85,4	85,4
E	Steam Boiler Capacity t/h	185		350		380	
	ID fan outlet temperature, °C	133,9	129,3	120,4	126,3	122,7	122,0
	Flue gas mass flow rate, kg/s	37,3	37,3	68,7	68,7	64,3	64,3
F	Steam Boiler Capacity t/h	230		350		380	
	ID fan outlet temperature, °C	143,8	137,6	120,4	126,3	122,7	122,0
	Flue gas mass flow rate, kg/s	47,8	47,8	68,7	68,7	64,3	64,3
G	Steam Boiler Capacity t/h	140		430		430	
1	ID fan outlet temperature, °C	133,9	127,2	128,5	121,3	132,8	131,2
	Flue gas mass flow rate, kg/s	20,9	38,2	97,8	94,4	85,6	85,1
2	ID fan outlet temperature, °C	133,9	127,2	128,5	121,3	132,8	131,2
	Flue gas mass flow rate, kg/s	29,5	29,5	96,1	96,1	85,4	85,4
H	Steam Boiler Capacity t/h	140		350		380	
	ID fan outlet temperature, °C	133,9	127,2	120,4	126,3	122,7	122,0
	Flue gas mass flow rate, kg/s	29,5	29,5	68,7	68,7	64,3	64,3
I	Steam Boiler Capacity t/h	0		430		0	
	ID fan outlet temperature, °C	0,0	0,0	128,5	121,3	0,0	0,0
	Flue gas mass flow rate, kg/s	0,0	0,0	96,1	96,1	0,0	0,0

The numerical model has been designed so that the static pressure levels at Control Point and at the inlets from primary Induced Draft fans are directly influenced by changes in the values of static pressure in the outlet surface (CollectorOutlet evaluation plane – Figure 6.1). Owing to automated character of regulation system of secondary Induced Draft fans, which is based on the value of static pressure in the measurement point (Control Point), it is possible to find the static pressure level at Control Point so that in the flue gas ducts and collector a negative pressure is being maintained. The table 6.2 demonstrates the steam boiler capacities of each unit per a configuration and applied mass flow rates as boundary conditions. Not only this information is contained, but also the values of measured temperature levels on the inlets from primary Induced Draft fans. The assumed temperature of flue gases has been calculated as weighted average of the measured temperature values from the configuration A1. The respective weights are the ratios of a given mass flow rates at an inlet to a sum of all mass flow rates. The calculated temperature has been assumed as $135°C$. The flue gas composition has been assumed based on the previous records of measured composition. Knowing the temperature and composition of the flue gas, the density and dynamic viscosity has been calculated using Engineering Equation Software.

6.3 Analysis results juxtaposition

The Table 6.3 shows the results juxtaposition for each of the analyzed configuration. The results are presented for faces, that are equivalent to inlets from respective primary ID fans. The mentioned locations has always showed the largest static pressure levels, since they are placed the furthest in the model from the secondary Induced Draft fans, that's main task is to maintain negative pressure throughout the collector and flue gas ducts. Furthermore, the primary Induced Draft fans generate negative pressure upstream, but also produce an increased pressure levels downstream these fans. As a result the area averaged static pressure at those locations are the highest. Therefore, if there is a negative pressure level at those locations it is safe to assume that the throughout the rest of the flue gas ducts and collector the pressure will be smaller (i.e. there will be sub-pressure) – it would also mean that the installation works properly. The results in the Table 6.3 has indicated the positive pressure occurrence for the majority of configurations. In order to maintain sub-pressure in the collector and the ducts, it is necessary to keep the static pressure in the control point at maximum -450 Pa. To compare, previous designed nominal value was -350 Pa.

Table 6.3 Analysis results juxtaposition including calculated and measured static pressure values for each of the analyzed configuration

Analysis		K1				K2				K3				Pressure Measurement	Outlet BC
		0WS1		0WS2		1WS1		1WS2		2WS1		2WS2			
		Mass flow rate, kg/s	Static Pressure, Pa	Mass flow rate, kg/s	Static Pressure, Pa	Mass flow rate, kg/s	Static Pressure, Pa	Mass flow rate, kg/s	Static Pressure, Pa	Mass flow rate, kg/s	Static Pressure, Pa	Mass flow rate, kg/s	Static Pressure, Pa	Static Pressure, Pa	Static Pressure, Pa
A	1	**54**	171	**42**	132	**98**	294	**94**	255	**86**	35	**85**	90	-142	-300
			79		39		196		157		-60		-6	-240	-400
			-21		-61		95		57		-160		-106	-340	-500
			-122		-161		-5		-43		-260		-206	-440	-600
	2	**48**	164	**48**	132	**96**	256	**96**	220	**85**	25	**85**	78	-147	-300
			64		32		156		120		-75		-23	-247	-400
			-36		-68		56		20		-175		-123	-347	-500
			-136		-168		-44		-80		-275		-223	-447	-600
B	1	**54**	68	**42**	28	**98**	186	**94**	147	**0**	-294	**0**	-294	-250	-300
			-32		-72		86		47		-394		-394	-350	-400
			-132		-172		-14		-53		-494		-494	-450	-500
			-232		-272		-114		-153		-594		-594	-550	-600
	2	**48**	54	**48**	22	**96**	150	**96**	113	**0**	-295	**0**	-295	-254	-300
			-46		-78		50		13		-395		-395	-354	-400
			-146		-178		-51		-87		-495		-495	-454	-500
			-246		-278		-151		-187		-595		-595	-554	-600
C		**48**	-11	**48**	-43	**0**	-323	**0**	-323	**0**	-300	**0**	-300	-328	-300
			-111		-142		-423		-423		-400		-400	-428	-400
			-210		-242		-523		-523		-500		-500	-528	-500
			-311		-343		-623		-623		-600		-600	-628	-600
D		**37**	40	**37**	20	**96**	243	**96**	206	**85**	12	**85**	64	-150	-300
			-60		-80		143		106		-88		-36	-250	-400
			-160		-180		43		6		-189		-136	-350	-500
			-260		-280		-57		-94		-289		-236	-450	-600
E		**37**	-26	**37**	-45	**69**	-9	**69**	-27	**64**	-121	**64**	-91	-218	-300
			-126		-145		-109		-127		-221		-191	-318	-400
			-226		-245		-209		-227		-321		-291	-418	-500
			-326		-345		-309		-327		-421		-391	-518	-600
F		**48**	91	**48**	60	**69**	-1	**69**	-19	**64**	-104	**64**	-73	-218	-300
			-9		-40		-101		-119		-204		-174	-318	-400
			-109		-140		-201		-219		-304		-274	-418	-500
			-209		-240		-301		-319		-404		-374	-518	-600

G	1	**21**	-43 -143 -243 -343	**38**	-49 -149 -249 -349	**98**	233 133 32 -68	**94**	198 98 -2 -103	**86**	6 -94 -194 -294	**85**	60 -41 -141 -241	-156 -256 -356 -456	-300 -400 -500 -600
	2	**30**	-36 -136 -236 -336	**30**	-48 -149 -249 -349	**96**	233 133 33 -67	**96**	196 96 -4 -104	**85**	6 -94 -195 -295	**85**	59 -42 -142 -242	-154 -254 -354 -454	-300 -400 -500 -600
H		**30**	-101 -201 -301 -401	**30**	-114 -214 -314 -414	**69**	-16 -116 -216 -316	**69**	-35 -135 -235 -335	**64**	-127 -227 -327 -427	**64**	-97 -197 -297 -397	-220 -320 -420 -520	-300 -400 -500 -600
I		**0**	-269 -369 -469 -569	**0**	-269 -369 -469 -569	**96**	112 12 -88 -188	**96**	76 -24 -125 -225	**0**	-299 -399 -499 -599	**0**	-299 -399 -499 -599	-260 -360 -460 -560	-300 -400 -500 -600

6.3.1 The regulation curves

The regulation curves is a diagram that shows the area averaged static pressure levels at the inlet surfaces (the places, that demonstrate the highest static pressure levels for all steam boiler capacity configurations of each of the unit ducts) dependency on the area averaged static pressure level in control point for respective configurations. From the maintenance point of view it is extremely useful as it allows to adjust the secondary Induced Draft fans setup to produce sufficient negative pressure throughout the ducts to ensure, that the ducts and collector system work under sub-pressure (i.e. to program the secondary ID fans to maintain certain maximum value of static pressure at control point). The simulation results, that include analysis of various configurations (variants) have allowed to develop the regulation curves, that represents the dependency of the pressure level at Control Point on the area averaged static pressure levels at the inlets from respective primary induced draft fans from units K1, K2 and K3. The results imply that the previous designed value of the static pressure at control point (-250 Pa) was incorrect as it was impossible to maintain the sub-pressure at the inlets form respective primary Induced Draft fans of each unit with this assumption. The updated value of the static pressure at control point (-350) allow to maintain negative pressure throughout the respective flue gas ducts for configurations C, E, F and H. However, in order for the flue gas ducts and collector to work under negative pressure for every variant the pressure level at control point has to be kept at level -450 Pa. This value has to be treated as an absolute minimum limit. In common practice for the pressure values at the inlets from primary Induced Draft fans ranging from -50 Pa up to -150 Pa, other existing systems has demonstrated the installation to work correctly. The comparison of variants A1 and A2 has shown the impact of irregular mass flow rates at the inlets to respective ducts of each unit. In case of regular flow, at the highest - the decrease in the static pressure levels has been observed in the inlets from primary ID fans of respective unit ducts to obtain 40 Pa in comparison to irregular

flow (for the same conditions). The mentioned highest difference has been noted for ducts of unit K2. However, the differences in other locations are negligible.

According to the results, the highest values of area averaged static pressure are observed to occur for ducts of unit K2 in place, where respective flue gas ducts of unit K2 joint.

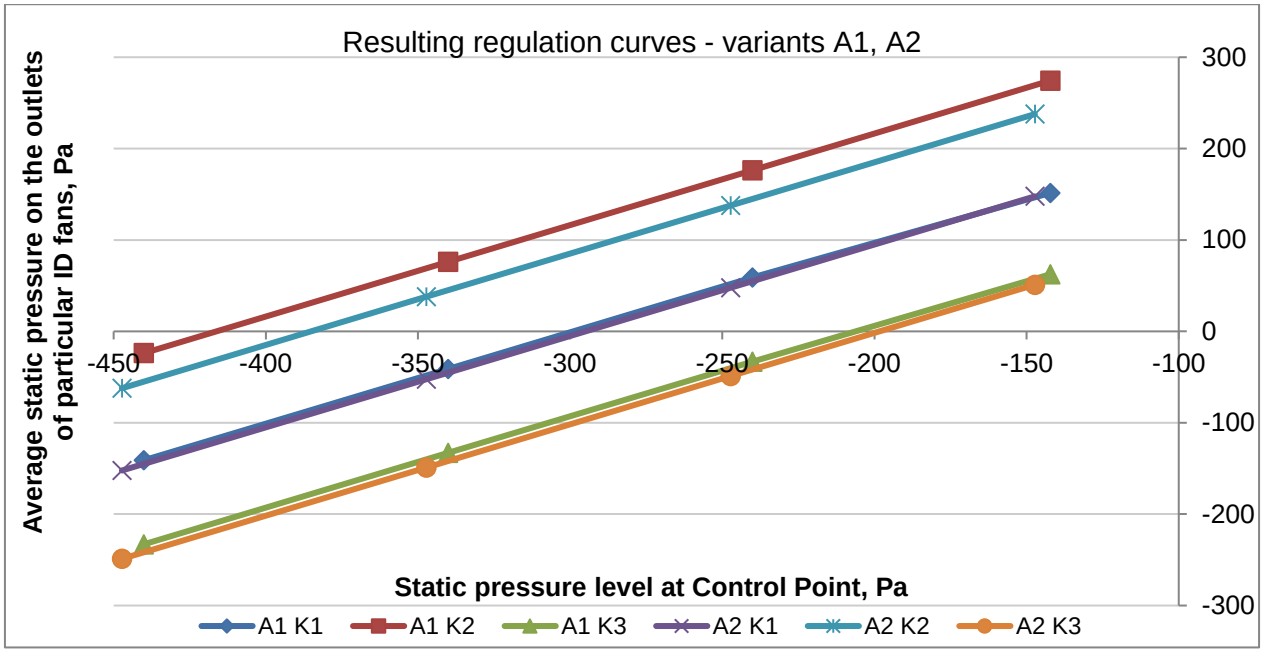

Figure 6.2 Regulation curves for A1 and A2 configurations

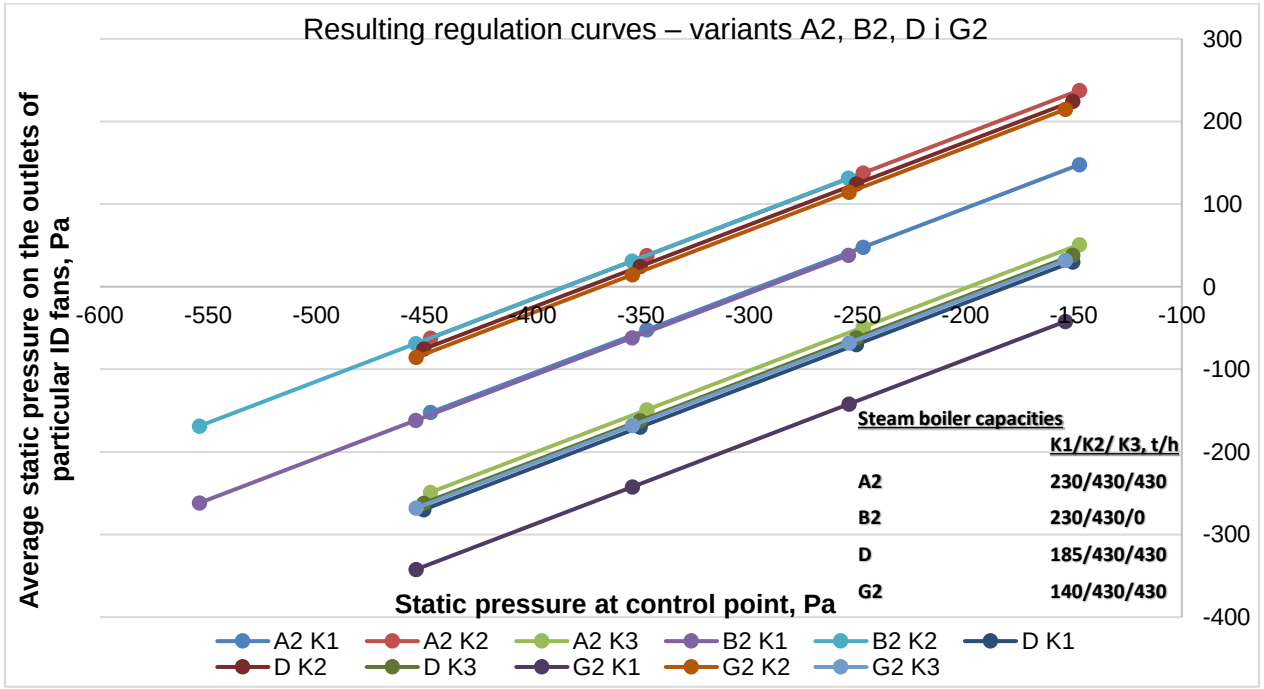

Figure 6.3 Regulation curves for A2, B2, D and G2 configurations

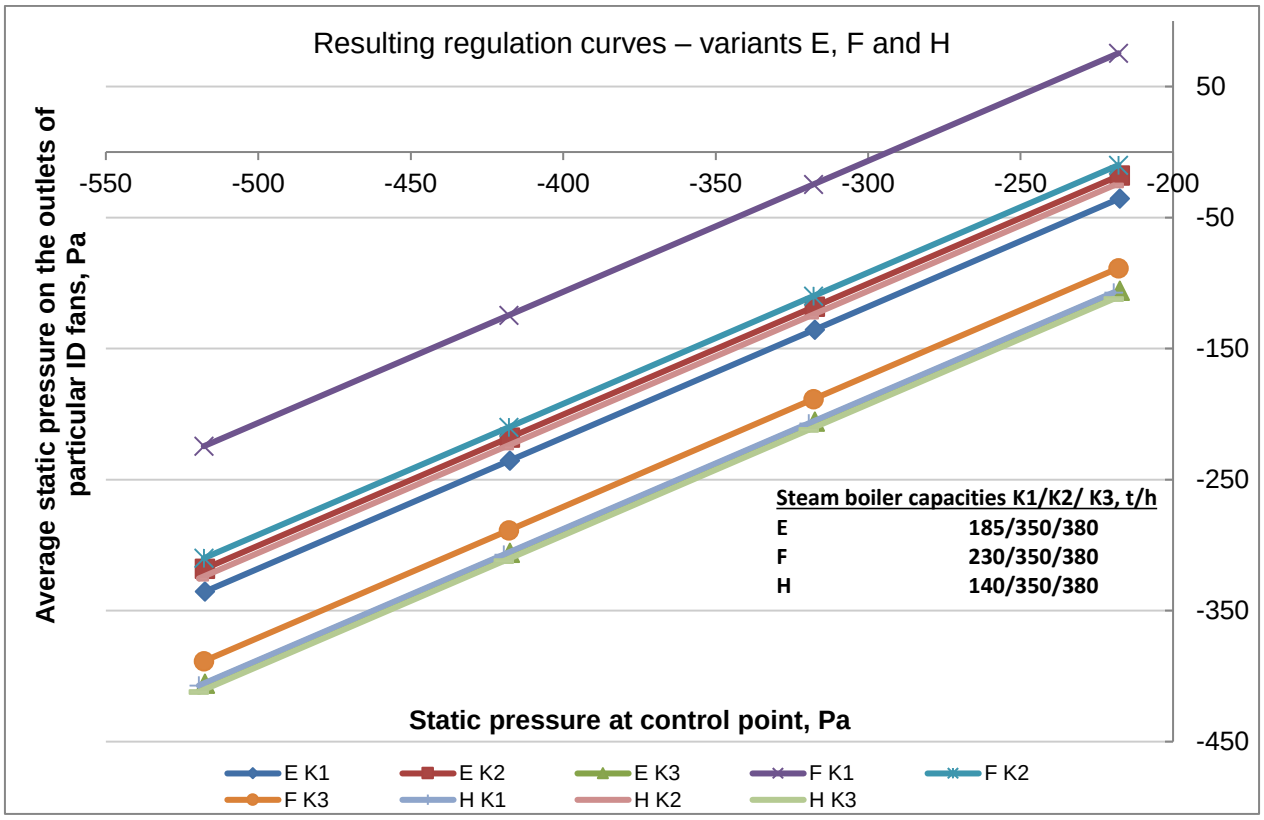

Figure 6.4 Regulation curves for E, F and H configurations

Besides the obvious benefits of having the regulation curves developed, another potentially useful dependency has been observed. Namely, a severe linear correlation between steam boiler capacity and the values of area averaged static pressure levels has been discovered. This allows to potentially program the secondary Induced Draft fans to work in relation to steam boiler capacity of given unit rather than the static pressure level at measurement point. Even though the benefits of such solution currently cannot be recognized, the information possibly could prove useful. The Figure 6.2 presents the discussed dependency for several configurations. It is worth to mention that the static pressure distribution of respective pairs of ducts from each unit depend on the steam boiler capacity of given unit itself rather than the collective configuration of each unit. The influence of one unit on the other in terms of pressure distribution seems almost negligible.

To summarize, the possibility to program main Induced Draft fans to depend on particular steam boiler capacity of a respective boiler has been noticed. The particular steam boiler capacities of each individual unit locally determine the static pressure levels at the inlets from given units rather than collective contributions of several units on the same values.

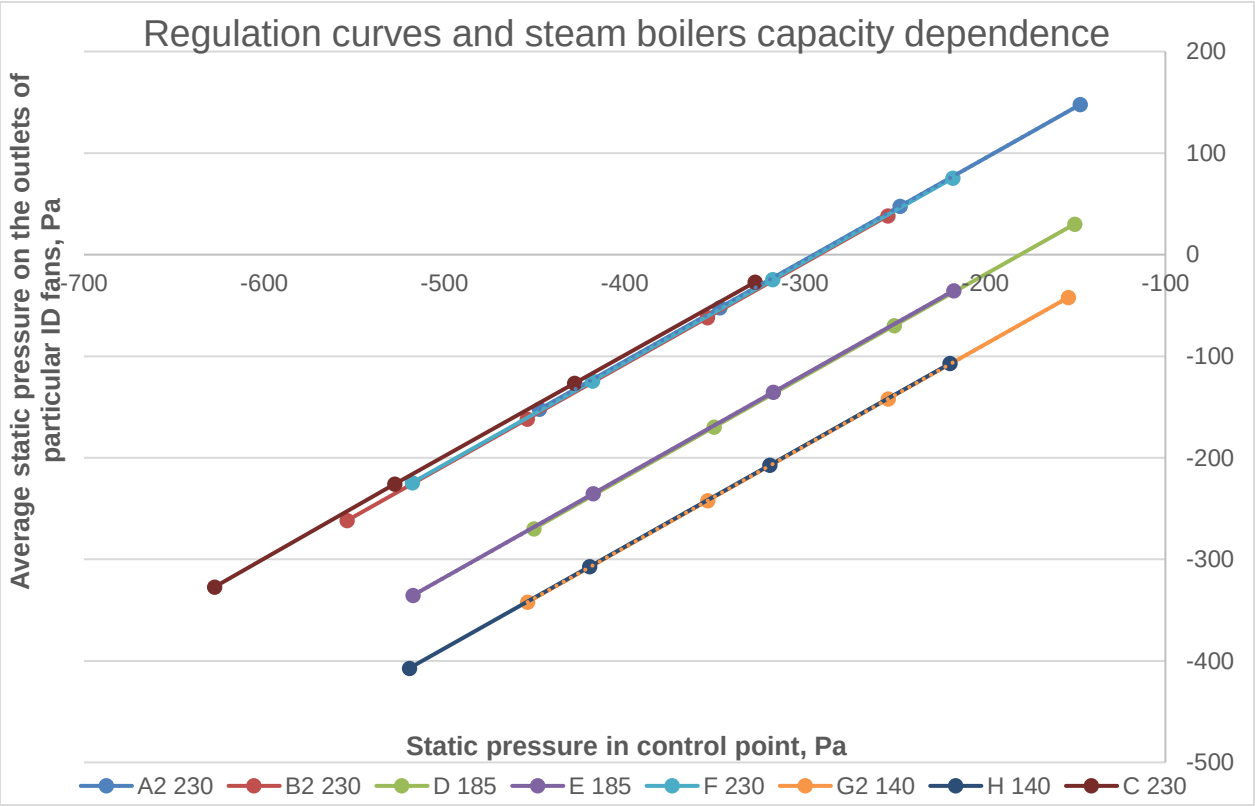

Figure 6.5 Regulation curves and steam boiler capacity dependence

6.3.2 The static pressure distribution and velocity streamlines for configuration A1

This chapter is dedicated to present the results in form of static pressure and velocity distributions throughout the installation for configuration A1. This configuration reflects the work of the system with maximum flue gas flow load, as it concerns the maximum steam boiler capacities for each unit (the mass flow rates and steam boiler capacities are presented on the Figure 6.6). Thus, the configuration is the most important from the point of view of operation and maintenance. The results on the figures to follow (namely Figures 6.7, 6.8, 6.9 and 6.10) below are presented as: top-left – static pressure distribution, top-right – velocity streamlines, bottom – static pressure with positive pressure marked with red color.

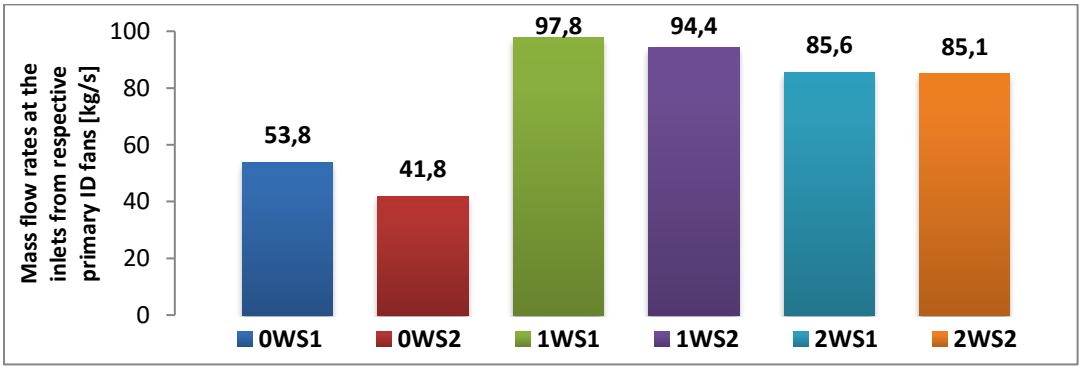

Figure 6.6 The mass flow rates at the inlets from respective primary Induced Draft fans for configuration A1

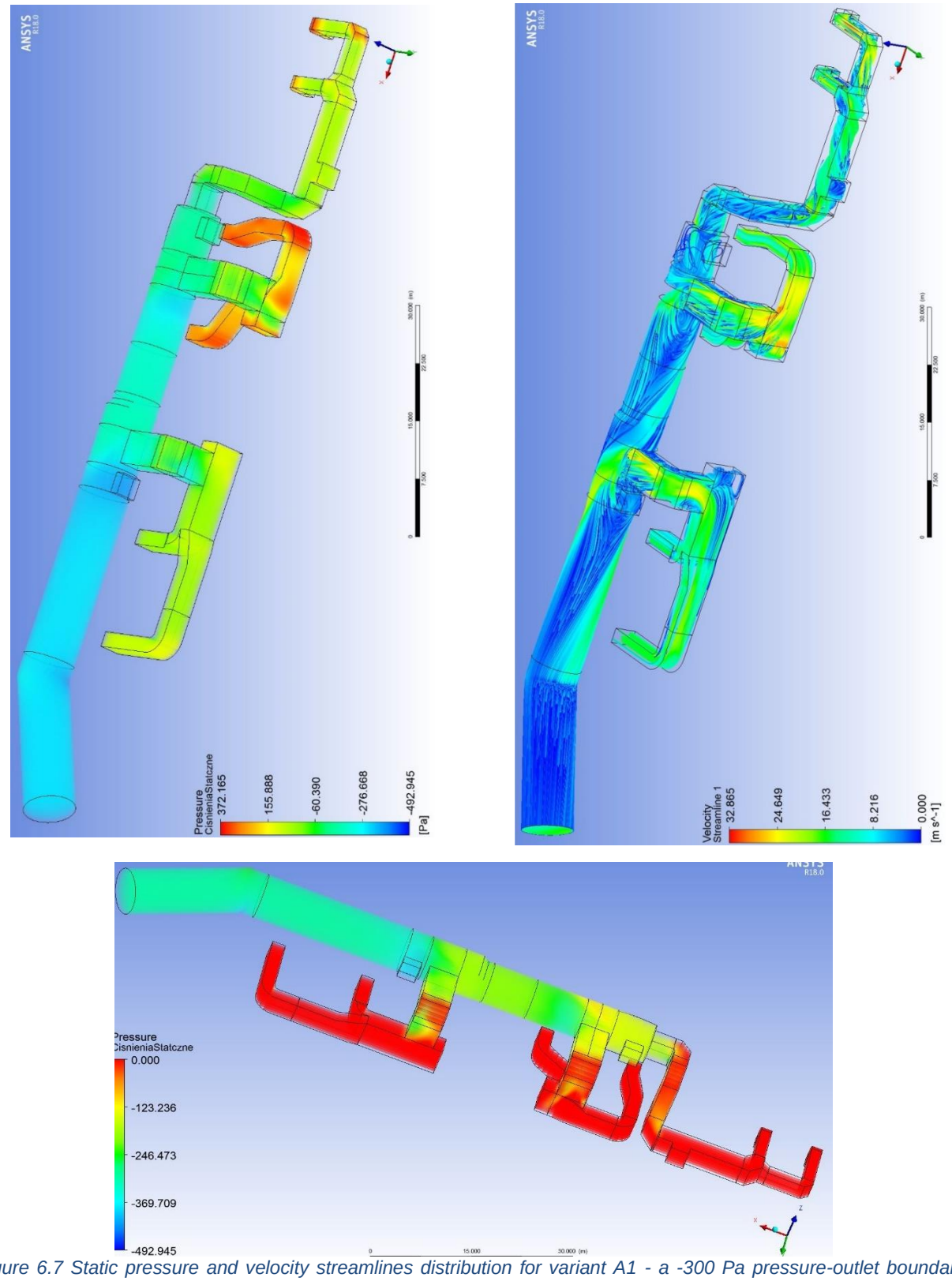

Figure 6.7 Static pressure and velocity streamlines distribution for variant A1 - a -300 Pa pressure-outlet boundary condition at "CollectorOutlet" evaluation plane (top-left – static pressure distribution, top-right – velocity streamlines, bottom – static pressure distribution with positive pressure marked as red color)

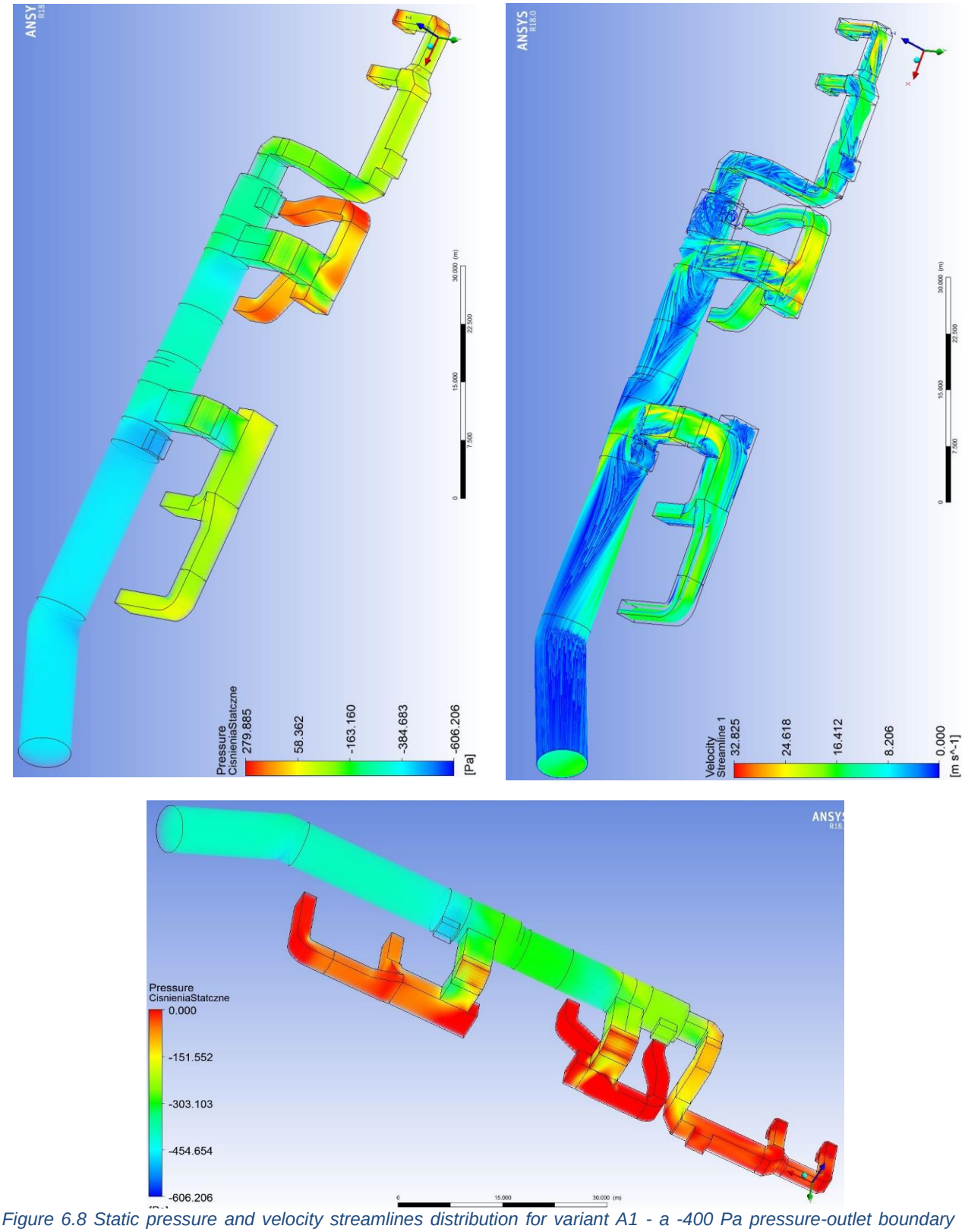

Figure 6.8 Static pressure and velocity streamlines distribution for variant A1 - a -400 Pa pressure-outlet boundary condition at "CollectorOutlet" evaluation plane (top-left – static pressure distribution, top-right – velocity streamlines, bottom – static pressure distribution with positive pressure marked as red color)

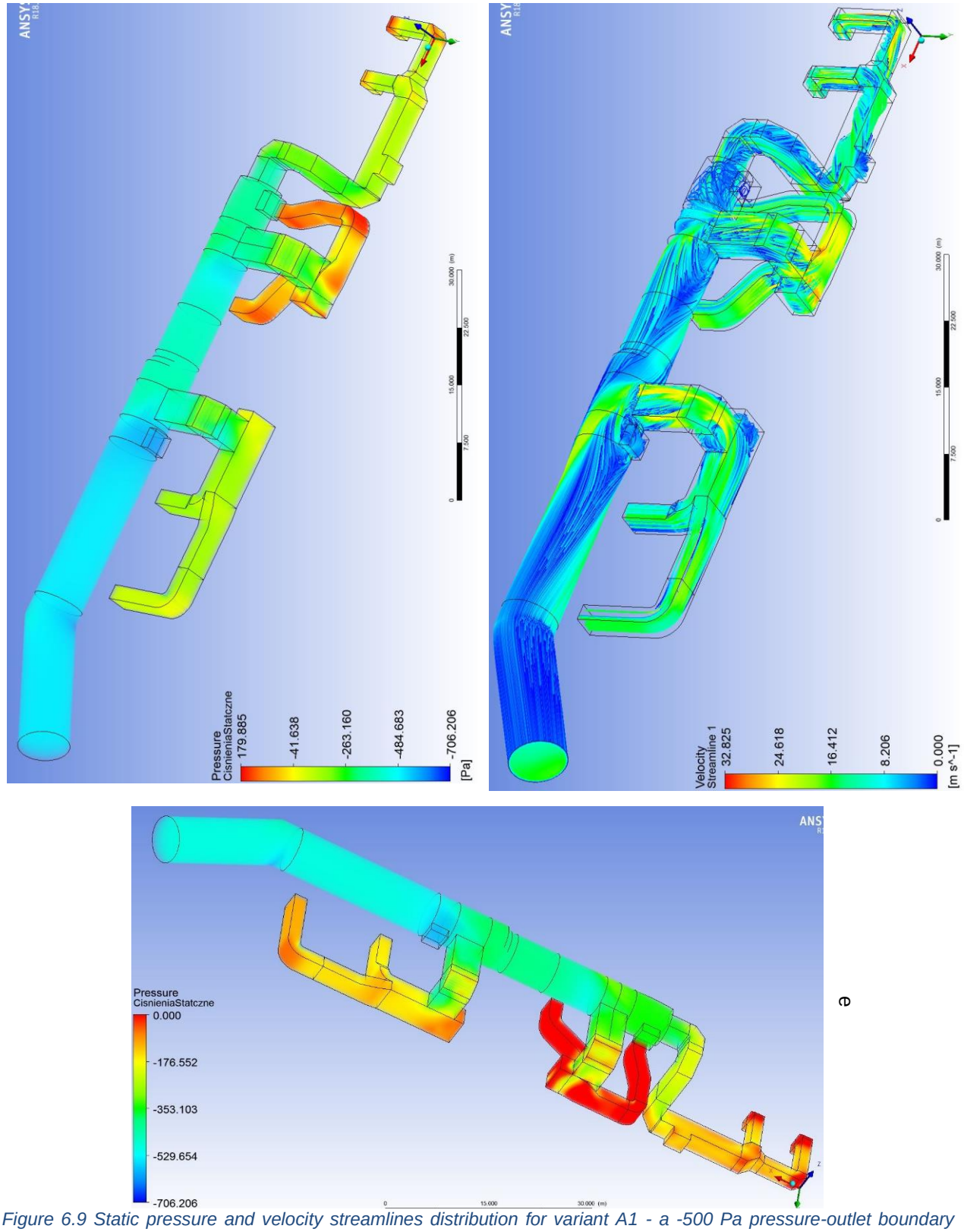

a

Figure 6.9 Static pressure and velocity streamlines distribution for variant A1 - a -500 Pa pressure-outlet boundary condition at "CollectorOutlet" evaluation plane (top-left – static pressure distribution, top-right – velocity streamlines, bottom – static pressure distribution with positive pressure marked as red color)

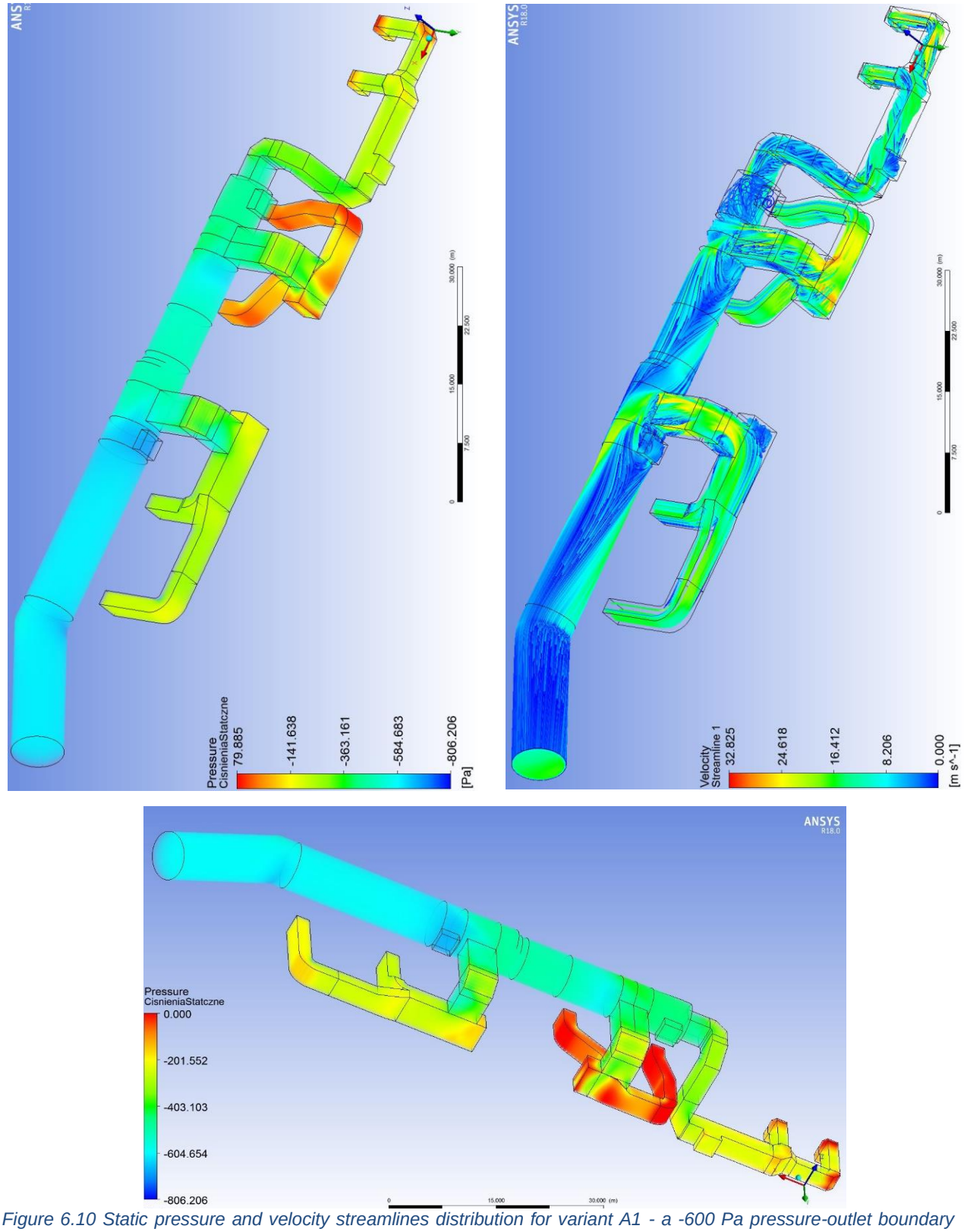

Figure 6.10 Static pressure and velocity streamlines distribution for variant A1 - a -600 Pa pressure-outlet boundary condition at "CollectorOutlet" evaluation plane (top-left – static pressure distribution, top-right – velocity streamlines, bottom – static pressure distribution with positive pressure marked as red color)

The static pressure distributions (top-left) has indicated graduate decrease in static pressure levels throughout the installation for consecutive assumed static pressure levels (i.e. -300; -400; -500 and -600 Pa) at “CollectorOutlet” surface as “pressure-outlet” boundary condition. The highest values of static pressure has been observed to be in K2 unit ducts and to a considerably lesser extend in K1 unit ducts.

The velocity streamlines is a group of curves being instantaneously tangent to the velocity vector of the flow. Therefore, they present the direction in which a fluid element at given point will travel. The resulting velocity streamlines has allowed to visualize this for the analyzed wet limestone FGD installation. The highest velocities has been noticed on K2 unit ducts. Further investigation of velocity streamlines for this location is conducted in chapter 6.2.5.

The bottom parts of Figures 6.7, 6.8, 6.9 and 6.10 represent a static pressure distribution with an indicative red-colored positive pressure levels in the installation. This representation allowed to show the places that work incorrectly (locations, where there is a positive static pressure levels). Not surprisingly, the highest pressure drop has been observed to occur in K2 unit ducts. The positive static pressure occurs for whole length of respective K2 ducts for every variation calculated that included the work of unit K2.

6.3.3 The static pressure distribution and velocity streamlines for configuration A2

This subchapter is represents the results in form of static pressure and velocity distributions in the installation for configuration A2. This configuration reflects the work of the system with maximum flue gas flow load, as it concerns the maximum steam boiler capacities for each unit (the mass flow rates and steam boiler capacities are presented on the Figure 6.11). Hence, the configuration is essential in terms of operation and maintenance. Analogically to previous subchapter the results on the figures to follow (namely Figures 6.12, 6.13, 6.14 and 6.15) below are shown as: top-left – static pressure distribution, top-right – velocity streamlines, bottom – static pressure with positive pressure marked with red color.

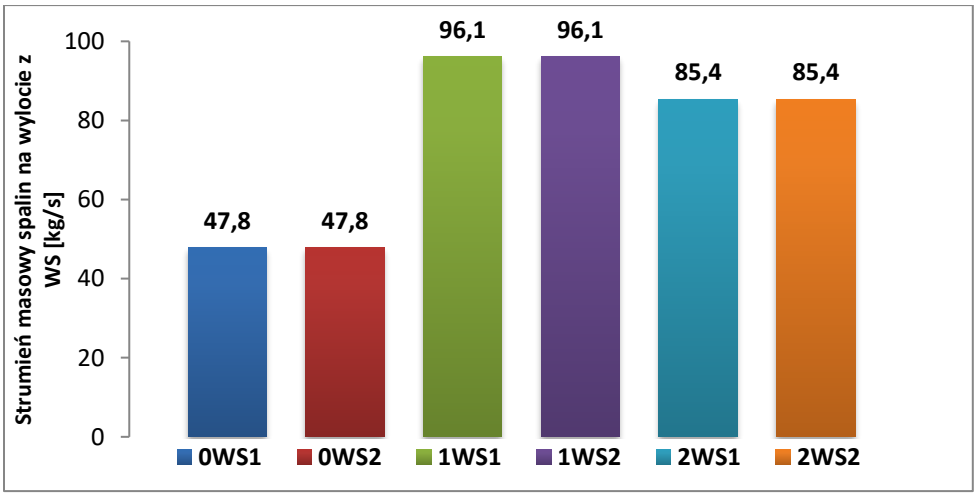

Figure 6.11 The mass flow rates at the inlets from respective primary Induced Draft fans for configuration A2

A2 is a configuration, where the mass flow rate boundary conditions on the inlets from respective unit has been assumed as an arithmetic average from measured values (in accordance with Figure 6.11), so that the impact of regular flow distribution for each of the two inlet ducts could be examined. The main purpose of this analysis is to compare the regular and irregular mass flow rates at the inlets to respective ducts of each unit and its impact on the static pressure levels, as well as velocity streamlines.

Based on the regulation curves, it has been already noticed the highest improvement (decrease) of static pressure for regular flow in place of the inlets from primary ID fans of K2 unit ducts at level 40 Pa at most. However, the differences in other locations are negligible. Moreover, static pressure graphic representation of the results presented on the Figures 6.12, 6.13, 6.14 and 6.15 further confirm that conclusion.

The results concerning the static pressure distributions (top-left) has presented the decrease in static pressure in the installation for followingly assumed static pressure values (i.e. -300; -400; -500 and -600 Pa) at “CollectorOutlet” face as “pressure-outlet” boundary condition. However, the highest levels of static pressure are found in K2 ducts. The K1 unit ducts have also shown increased static pressure levels for consecutive outlet BCs (boundary conditions), those values are a lot smaller in comparison to the K2 static pressure levels though.

According to obtained velocity streamlines the highest velocities has been noticed on K2 unit ducts. Further investigation of velocity streamlines for this location is conducted in chapter 6.2.5.

The bottom parts of Figures 6.12, 6.13, 6.14 and 6.15 represent a static pressure distributions with a red-colored indication of positive pressure occurrences in the installation for a consecutive outlet BC assumed. This representation enabled to identify the locations that work with incorrect positive pressure levels. The highest pressure values have occurred in K2 unit ducts. The positive static pressure appear for the entire length of the particular K2 ducts for each variation calculated that included the work of unit K2.

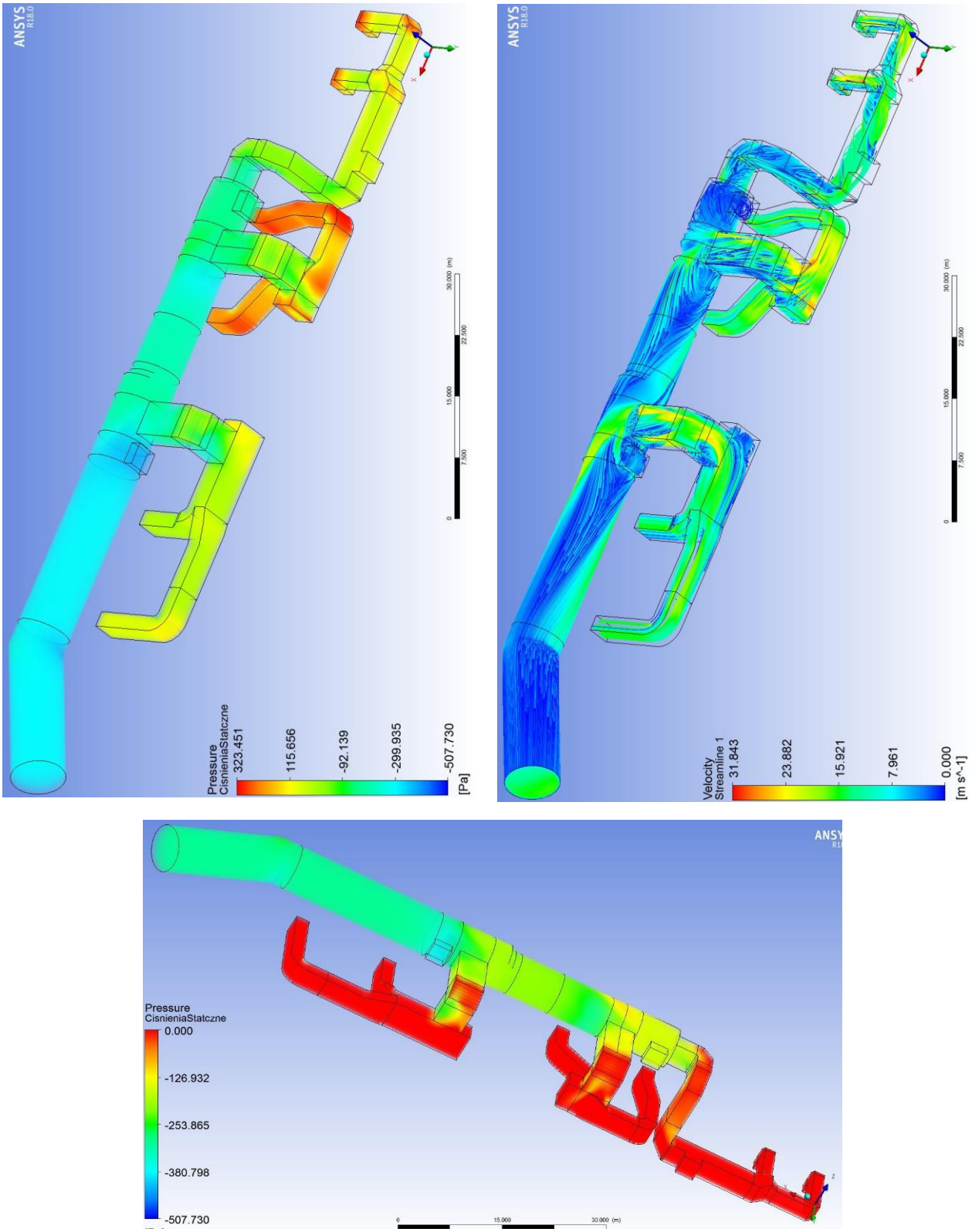

Figure 6.12 Static pressure and velocity streamlines distribution for variant A2 - a -300 Pa pressure-outlet boundary condition at "CollectorOutlet" evaluation plane (top-left – static pressure distribution, top-right – velocity streamlines, bottom – static pressure distribution with positive pressure marked with as color)

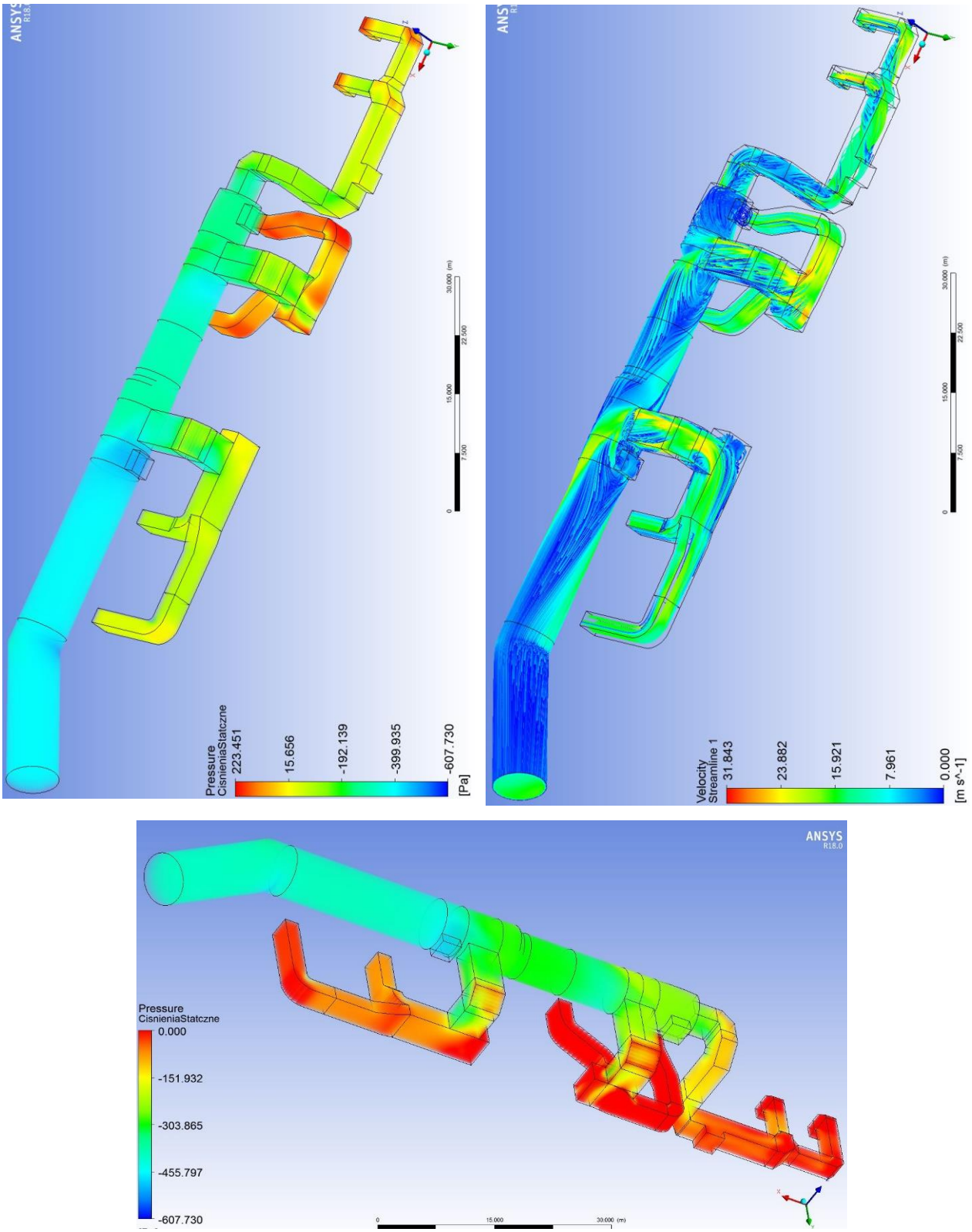

Figure 6.13 Static pressure and velocity streamlines distribution for variant A2 - a -400 Pa pressure-outlet boundary condition at "CollectorOutlet" evaluation plane (top-left – static pressure distribution, top-right – velocity streamlines, bottom – static pressure distribution with positive pressure marked as red color)

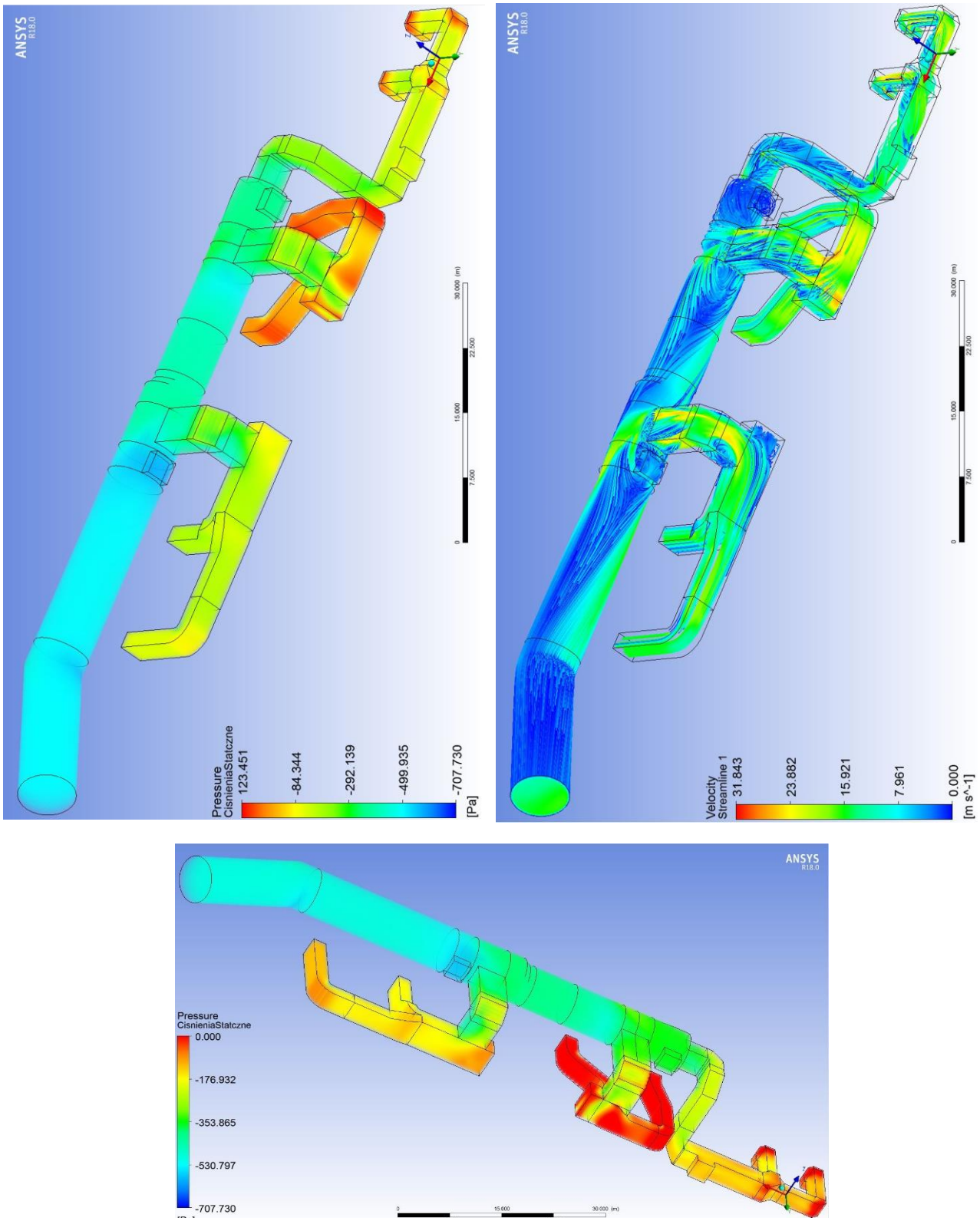

Figure 6.14 Static pressure and velocity streamlines distribution for variant A2 - a -500 Pa pressure-outlet boundary condition at "CollectorOutlet" evaluation plane (top-left – static pressure distribution, top-right – velocity streamlines, bottom – static pressure distribution with positive pressure marked as red color)

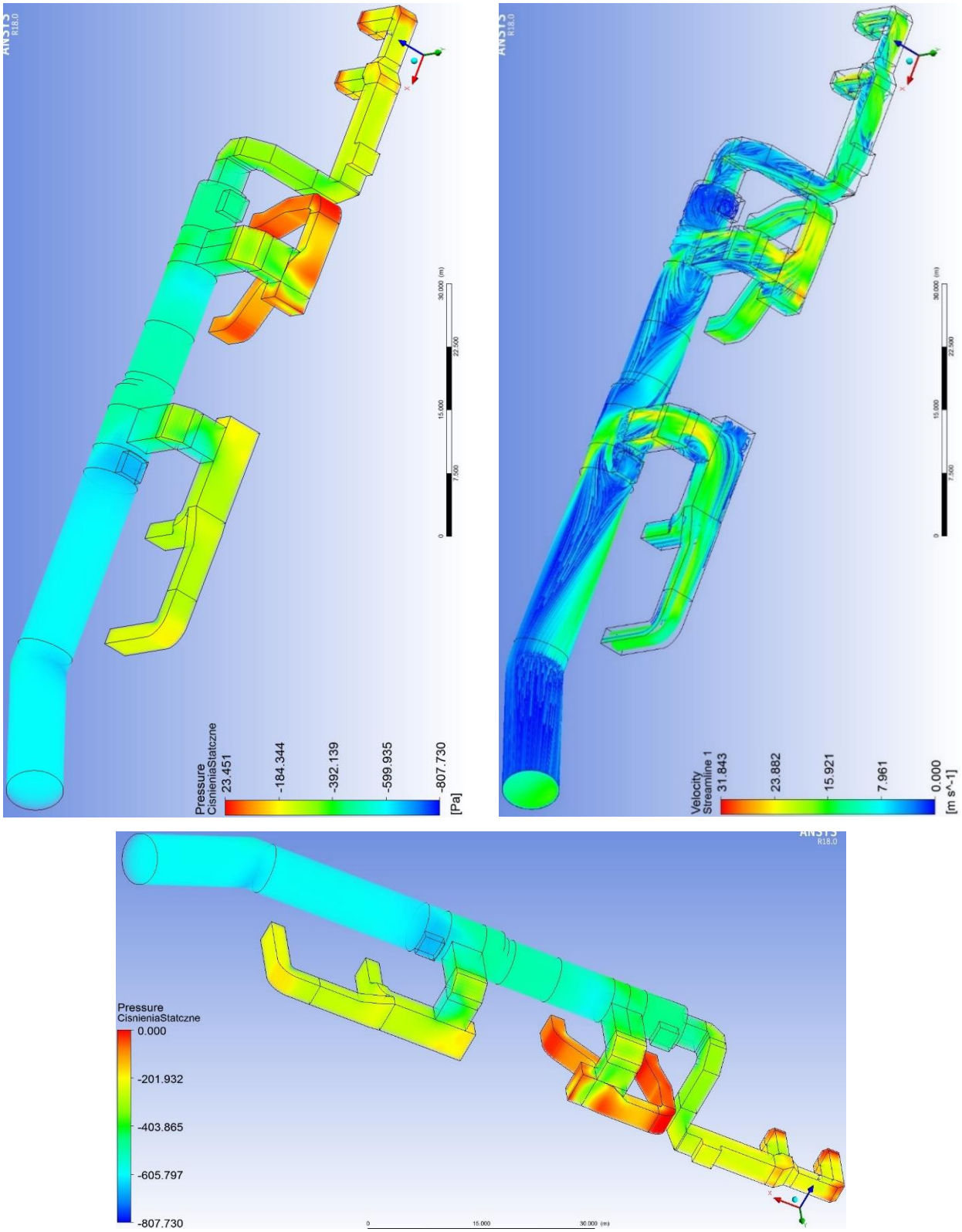

Figure 6.15 Static pressure and velocity streamlines distribution for variant A2 - a -600 Pa pressure-outlet boundary condition at "CollectorOutlet" evaluation plane (top-left – static pressure distribution, top-right – velocity streamlines, bottom – static pressure distribution with positive pressure marked as red color)

6.3.4 K2 unit ducts analysis

Since the unit K2 ducts have shown the worst results so far, the more attention had to be paid to velocity streamlines and the character of the flue gas flow in this location and surrounding area.

6.3.4.1 Velocity streamlines overview for configurations A1 and A2

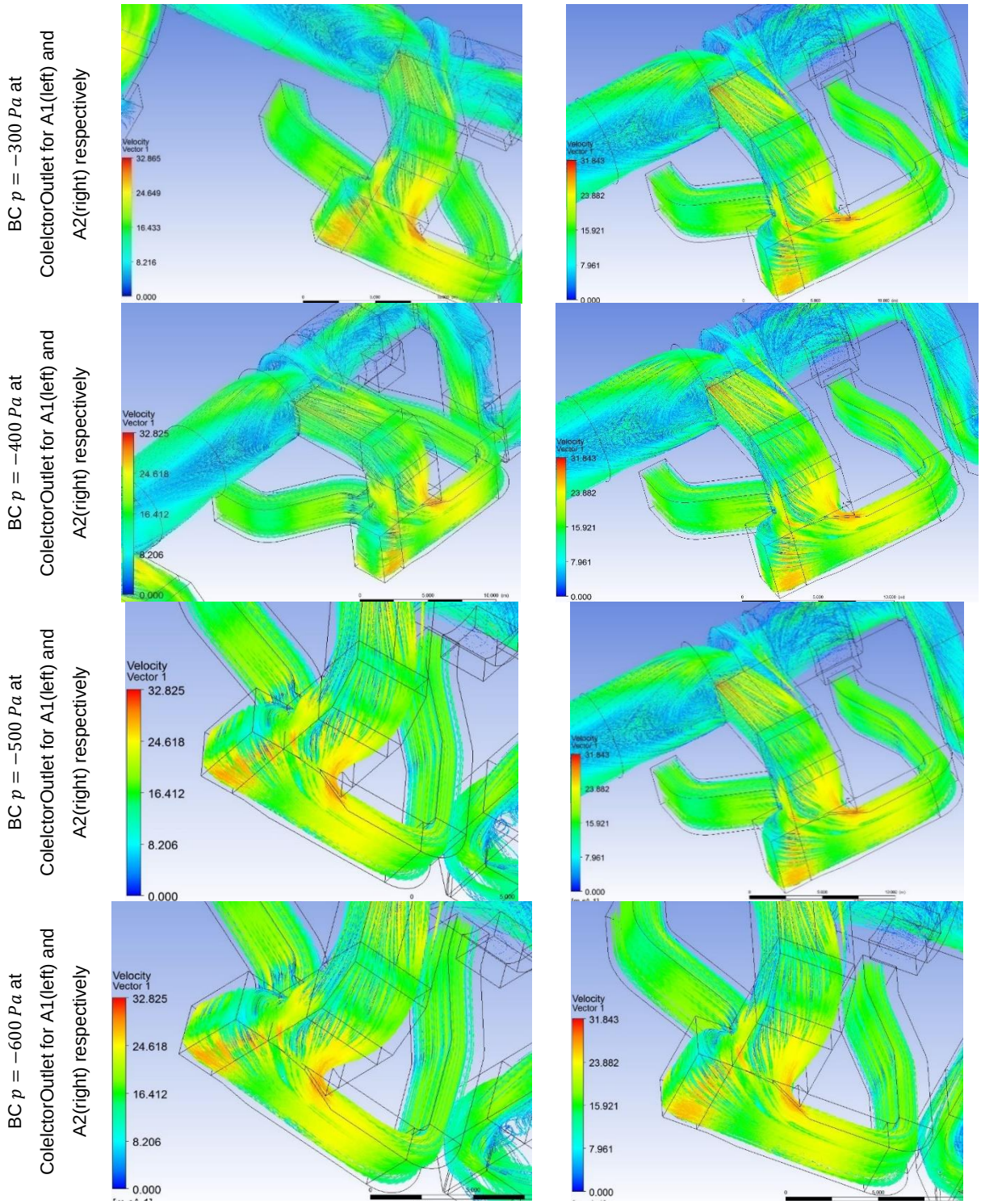

Figure 6.16 Velocity streamlines overview for variations A1 and A2 – more detailed investigation of K2 unit ducts

The previous results obtained from static pressure distributions has indicated increased pressure values throughout the K2 unit ducts (see Figures 6.7, 6.8, 6.9, 6.10, 6.12, 6.13, 6.14 and 6.15, as well as Table 6.3). Additionally, the regulation curves for each of the configurations that include the K2 unit operation have indicated the worst results in terms of static pressure levels to be in the K2 unit ducts (Figures 6.2, 6.3 and 6.4). In conjunction with the velocity streamlines presented on Figure 6.16 the results imply incorrect configuration of the K2 flue gas ducts. In terms of velocity, the manner of the flow in the location, where respective flue gas streams connect has strongly circulative flow character. It worsens so far smooth gas flow, resulting in unnecessary flue gas fluctuations that are the reverse of the designed operational idea of the assumed fluid flow in the ducts and collector. It is possible, that the aforementioned increased vibration levels detected during the warranty measurements are caused by the flue gas stream fluctuations in this location. However, further investigation would be necessary to confirm such hypothesis.

Furthermore, for each of the configurations in which the unit K2 is running, the velocity streamlines have very close character to the flow streamlines on Figure 6.16. The way, in which the K2 unit ducts are connected causes mutual counteracting of particular flue gas streams, simultaneously resulting in significant pressure drops and equivalently causing occurrence of positive pressures on the inlets from primary Induced Draft fans of K2 unit. It has been recommended to optimize the flow through modification of the local geometry of the duct system.

7. Conclusions

The comprehensive numerical analysis of flue gas flow in wet limestone FGD installation in a combined heat and power plant using Computational Fluid Dynamics has been performed. The evaluation provided static pressure and velocity distributions throughout the examined installation and indicated the locations subject to increased pressure levels. The different steam boiler capacity collective variants has been analyzed, providing exhaustive elaboration for an installation owner. The static pressure distributions has indicated graduate decrease in static pressure levels throughout the installation for consecutive assumed static pressure levels (i.e. -300; -400; -500 and -600 Pa) at “CollectorOutlet” surface as “pressure-outlet” boundary condition. The highest values of static pressure has been observed to be in K2 unit ducts and to a considerably lesser extend in K1 unit ducts for configurations, where the K2 unit was operating. The positive static pressure occurs for an entire length of respective K2 unit ducts for every variation calculated that included the work of unit K2. The resulting velocity streamlines has allowed to visualize the fluid flow and local velocities of the streams for the analyzed wet limestone FGD installation. The highest velocities has been noticed on K2 unit ducts. For each of the configurations, where the unit K2 is operating, the particular velocity streamlines has showed adverse character. The manner, in which the K2 unit ducts are joint together causes mutual counteracting of respective flue gas streams, simultaneously resulting in high pressure drops and causing occurrence of positive pressures on the inlets from primary Induced Draft fans of K2 unit at the same time. Thus, the determined location with faulty duct configuration design, that

potentially could be improved. It has been advised to optimize the fluid flow through modification of the local geometry of the ducts system. The numerical simulation results, that include analysis of different operational configurations have allowed to develop the regulation curves, that demonstrate the dependency of the pressure level at Control Point on the area averaged static pressure levels at the inlets from respective primary induced draft fans from units K1, K2 and K3. The results imply that the previous designed value of the static pressure at control point (-250 Pa) was incorrect as it was impossible to maintain the sub-pressure at the inlets form respective primary Induced Draft fans of each unit. The updated value of the static pressure at control point (-350) allows to maintain negative pressure throughout the respective flue gas ducts for configurations C, E, F and H. However, in order for the flue gas ducts and collector to work under sub-pressure pressure for every variant the pressure level at control point has to be kept at level -450 Pa. This value has to be treated as a maximum limit. In other words, the system evaluation has enabled the programmable secondary Induced Draft fans setup to produce sufficiently low pressure for the flue gas ducts and the collector in order for the installation to work under negative pressure. The comparison of variants A1 and A2 has shown the impact of irregular mass flow rates at the inlets to respective ducts of each unit. In case of regular flow, the decrease in the static pressure levels has been observed in the inlets from primary ID fans of respective unit ducts to obtain at most 40 Pa in comparison to irregular flow (for the same steam boiler capacities). This highest difference has been noted for ducts of unit K2. The differences in other locations are negligible though. Subsequently, the possibility to program main Induced Draft fans to depend on respective steam boiler capacity of a particular boiler has been noticed basing on regulation curves. A correlation between steam boiler capacity and the values of area averaged static pressure levels has been discovered. This allows to potentially program the main ID fans to work in relation to steam boiler capacity of given unit rather than the static pressure level at measurement point. Even though the benefits of such approach in developing a control system currently cannot be recognized, the information could prove useful in the future. In addition, the static pressure distribution of respective pairs of ducts from each unit depend on the steam boiler capacity of particular unit itself rather than the collective configuration of each unit. The impact of one unit work on the another in terms of pressure distribution seems hardly noticeable.

The thesis took advantage of several engineering tools, such as ANSYS Fluent, ANSYS Meshing, ANSYS SpaceClaim and Engineering Equation Software to evaluate the industrial flue gas ducts system and relied on the gathered internal CHP plant measured data and records in order to develop the most accurate numerical model. The mesh sensitivity analysis and mesh quality optimization have been performed to maximize the results accuracy with simultaneous minimization of the computation time. The justification for applying subsequent boundary conditions and particular methodology in numerical model development has been described including assembly of different assumptions concerning the flow and fluid itself. Moreover, the state of the art of contemporary Flue Gas Desulfurization Technologies for Coal-Fired Power Plants has been reviewed with utmost priority given to wet limestone FGD systems due to the fact, that the analyzed FGD installation uses this method to mitigate SO_2 content in the flue gases. Additionally, the elaboration concerning the fluid dynamics equations, mass, momentum and energy transport equations, as well as

several methodologies and approaches in turbulence modeling has been discussed to a extend, that sufficed to develop the numerical model of wet limestone FGD installation for the particular system conditions.

References

[1] Patricia Córdoba, Status of Flue Gas Desulphurization (FGD) systems from coal-fired power plants: Overview of the physic-chemical control processes of wet limestone FGDs, Fuel, Volume 144,2015,Pages 274-286,ISSN 0016-2361

[2] Soud HN. Developments in FGD. CCC/29, IEA Coal Research, London; 2000.

[3] United States Environmental Protection Agency (US EPA). Controlling SO2 emissions: a review of technologies. EPA/600/R-00/093; 2000.

[4] Benko˝ T., Mizsey P., Comparison of flue gas desulphurization processes based on life cycle assessment, Chemical Engineering 51/2 (2007) 19–27

[5] Clarke L, Sloss L. Trace elements. EIACR/49.Ed, IEA coal research; 1992. p. 51.

[6] Helle GN, Soren K, Jan EJ, Jorgen NJ, Jørn H, Folmer F, et al. Full-scale measurements of SO2 gas phase concentrations and slurry compositions in a wet flue gas desulphurisation spray absorber. Fuel 2004;83:1151–64.

[7] Clarke L. The fate of trace elements during combustion and gasification: an overview. Fuel 1993;72(6):731–6.

[8] Schroeder K, Kairies C. Distribution of Hg in FGD by-products. In: Proceedings of world of coal ash conference, CAER, University of Kentucky, April 11–1. Paper 100; 2005.

[9] United States Environmental Protection Agency (US EPA). Flue gas desulfurization system capabilities for coal-fired steam generators. Vol II, Technical Report. EPA-600/7-78-032b; March 1978.

[10] Reference document on best available techniques for large combustion plants(BREFs); 2006.

[11] Babcock & Wilcox Power Generation Group (B&W). Steam-its generation anduse, 40th ed. Barbeton, Ohio: Babcock and Wilcox Company; 1991. p. 980.

[12] Polster M, Nolan PS, Batyko RJ. Babcock & Wilcox Technologies for powerplant stack emissions control. Paper N. BR-1571, U.S./Korea Electric Power Technologies Seminar Mission, Seoul, Korea; October 1994.

[13] Lani BW, Babu M. Phase II: the age of high velocity scrubbing. EPRIDOE-EPA combined utility air pollutant control symposium: the mega symposium: SO2control technologies and continuous emission monitors, EPRI, Palo Alto, CA,U.S. Department of Energy, Pittsburgh, PA,4 and U.S. Environmental Protection Agency, Air Pollution Prevention and Control Division, Research Triangle Park, NC. TR-108683-V2; 1997.

[14] Benson L, Garner J, Murphy JL, Thompson M, Weilert C. Henderson municipal power& light a low-cost phase I clean air act retrofit. EPRI-DOEEPA combined utility air pollutant control symposium: the mega symposium: SO2 control technologies and continuous emission monitors, EPRI, Palo Alto, CA, U.S. Department of Energy, Pittsburgh, PA, and U.S. EPA, Air Pollution Prevention and Control Division, Research Triangle Park, NC. TR-108683-V2; 1997.

[15] Kamall R. Flue Gas Desulphurization (FGD) technologies. Cleaner coal technology programme, Department of Trade and Industry, 1 Victoria Street, London SW1H 0ET; 2000.

[16] Zheng Y, Kiil S, Johnsson JE, Zhong Q. Use of spray dry absorption product inwet flue gas desulphurization plants: pilot-scale experiments. Fuel2002;81:1899–905.

[17] Bennett R. Fly ash conditioning to improve precipitator efficiency with low sulphur coals. (www.benetechusa.com) [accessed 07.05.18]

[18] Oglesby S, Nichols GB. Electrostatic precipitation. New York: Marcel Dekker Inc.; 1978.

[19] EPA. Stationary source control techniques document for fine particulate matter. Final technical report. USEPA. Report no. EPA-452/R-97-001, 1998.

[20] Centro de Investigaciones Energéticas y Medioambientales (CIEMAT). Flue gas cleaning. Clean coal technologies handbook; 2000.

[21] Frandsen JBW, Kiil S, Johnsson JE. Optimisation of a wet FGD pilot plant using fine limestone and organic acids. Chem Eng Sci 2001;56:3275–87.

[22] Gutiérrez Ortiz FJ. A simple realistic modeling of full-scale wet limestone FGD units. Chem Eng J 2010;165:426–39.

[23] Anil W. Date, Introduction to Computational Fluid Dynamics,Cambridge University Press, New York 2005

[24] Perry, R. H. and Chilton, C. H., Chemical Engineers' Handbook, 5th Ed., McGraw-Hill–Kogakusha, Tokyo (1973)

[25] Versteeg, H. K., Malalasekera W., An introduction to computational fluid dynamics. The finite volume method., Longman Group Ltd 1995, Longman Scientific & Technical

[26] Bland, D. R., Wave theory and applications, Clarendon Press, Oxford 1988

[27] Fletcher, C. A. J., Computational Techniques for Fluid Dynamics, Volumes I and II, Springer-Verlag, Berlin 1991

[28] Shapiro, A. H., Compressible fluid flow, Volume 1, John Wiley & Sons, New York 1953

[29] Gersho, P. M., Incompressible Fluid Dynamics: Some Fundamental Formulation Issues, Annu. Rev. Fluid Mech., Volume 23, No. 10, pp. 1751-1757

[30] Schlichting, H., Boundary-layer theory, 7th ed, McGraw-Hill, New York 1979

[31] The Open University, Mathematical methods and fluid mechanics, Course MST322, The Open University Press, Milton Keynes, England 1984

[32] Abbott, M. B., Basco, D. R., Computational Fluid Dynamics – An Introduction for Engineers, Longman Scientific & Technical, Harlow, England 1989

[33] Amano, R. S., Goel, P., Investigation of Third-order Closure Model of Turbulence for the Computation of Incompressible Flows in a Channel in a Backward-facing Step, Trans. ASME, J. Fluids Eng.,1987, Volume 109, pp. 424-429.

[34] Anderson D. A., Tannehill J. C., Pletcher R. H., Computational Fluid Mechanics and Heat Transfer, Hemisphere Publishing Corporation, Taylor & Fancis Group, New York 1984

[35] Baldwin B. S., Lomax H., Thin Layer Approximation and Algebraic Model for Separated Turbulent Flow, AIAA paper 78-257, 1978

[36] Bradshaw P., George Jr. W. K., Lumley J. L., The Measurement of Turbulence with the Laser-Doppler Anemometer, Annu. Rev. Fluid Mech., Vol. 11, pp. 443-503, 1979

[37] Cebeci T., Essential Ingredients of a Method for Low Reynolds-number Airfoils, AIAA J., Vol. 27, No. 12, pp. 1680-1688, 1989

[38] Cebeci T., Smith, AMO, Analysis of Turbulent Boundary Layers, Applied Mathematics and Mechanics, Vol. 15, Academic Press, New York 1974

[39] Comte-Bellot G., Hot-wire Anemometry, Annu. Rev. Fluid Mech., Vol. 8, pp. 209-231, 1976

[40] Demuren A. O., Rodi W., Calculation of Turbulence-driven Secondary Motion in Non-circular Ducts, J. Fluid Mech., Vol. 140, pp. 189-222, 1984

[41] Gatski T. B., Speziale C. G., On Explicit Algebraic Stress Models for Complex Turbulent Flows, J. Fluid Mech., Vol 254, pp. 59-78, 1993

[42] Horiuti K., Higher-order Terms in the Anisotropic Representation of Reynolds Stressesm Phys. Fluids A, Vol. 2, No. 10, pp. 1708-1710, 1990

[43] Klebanoff P. S., Characteristics of Turbulence in a Boundary Layer with Zero Pressure Gradient, NACA Report 1247, National Bureau of Standards, Washington, D.C. 1955

[44] Kleiser L., Zang T. A., Numerical Simulation of Transition in Wall-bounded Shear Flows, Annu. Rev. Fluid Mech., Vol. 23, pp. 495-537, 1991

[45] Lam C. K. G., Bremhorst K. A., Modified Form of the k-ϵ Model for Predicting Wall Turbulence, Trans. ASME, J. Fluids Eng., Vol. 103, pp. 456-460, 1981

[46] Launder B. E, Spalding D. B., The Numerical Computation of Turbulent Flows, Comput. Methods Appl. Mech. Eng., Vol. 3, pp. 269-289, 1974

[47] Launder B. E, Reece G. J., Rodi W., Progress in the Development of a Reynolds-stress Turbulence Closure, J. Fluid. Mech., Vol. 68, Pt 3, pp. 537-566, 1975

[48] Rodi V. C., Turbulence Models and Their Application in Hydraulics – A State of the Art Review, IAHR, Delft, The Netherlands 1980

[49] Tenneks H., Lumley J. L., A first course in turbulence, MIT Press, Cambridge, MA 1972

[50] Patel V. C., Rodi W., Scheuer G., Turbulence Models for Near-Wall and Low Reynolds Number Flows: A review AIAA J., Vol. 23, No. 9, pp. 1308-1319, 1985

[51] Shih T.-H., Liou W.W., Shabbir A., Yang Z., Zhu J., A New k-ε Eddy Viscosity Model for High Reynolds Number Turbulent Flows – Model Development and Validation, Institute for Computational Mechanics in Propulsion and Center for Modeling of Turbulence and Transition, NASA, Lewis Research Center, Cleveland, Ohio 1994

[52] Reynolds W.C., Fundamentals of turbulence for turbulence modeling and simulation, Lecture Notes for Von Karman Institute, Agard Report No. 755, 1987

[53] Shih T.-H., Zhu J., Lumley J. L., A First Course in Turbulence, The MIT press 1972

[54] ANSYS Fluent User's Guide 15.0